介质阻挡放电等离子体激发器在湍流减阻中的应用研究

（申请清华大学工学博士学位论文）

培 养 单 位 ： 航 天 航 空 学 院
学　　科 ： 力 学
研　究　生 ： 王　哲　夫
指 导 教 师 ： 符　松　教　授

二〇一八年三月

Study of the application of Dielectric-Barrier-Discharge plasma actuators in turbulent drag reduction

Dissertation Submitted to

Tsinghua University

in partial fulfillment of the requirement

for the degree of

Doctor of Philosophy

in

School of Aerospace Engineering

by

Wang Zhefu

Dissertation Supervisor : Professor Fu Song

March, 2018

关于学位论文使用授权的说明

本人完全了解清华大学有关保留、使用学位论文的规定，即：

清华大学拥有在著作权法规定范围内学位论文的使用权，其中包括：（1）已获学位的研究生必须按学校规定提交学位论文，学校可以采用影印、缩印或其他复制手段保存研究生上交的学位论文；（2）为教学和科研目的，学校可以将公开的学位论文作为资料在图书馆、资料室等场所供校内师生阅读，或在校园网上供校内师生浏览部分内容；（3）根据《中华人民共和国学位条例暂行实施办法》，向国家图书馆报送可以公开的学位论文。

本人保证遵守上述规定。

（保密的论文在解密后应遵守此规定）

作者签名：_____　　导师签名：_____

日　　期：_____　　日　　期：_____

摘　要

论文的摘要是对论文研究内容和成果的高度概括。摘要应对论文所研究的问题及其研究目的进行描述，对研究方法和过程进行简单介绍，对研究成果和所得结论进行概括。摘要应具有独立性和自明性，其内容应包含与论文全文同等量的主要信息。使读者即使不阅读全文，通过摘要就能了解论文的总体内容和主要成果。

论文摘要的书写应力求精确、简明。切忌写成对论文书写内容进行提要的形式，尤其要避免“第 1 章……；第 2 章……；……”这种或类似的陈述方式。

本文介绍清华大学论文模板 ThuThesis 的使用方法。本模板符合学校的本科、硕士、博士论文格式要求。

本文的创新点主要有：

- 用例子来解释模板的使用方法；
- 用废话来填充无关紧要的部分；
- 一边学习摸索一边编写新代码。

关键词是为了文献标引工作、用以表示全文主要内容信息的单词或术语。关键词不超过 5 个，每个关键词中间用分号分隔。（模板作者注：关键词分隔符不用考虑，模板会自动处理。英文关键词同理。）

关键词：TEX； LATEX； CJK；模板；论文

Abstract

An abstract of a dissertation is a summary and extraction of research work and contributions. Included in an abstract should be description of research topic and research objective, brief introduction to methodology and research process, and summarization of conclusion and contributions of the research. An abstract should be characterized by independence and clarity and carry identical information with the dissertation. It should be such that the general idea and major contributions of the dissertation are conveyed without reading the dissertation.

An abstract should be concise and to the point. It is a misunderstanding to make an abstract an outline of the dissertation and words “the first chapter”, “the second chapter” and the like should be avoided in the abstract.

Key words are terms used in a dissertation for indexing, reflecting core information of the dissertation. An abstract may contain a maximum of 5 key words, with semi-colons used in between to separate one another.

Key words: TEX; LATEX; CJK; template; thesis

目 录

主要符号对照表

HPC	高性能计算 (High Performance Computing)
cluster	集群
Itanium	安腾
SMP	对称多处理
API	应用程序编程接口
PI	聚酰亚胺
MPI	聚酰亚胺模型化合物，N-苯基邻苯酰亚胺
PBI	聚苯并咪唑
MPBI	聚苯并咪唑模型化合物，N-苯基苯并咪唑
PY	聚吡咙
PMDA-BDA	均苯四酸二酐与联苯四胺合成的聚吡咙薄膜
ΔG	活化自由能 (Activation Free Energy)
χ	传输系数 (Transmission Coefficient)
E	能量
m	质量
c	光速
P	概率
T	时间
v	速度
劝学	君子曰：学不可以已。青，取之于蓝，而青于蓝；冰，水为之，而寒于水。—— 荀况

第1章　引言

等离子体激发器由于具有响应时间短，安装方便，耗能低，器件小等众多优点，近些年得到了流动控制领域研究者们的青睐。本文主要研究了介质阻挡放电（dielectric barrier discharge，DBD）等离子体激发器在湍流减阻方面的应用。研究主要分为两个部分，分别是通过推迟转捩降低阻力和通过改变充分发展湍流的相干结构降低阻力。引言部分将会先介绍我们所采用的等离子体激发器，然后再分别综述这两种控制方法的研究现状。

1.1　介质阻挡放电等离子体激发器

等离子体是除了液态、固态以及气态之外的物质第四态[1,2]。等离子体可由高温或者强电场产生。高温条件下气体会离解产生等离子体。在电场力的作用下气体也会电离产生等离子体，电离产生的等离子体通常由大量的电子和相应成对出现的离子构成。在电场的作用下，等离子体可以表现出明显的集体行为[3]。在本文中，主要是用的介质阻挡放电等离子体激发器。这种激发器由两片电击和一层绝缘层构成（如图 1.1所示）。当在两片电极上加上高电压时，两片电击之间的空气就会被电离。在电场的作用下，带电的离子会做定向运动，并通过与不带电的空气分子的碰撞作用，将动量转移到空气分子上。从宏观的角度看，等离子体激发器在开启时会产生图示方向的射流。介质阻挡放电等离子体激发器的出现最早可以追溯到1979年[4]。在1998年，Roth首次将其用于流动控制[5]。由于本文主要是采用数值模拟的方法研究这种激发器在流动控制中的应用，所以本文将在引言的第一部分重点介绍DBD等离子体激发器的数值模拟方法与将其应用于流动控制的研究现状。

1.1.1　介质阻挡放电等离子体激发器数值模拟方法

从目前的研究可知，介质阻挡放电等离子体的放电和气动激励过程中的各个物理过程的时间跨度较大，其中包括瞬间发生的电磁场分布过程、不足纳秒和纳秒级的电子能量传输及输运过程、微秒级的离子输运过程和毫秒级的中性气体间的动量交换及传热过程等，较大的时间跨度使得对等离子体的数值仿真存在着较大的难度。因此，许多研究者提出可以在结果合理的前提下，对等离子体气动激励这一复杂的多物理过程进行必要的简化，提出其中的主要激励机理。在现阶段，

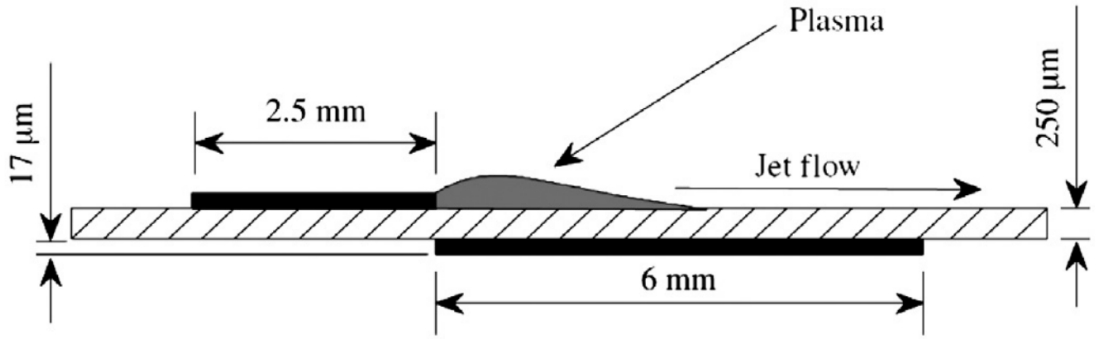

图 1.1　等离子体激发器示意图[6]

这种简化过程对研究和应用等离子体流动控制这一前沿技术是十分必要的。目前，介质阻挡放电等离子体气动激励的仿真模型主要有以下几类。

等离子体简化模型唯象简化模型作为数值模拟中最为简单和常见的模型，其基本思路是将因粒子碰撞产生的动量传递效应简化为一种作用于流体的电场力，并将其以体积力源项的形式与 N-S 方程耦合求解。简化模型通常需要利用实验结果对模型中的相关参数进行修正。基于不同的假设条件，Massines [89] 、Orlov [90] 、Shyy [91] 、 Suzen [92] 、Roth [93] 分别各自提出了自己的简化模型，同时国内外的研究者在此类模型基础上做了大量的研究工作。Rizzetta [94] 基于 Shyy 提出的简化模型，并利用大涡模拟数值方法研究了等离子体对湍流附面层的流动控制。毛枚良 [95] 等人利用简化模型，对 NACA0015 翼型进行了数值研究，探讨了大气压下辉光放电等离子体对边界层流动的影响。陈浮 [96] 等人采用三种不同的简化模型对比研究了 5kV 激励电压作用下的诱导流场，分析探讨了各模型的优缺点。王江南 [97] 等人进行了流动分离控制的数值模拟研究，结果表明等离子体流动控制方法可以有效地延迟流动的分离，达到增升减阻的目的。 1.4.5.2 集总电路求解模型集总电路求解模型主要基于等离子体放电过程中的电流与电场强度的关系，建立起等离子体气动激励器电特性的分析模型。此类简化模型可以获得功率和电流随时间变化的数学表达式，以及电功率、电流和相位差对电压幅值、交流电频率、绝缘层厚度和介电常数等参数之间的依赖关系。该模型通过将等离子体激励器等效成一个集总电路原件的形式来描述等离子体气动激励器的行为。Orlov [98] 验证了等离子体气动激励器的推力与施加在电极两端的电压成

1.1.2　介质阻挡放电等离子体激发器在流动控制方面的应用

介质阻挡放电等离子体激发器在流动控制方面的应用

1.2　通过推迟层流/湍流转捩减阻

众所周知，层流的摩擦阻力要比湍流的摩擦阻力小很多，所以流动减阻的一个重要方向就是扩大飞行器表面的层流范围。对于大型客机而言，由于机身长度过长，转捩总会无可避免的发生。相比之下，在机翼上发展和应用层流技术则有很大的前景。目前大多数客机使用的机翼还都是湍流机翼。湍流机翼发生从层流向湍流的转捩点一般在翼型弦长的10%以前，而如果使用推迟转捩的层流技术，可以将转捩点推迟到20%甚至70%弦长之后。在这一小节，我们先简要介绍二维和三维边界层的失稳与转捩研究现状，最后再总结目前已经提出的转捩推迟手段。

1.2.1　二维边界层失稳与转捩

边界层转捩过程强烈依赖于来流条件和壁面条件，受到来流湍流度、来流马赫数、外流压力梯度、壁面温度、壁面粗糙度、壁面抽吸量及外部扰动特征参数等诸多因素的影响**??**，因此存在着多种物理机制。在二维不可压缩边界层中，转捩过程可分为以下三种类型：当来流湍流度较低（小于0.1%）时发生的是自然转捩（natural transition）**??**；而来流湍流度较高（大于1%）时，转捩过程中小扰动的指数增长阶段将被跳过，这被称为跨越转捩（bypass transition）**??**；逆压梯度会导致层流边界层与壁面分离，从而引发分离流转捩（separation-induced transition）**??**；反过来，顺压梯度会使湍流边界层再层流化**??**。具体地，自然转捩过程分为四个阶段**??**：第一阶段是所谓的边界层感受性过程（Receptivity）**??**，指的是背景扰动如何进入边界层并产生不稳定波的机制；第二阶段是不稳定波的线性增长过程；第三阶段是不稳定波发展的非线性阶段，不稳定波发展到一定的幅值后，会出现波的相互作用和高阶不稳定性，从而导致以湍斑为特征的湍流结构的产生；最后一个阶段是从湍斑到完全湍流的发展过程。在自然转捩的第二阶段，扰动幅值相比于基本流非常小，一般采用线性稳定性理论进行描述。该理论假设扰动具有行波的形式，且不同频率，不同波长的扰动波之间不会互相干扰。基于这一假设，我们可以得到线性稳定性方程（Orr-Sommerfeld方程）[9]，并且得到不同频率和波长的扰动波的衰减或增长的情况，如图1.2所示。在此图上，扰动的衰减（稳定）区和放大（不稳定）区可通过的扰动增长率等于零的线区分出来，这条线被称为中性稳定性曲线。令人特别关注的是曲线上取最小值的点：小于此值的区域内，所有的扰动均会趋于稳定。这个最小的雷诺数被称为临界雷诺数。可见，速度剖面有拐点的边界层比没有的更不稳定，而且后者在时仍存在不稳定频带，因此也被称为具有“无粘不稳定性”的剖面。实际上，上述频带可通过求

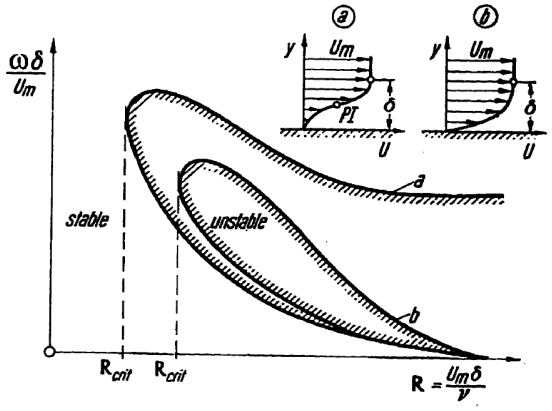

图 1.2　二维边界层中二维扰动的中性稳定性曲线，引自[10]。图中，a曲线对应的是具有拐点PI的速度剖面a，而b曲线对应的是无拐点的速度剖面b。

解Rayleigh方程[10]得到，此方程是Orr-Sommerfeld方程在时的简化形式，基于此方程的理论被称为“无粘稳定性理论”。无粘稳定性理论中的拐点定理指出拐点的存在是流动失稳的充分必要条件。

1.2.2　三维边界层失稳与转捩

三维边界层转捩的研究起始于后掠层流机翼设计项目[11]，其目标是大幅降低机翼阻力。几十年来航空界一直致力于这一项目，然而由于三维边界层的稳定性涉及到边界层对自由流中的扰动与机翼表面粗糙度的感受性、基频扰动及其谐波与驻涡（crossflow vortices）等多种模态之间的相互作用等诸多问题，目前的研究与实际应用还有着相当的距离。三维不可压缩边界层具有多种失稳机制，其中横流不稳定性起主导作用。图2.2显示了后掠机翼上的层流边界层流动。可见，由于沿机翼弦向压力梯度的存在，边界层外缘流线将发生扭曲，或者认为此处流体微团曲线运动产生的离心力与压力平衡。而在边界层内，流体微团的速度沿壁面法向逐渐减小，因此其产生的离心力减小，而压力却保持不变，这种不平衡性导致了垂直于主流方向的横流（crossflow velocity）的出现。横流速度剖面存在拐点并因此产生了横流不稳定波，其增长率比T-S波大得多。最不稳定波的方向几乎与势流方向垂直（85o～89o），波长是边界层厚度的三倍到四倍[13]。在极限条件时，零频率的波驻留在物面上，它们具有恒定相位线，方向近似与来流平行，被称为驻涡。横流失稳模态可分为驻涡模态与行波（traveling waves）模态两种。Malik[44]等人通过对后掠Hiemenz流动NPSE的计算得出行涡模态与驻涡模态的主导关系，他们指出当行涡模态的初始幅值小于驻涡模态初始幅值一个数量级时，驻涡模态扰动主导横流转捩；反之，转捩则由行波模态扰动引起，并且行涡会在发展过程中抑制驻涡的发展。这一计算结果与Bippes[43]年提出的低湍流情况横流

驻涡主导转捩，高湍流情况横流行涡主导转捩的结论相吻合。由于横流失稳产生的横流涡亦是不稳定，所以在其基础之上会产生二次失稳。Malik[45]研究了后掠翼上转捩前扰动波的发展，其计算结果与Reibert[47]的实验结果符合的很好，并在此基础上研究了饱和的横流涡的二次失稳现象。他们将二次失稳的模态根据能量来源的不同分为Y模态和Z模态。下图为Y模态与Z模态的扰动幅值等值线：

Z模态（上图）与Y模态（下图）与此同时，他们还提出了基于二次失稳理论N转捩因子的预测方法。Haynes [47]等人研究了雷诺数和曲率对于后掠翼上流动稳定性的影响，发现雷诺数越大横流涡饱和越早，雷诺数非常小时甚至不会出现横流涡的饱和现象；另外横流涡的发展对曲率的敏感性也很大。Li[48]等人对横流行涡的二次失稳也做了详细的研究，他们发现行涡的增长率相比于驻涡更大，并且在更低的幅值饱和，而二次失稳的幅值却不亚于驻涡，所以只有在行涡的初始幅值很低的时候才是驻涡主导转捩。由于横流失稳是导致后掠翼转捩的主要机制，所以近些年研究者们也在试图通过影响横流失稳产生扰动的发展推迟转捩。Saric[49]在试验中发现，通过采用在机翼前缘放置一排间距略小于最不稳定横流涡展向波长的粗糙单元，可以有效的推迟转捩。这是因为该粗糙单元激发出的模态本身并不会发展导致转捩，相反其还会抑制最不稳定模态，从而推迟转捩。Malik[45]的计算也给出了相同的解释。不同模态幅值在不同初始值条件下的发展如下图：

其中实线是控制模态和自然模态同时存在时它们的幅值沿着流向发展的情况，虚线是只有自然模态时的情况。可以看到在有控制模态的时候自然扰动模态的发展受到了抑制。Carpenter（2008）年做了利用粗糙单元推迟转捩的飞行试验，实验发现在翼型前缘表面没有打磨得很光滑的时候该方法是有效的，2009年F.Li用NPSE进行计算也得到了相同的结果。2013年，Templemann[50]用DNS的进行模拟，同样印证了该方法的可行性。2014年Lovig[51]等人在湍流度更低的风洞（来流湍流度0.04Friederich 和Kloker[52]提出了一种吸气的控制方法来推迟横流诱发的转捩并在后掠平板上得到了验证。他们通过在横流涡卷起的地方向下吸气，从而破坏横流涡的结构，使得二次失稳受到抑制。这一方法还有待实验的检验以及向更加便于应用的方向改变。在实验方面，处于前沿的研究者为亚利桑那州立大学（ASU）的Saric、俄罗斯的Kachanov、日本宇航实验室的Tagagi以及德国宇航研究院（DLR）的Bippes。Saric[14]综述了三维不可压缩边界层的感受性、二次失稳和壁面粗糙度效应等热点问题的最新进展。目前，数值模拟方面使用较多的还是线性稳定性理论和NPSE方法。目前线性稳定性理论可以准确预测出驻涡模态及其波长。Reed对

这方面的研究进行了总结[15]。NPSE方法的优势是其具有模拟非平行和非线性效应的能力[16]，Haynes和Reed综述了此法对几种典型的三维不可压缩边界层流动的研究结果[17]。直接数值模拟方面，Reed和Lin[18-19]研究了无限展长后掠翼上的转捩过程，结果与ASU的实验符合较好。Meyer和Kleiser[20]考察了横流不稳定性的驻涡模式与行波模式的扰动在后掠平板上的相互作用，他们采用与Muller和Bippes[21]的实验近似的初始条件，得到了合理的三维边界层转捩发展过程。Wintergerste和Kleiser[22]对他们的工作进行了补充，重点研究转捩后期横流涡的破碎现象。

1.2.3　转捩推迟方案研究进展

转捩推迟方案研究进展

1.3　通过控制壁湍流相干结构减阻

1.3.1　湍流相干结构研究进展

壁湍流相干结构研究进展

1.3.2　湍流减阻技术研究进展

湍流减阻技术研究进展

第2章　理论公式与数值求解方法

2.1　等离子体模型

2.2　流动稳定性求解框架

在研究等离子体控制扰动的问题中，本文采用研究稳定性问题的相关数值方法，来解析控制前后边界层内扰动的发展情况。稳定性的相关理论虽然并不能给出精确的转捩位置，但是能够从理论方面给出流动失稳特性，并且具有计算效率高，转捩前流动解析精度高的优点。本文中通过研究流动在控制前后稳定性方面的特性变化，来甄别控制是否有效。本文采用的研究边界层流动稳定性的步骤如下：

1. 采用高精度有限元程序求解无粘流场；
2. 以无粘流壁面上的流动参数作为边界层方程的边界条件，求解层流基本流动；
3. 基于线性稳定性理论，判断主导转捩的模态；
4. 采用抛物化扰动方程，求解边界层内扰动的演化；
5. 以受扰流场作为新的基本流动进行二次失稳分析。

与前人所做的研究不同的是，本文的研究需要将等离子体产生的体积力也考虑进来。在详细介绍求解方法之前，这里先简要介绍一下本文中对体积力的处理方法。流动所满足的控制方程（N-S方程）为：

$$\left.\begin{aligned}
\frac{\partial \rho^*}{\partial t^*} + \nabla^* \cdot (\rho^* \mathbf{V}^*) &= 0 \\
\rho^* \left(\frac{\partial \mathbf{V}^*}{\partial t^*} + (\mathbf{V}^* \cdot \nabla^*) \mathbf{V}^* \right) &= -\nabla^* p^* + \nabla^* (\lambda^* (\nabla^* \cdot \mathbf{V}^*)) \\
&\quad + \nabla^* \cdot \left(\mu^* \left(\nabla^* \mathbf{V}^* + \nabla^* \mathbf{V}^{*T} \right) \right) + \mathbf{f}^* \\
\rho^* C_p{}^* \left(\frac{\partial T^*}{\partial t^*} + (\mathbf{V}^* \cdot \nabla^*) T^* \right) &= \nabla^* \cdot (\kappa^* \nabla^* T^*) \\
&\quad + \frac{\partial p^*}{\partial t^*} + (\mathbf{V}^* \cdot \nabla^*) p^* + \Phi^* + \mathbf{V}^* \cdot \mathbf{f}^*
\end{aligned}\right\} \tag{2-1}$$

式（2-1）中能量方程的耗散函数为：

$$\Phi^* = \lambda^* (\nabla^* \cdot \mathbf{V}^*)^2 + \frac{\mu^*}{2} \left(\nabla^* \mathbf{V}^* + \nabla^* \mathbf{V}^{*T} \right)^2 \tag{2-2}$$

方程中星号 $*$ 表示有量纲量，$\mathbf{V}$ 表示速度矢量，其在x, y, z三个方向的分量为 u，v，w 。$\mathbf{f}$ 表示体积力矢量，其分量分别为 f_x，f_y，f_z 。

为封闭 N-S 方程，分别引入状态方程、Sutherland 粘性律、Stokes 假设，假定流体是量热完全气体并具有恒定的 Pr 数：

$$\left.\begin{aligned} p^* = \rho^* R^* T^* \Leftrightarrow p = \frac{\rho T}{\gamma M a^2} \\ \mu^* = \mu_s^* \frac{T^*}{T_s^*} \frac{T_s^* + S^*}{T^* + S^*} \Leftrightarrow \mu = \mu_s \frac{T}{T_s} \frac{T_s + S}{T + S} \\ \lambda^* + 2/3\mu^* = 0 \Leftrightarrow \lambda = -2/3\mu \\ \mathrm{Pr} = \frac{{C_p}^* \mu^*}{\kappa^*} = const \Leftrightarrow \mu = \kappa \\ C_p^* = const, R^* = const \end{aligned}\right\} \tag{2-3}$$

Sutherland 粘性律中 $T_s^* = 273K,\ \mu_s^* = 1.71 \times 10^{-5} kg/(m \cdot s),\ S^* = 110.4K$。

选取适当的参考长度 l_{reff}、参考速度 U_{reff}、参考密度 ρ_{reff}等特征量，可以对式（2-1）进行无量纲化。在本文中，分别研究了后掠Hiemenz流动和后掠翼流动。在这两个流动中我们选择的特征量是不一样的，之后我们会分别介绍。为了简洁，我们将无量纲化后的N-S方程记为：

$$\mathscr{N}(\mathbf{q}) = \mathbf{F} \tag{2-4}$$

这里，$\mathbf{q} = (\rho, u, v, w, T)^T$，即原始变量组成的5维矢量。$\mathbf{F} = (0, f_x, f_y, f_z, \mathbf{V} \cdot \mathbf{f})^T$。上标 "$T$" 表示转置。这里由于添加的体积力很小，我们假设其只影响扰动发展，并不影响基本流。即基本流依然满足N-S方程：

$$\mathscr{N}(\mathbf{q_0}) = 0 \tag{2-5}$$

$\mathbf{q_0}$ 为基本流流动原始变量组成的矢量，其与$\mathbf{q}$的差即为扰动量$\tilde{\mathbf{q}}$。令式(2-4) - 式(2-5)，即可得到扰动的控制方程：

$$\mathscr{S}(\tilde{\mathbf{q}}) = \mathscr{N}(\mathbf{q_0} + \tilde{\mathbf{q}}) - \mathscr{N}(\mathbf{q_0}) = \mathbf{F} \tag{2-6}$$

在之后的小节2.2.1和2.2.2中，将会分别介绍式（2-5）和（2-6）所采用的求解方法。至于求解步骤1中提到的高精度有限元方法，将会在2.3节中介绍。

2.2.1　边界层方程

在边界层流动中，流向的特征尺度为常规尺度，而法向的特征尺度为边界层厚度尺度。利用这一特性，可将Navier-Stokes 方程式抛物化，得到层流边界层控制方程。本文研究的问题的基本流均满足展向均匀假设，即$\partial/\partial z^* = 0$。利用这些假设，式（2-5）可以写为[①]：

$$\frac{\partial(\rho^* u^*)}{\partial x^*} + \frac{\partial(\rho^* v^*)}{\partial y^*} = 0 \tag{2-7a}$$

$$\rho^* u^* \frac{\partial u^*}{\partial x^*} + \rho^* v^* \frac{\partial u^*}{\partial y^*} = -\frac{\partial p^*}{\partial x^*} + \frac{\partial}{\partial y^*}\left(\mu^* \frac{\partial u^*}{\partial y^*}\right) \tag{2-7b}$$

$$\rho^* u^* \frac{\partial w^*}{\partial x^*} + \rho^* v^* \frac{\partial w^*}{\partial y^*} = \frac{\partial}{\partial y^*}\left(\mu^* \frac{\partial w^*}{\partial y^*}\right) \tag{2-7c}$$

$$\frac{\partial p^*}{\partial y^*} = 0 \tag{2-7d}$$

$$\rho^* u^* C_p^* \frac{\partial T^*}{\partial x^*} + \rho^* v^* C_p^* \frac{\partial T^*}{\partial y^*} = \frac{\partial}{\partial y^*}\left(k^* \frac{\partial T^*}{\partial y^*}\right) + u^* \frac{\partial p^*}{\partial x^*} + \mu^* \left(\frac{\partial u^*}{\partial y^*}\right)^2 + \mu^* \left(\frac{\partial w^*}{\partial y^*}\right)^2 \tag{2-7e}$$

在传统的边界层方程求解方法中，所有物理量都采用相同的参考量进行无量纲化，比如一般会采用来流的速度、密度等物理量进行无量纲化。然而，在本文研究的问题中，边界层外普遍有较大的压力梯度，这导致不同流向位置的边界层外物理量差异比较大，计算很难收敛。所以本文采用当地边界层外的物理量，即$U_e^*, T_e^*, \rho_e^*, k_e^*, \mu_e^*$，进行无量纲化，提高计算稳定性。这里边界层外的物理量是通过求解无粘流方程得到的，并作为边界层方程求解的边界条件。采用当地边界层外物理量无量纲化后的边界层方程为：

$$\frac{\partial(\rho u)}{\partial x^*} + \frac{\partial(\rho v)}{\partial y^*} + \frac{\rho u}{\rho_e^* U_e^*} \frac{\partial\left(\rho_e^* U_e^*\right)}{\partial x^*} = 0 \tag{2-8a}$$

$$\rho u \rho_e^* U_e^* U_e^* \frac{\partial u}{\partial x^*} + \rho u u \rho_e^* U_e^* \frac{\partial U_e^*}{\partial x^*} + \rho v \rho_e^* U_e^* U_e^* \frac{\partial u}{\partial y^*} = \rho_e^* U_e^* \frac{dU_e^*}{dx^*} + \mu_e^* U_e^* \frac{\partial}{\partial y^*}\left(\mu \frac{\partial u}{\partial y^*}\right) \tag{2-8b}$$

$$\rho u \frac{\partial w}{\partial x^*} + \rho v \frac{\partial w}{\partial y^*} = \frac{\mu_e^*}{\rho_e^* U_e^*} \frac{\partial}{\partial y^*}\left(\mu \frac{\partial w}{\partial y^*}\right) \tag{2-8c}$$

① 本节讨论的均为基本流的计算方法，为了简洁，表明基本流变量的下标0在本节中都被略去。即原本的$\rho_0, u_0, v_0, w_0, T_0$在本节被记为$\rho, u, v, w, T$。有量纲量类似。

$$\rho u\rho_e^* U_e^* C_p^* \left(T\frac{\partial T_e^*}{\partial x^*} + T_e^* \frac{\partial T}{\partial x^*}\right) + \rho v \rho_e^* U_e^* C_p^* T_e^* \frac{\partial T}{\partial y^*}$$
$$= k_e^* T_e^* \frac{\partial}{\partial y^*}\left(k\frac{\partial T}{\partial y^*}\right) - \rho_e^* U_e^* U_e^* \frac{dU_e^*}{x^*} u + \mu\mu_e^* U_e^* U_e^* \left(\frac{\partial u}{\partial y^*}\right)^2 + \mu\mu_e^* W_e^* W_e^* \left(\frac{\partial w}{\partial y^*}\right)^2 \quad (2\text{-}8d)$$

注意到在上面的代换中，还用到了无粘势流中沿流线的伯努利方程：

$$-\frac{\partial p^*}{\partial x^*} = \rho^* u_e^* \frac{du_e^*}{dx_e^*} \quad (2\text{-}9)$$

和气体状态方程：

$$\rho T = 1 \quad (2\text{-}10)$$

为了消除上述边界层方程在驻点处的奇异性，引入如下相似变换：

$$\xi = x^* \quad (2\text{-}11a)$$
$$\eta = \sqrt{\frac{U_e^*}{x^* \rho_e^* \mu_e^*}} \int_0^{y^*} \rho^* dy^* = \frac{1}{L^*} \int_0^{y^*} T^{-1} dy^* \quad (2\text{-}11b)$$

最终得到如下计算求解的方程：

$$\xi\frac{\partial u}{\partial \xi} + \frac{\partial \Lambda}{\partial \eta} + \frac{u}{2}\left[1 + \frac{\xi}{\mu_e^*}\frac{\partial \mu_e^*}{\partial \xi} + \frac{\xi}{\rho_e^* \mu_e^*}\frac{\partial(\rho_e^* \mu_e^*)}{\partial \xi}\right] = 0 \quad (2\text{-}12a)$$

$$\xi u\frac{\partial u}{\partial \xi} + \Lambda\frac{\partial u}{\partial \eta} - \frac{\xi}{\mu_e^*}\frac{\partial \mu_e^*}{\partial \xi}(T - u^2) = \frac{\partial}{\partial \eta}\left(\frac{\mu}{T}\frac{\partial u}{\partial \eta}\right) \quad (2\text{-}12b)$$

$$\xi u\frac{\partial w}{\partial \xi} + \Lambda\frac{\partial w}{\partial \eta} = \frac{\partial}{\partial \eta}\left(\frac{\mu}{T}\frac{\partial w}{\partial \eta}\right) \quad (2\text{-}12c)$$

$$\xi u\frac{\partial T}{\partial \xi} + \Lambda\frac{\partial T}{\partial \eta} - \frac{1}{\mathrm{Pr}}\frac{\partial}{\partial \eta}\left(\frac{k}{T}\frac{\partial T}{\partial \eta}\right) = (\gamma - 1)\frac{\mu}{T}\left[(\mathrm{Ma}_{ue}\frac{\partial u}{\partial \eta})^2 + (\mathrm{Ma}_{we}\frac{\partial w}{\partial \eta})^2\right] \quad (2\text{-}12d)$$

其中：

$$L^* = \sqrt{\frac{\mu_e^* x^*}{\rho_e^* u_e^*}} \tag{2-13a}$$

$$\Lambda = \xi u \frac{\partial \eta}{\partial x^*} + \frac{\xi v}{L^* T} \tag{2-13b}$$

$$\mathrm{Ma}_{ue} = \frac{u_e^*}{a_e^*} \tag{2-13c}$$

$$\mathrm{Ma}_{we} = \frac{w_e^*}{a_e^*} \tag{2-13d}$$

$$a_e^* = \sqrt{\gamma R T_e^*} \tag{2-13e}$$

将方程（2-12）在法方向采用谱方法进行离散，流向采用五阶差分格式，最后得到离散的方程简记为：

$$L_{dis}(\Phi) = 0 \tag{2-14}$$

$\Phi = (u, w, \Lambda, T)^T$为方程（2-12）中实际求解的变量组成的矩阵。上式对应的Jacobian矩阵为：

$$\mathbf{J}_b = \frac{\partial L_{dis}(\Phi)}{\partial \Phi} \tag{2-15}$$

本文采用拟牛顿法对式（2-14）进行求解，迭代更新方法如下：

$$\Phi_{\mathrm{new}} = \Phi_{\mathrm{old}} - \mathbf{J}_b^{-1} L_{dis}(\Phi) \tag{2-16}$$

式（2-14）和（2-15）的具体形式将在附录A中给出。

为了验证程序是否正确，首先将计算结果与零压力梯度平板上的相似性解进行对比。这里采用的计算工况为：

$$U_\infty = 100\mathrm{m/s}, T_\infty = 300\mathrm{K}, \nu_\infty = 1.5 \times 10^{-5}\mathrm{m^2/s} \tag{2-17}$$

对比$x = 1\mathrm{m}$，即$Re_x = 6.67 \times 10^6$，位置处各个物理量延法向的分布如图2.1所示。其中黑色由方框标记的线为边界层方程求解出来的结果，红色由三角标记出来的先为相似性解的结果。可以看到两种算法的结果几乎完全重合了。

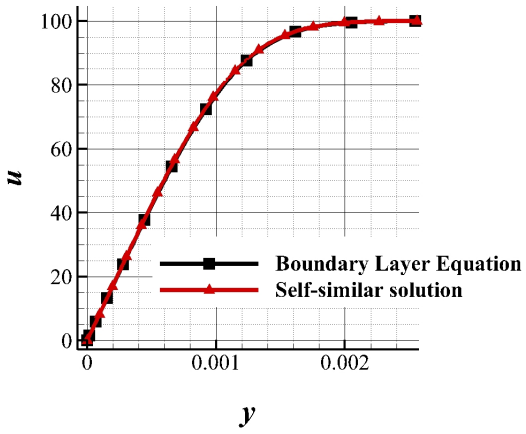

(a) 流向速度对比

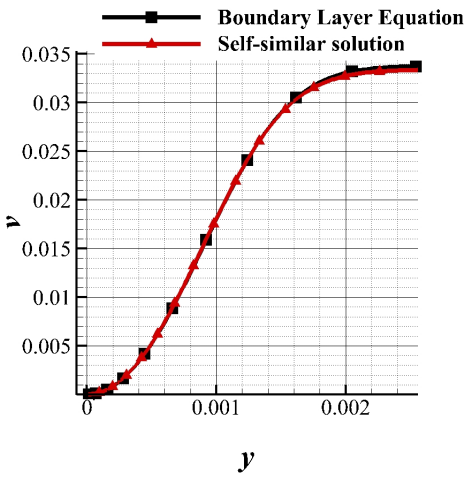

(b) 法向速度对比

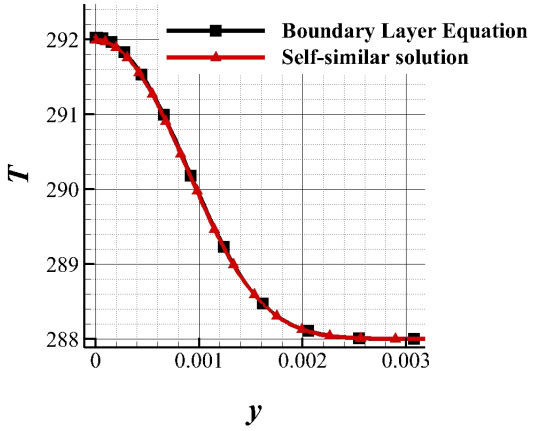

(c) 温度对比

图 2.1　边界层方程计算结果与相似性解对比（黑线方框标记：边界层方程计算结果；红线三角标记：相似性解）

本文中主要进行的是三维边界层失稳的研究，所以针对三维边界层的计算也需要验证。清华大学徐胜金老师课题组为研究三维边界层转捩在低湍流度风洞中做了后掠NLF-0415翼型的绕流实验。实验相应参数可以参考文献？？？？？。在实验自由来流为22.3m/s的工况中，翼型上表面直至70%弦长处均为层流。采用边界层方程计算速度分布，并取40%和60%弦长处的速度剖面与实验对比，结果如图2.2。其中计算结果用线表示，实验结果用点表示。这里U_{wt}表示延风洞方向的速度分量[①]。蓝色表示20%弦长处的结果，红色为40%处。从计算的结果可以看到，我们所采用的求解方法完全满足精度需求。

① 注意这里并不是u，因为在后掠翼计算中，x方向与平行于风洞的流向有45°夹角

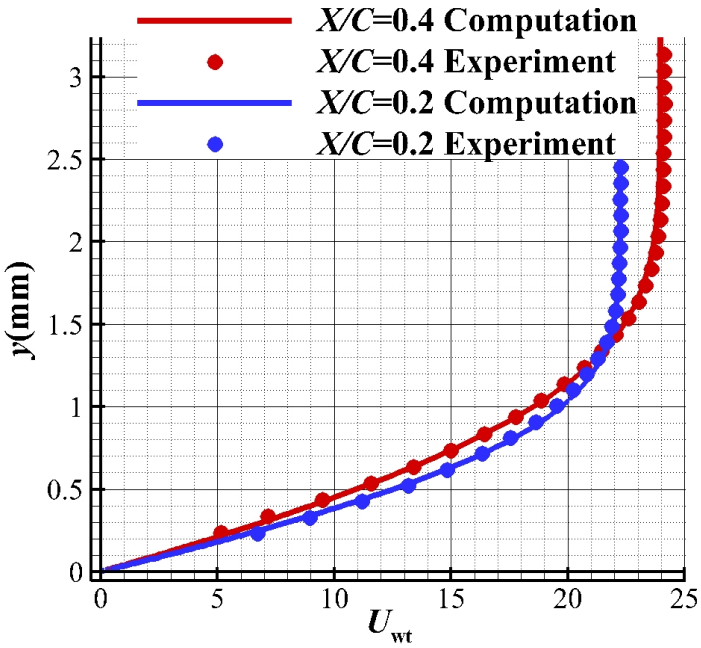

图 2.2　后掠翼上边界层速度剖面对比（线：计算结果；点：实验结果）

2.2.2　扰动方程

如之前所述，本文将流场基本变量 $\mathbf{q} = (\rho,\ u,\ v,\ w,\ T)$ 分解为基本流动 $\mathbf{q}_0$ 和扰动 $\tilde{\mathbf{q}}$ 两部分：

$$\mathbf{q}(x, y, z, t) = \mathbf{q}_0(x, y) + \tilde{\mathbf{q}}(x, y, z, t) \tag{2-18}$$

在小节2.2.1中已经探讨了基本流动的求解方法。在这一节中，重点讨论扰动方程（2-6）的求解方法。先假设方程（2-6）可以写成如下紧凑的形式：

$$\begin{aligned}&\boldsymbol{\Gamma}\frac{\partial\tilde{\mathbf{q}}}{\partial t} + \mathbf{A}\frac{\partial\tilde{\mathbf{q}}}{\partial x} + \mathbf{B}\frac{\partial\tilde{\mathbf{q}}}{\partial y} + \mathbf{C}\frac{\partial\tilde{\mathbf{q}}}{\partial z} + \mathbf{D}\tilde{\mathbf{q}}\\ &\quad = \mathbf{H}_{xx}\frac{\partial^2\tilde{\mathbf{q}}}{\partial x^2} + \mathbf{H}_{yz}\frac{\partial^2\tilde{\mathbf{q}}}{\partial z\,\partial y} + \mathbf{H}_{xy}\frac{\partial^2\tilde{\mathbf{q}}}{\partial x\,\partial y} + \mathbf{H}_{xz}\frac{\partial^2\tilde{\mathbf{q}}}{\partial x\,\partial z} + \mathbf{H}_{yy}\frac{\partial^2\tilde{\mathbf{q}}}{\partial y^2} + \mathbf{H}_{zz}\frac{\partial^2\tilde{\mathbf{q}}}{\partial z^2} + \mathbf{N} + \mathbf{F}.\end{aligned} \tag{2-19}$$

其中 5×5 系数矩阵 $\boldsymbol{\Gamma}$, $\mathbf{A}$, $\mathbf{B}$, $\mathbf{C}$, $\mathbf{D}$, $\mathbf{H}_{xx}$, $\mathbf{H}_{yy}$, $\mathbf{H}_{zz}$, $\mathbf{H}_{xy}$, $\mathbf{H}_{xz}$, $\mathbf{H}_{yz}$ 是基本流动、流向曲率和 Re, Ma, Pr 的函数，详细表达式可参见附录B。向量 $\mathbf{N}$ 表示非线性项，$\mathbf{F}$表示体积力产生的源项。

2.2.2.1　线性稳定性理论

由于边界层流动中，边界层厚度增长缓慢，所以可将其近似为平行剪切流。假设扰动具有行波解：

$$\tilde{\mathbf{q}}(x,y,z,t)=\hat{\mathbf{q}}(y)\exp\left(\mathrm{i}(\alpha x+\beta z-\omega t)\right)+c.c. \tag{2-20}$$

针对边界层失稳问题，其不稳定性通常是对流失稳，即边界层内的扰动并不是在原地增长，而是一边向下游传播一遍增长。针对这一类问题，通常采用空间模式求解，即给定 β 和 ω，求解α。将式（2-20）代入扰动方程（ 2-19），忽略非线性项整理得到

$$\mathbf{A}_L\hat{\mathbf{q}}+\mathbf{B}_L\frac{\partial\hat{\mathbf{q}}}{\partial y}-\mathbf{H}_{yy}\frac{\partial^2\hat{\mathbf{q}}}{\partial y^2}=\alpha\left(\mathbf{M}_L\hat{\mathbf{q}}+\mathrm{i}\mathbf{H}_{xy}\frac{\partial\hat{\mathbf{q}}}{\partial y}\right)-\alpha^2\mathbf{H}_{xz}\hat{\mathbf{q}} \tag{2-21}$$

其中

$$\left.\begin{aligned}\mathbf{A}_L&=-\mathrm{i}\omega\mathbf{\Gamma}+\mathrm{i}\beta\mathbf{C}+\mathbf{D}+\beta^2\mathbf{H}_{zz}\\ \mathbf{B}_L&=\mathbf{B}-\mathrm{i}\beta\mathbf{H}_{yz}\\ \mathbf{M}_L&=-\mathrm{i}\mathbf{A}-\beta\mathbf{H}_{xz}\end{aligned}\right\} \tag{2-22}$$

将上式中的几个微分算子记作：

$$\mathscr{L}_0=\mathbf{A}_L+\mathbf{B}_L\frac{\partial}{\partial y}-\mathbf{H}_{yy}\frac{\partial^2}{\partial y^2} \tag{2-23a}$$

$$\mathscr{L}_1=-\mathbf{M}_L-\mathrm{i}\mathbf{H}_{xy}\frac{\partial}{\partial y} \tag{2-23b}$$

$$\mathscr{L}_2=\mathbf{H}_{xz} \tag{2-23c}$$

则线性稳定性的控制方程可以写为：

$$\mathscr{L}\hat{\mathbf{q}}=\mathscr{L}_0\hat{\mathbf{q}}+\alpha\mathscr{L}_1\hat{\mathbf{q}}+\alpha^2\mathscr{L}_2\hat{\mathbf{q}}=0 \tag{2-24}$$

引入一个辅助变量：

$$\tilde{\mathbf{q}}_a=\alpha\tilde{\mathbf{q}} \tag{2-25}$$

则式（2-24）可以改写为：

$$\begin{pmatrix} 0 & 1 \\ \mathscr{L}_0 & \mathscr{L}_1 \end{pmatrix}\begin{pmatrix} \tilde{\mathbf{q}} \\ \tilde{\mathbf{q}}_a \end{pmatrix} = \alpha \begin{pmatrix} 1 & 0 \\ 0 & -\mathscr{L}_2 \end{pmatrix}\begin{pmatrix} \tilde{\mathbf{q}} \\ \tilde{\mathbf{q}}_a \end{pmatrix} \tag{2-26}$$

很显然，式(2-21)是针对微分算子的广义特征值问题。对其进行离散求解，在法方向采用四阶精度中心差分格式：

$$\left.\begin{aligned} \frac{\partial \hat{\mathbf{q}}_j}{\partial y} &= \frac{\hat{\mathbf{q}}_{j-2} - 8\hat{\mathbf{q}}_{j-1} + 8\hat{\mathbf{q}}_{j+1} - \hat{\mathbf{q}}_{j+2}}{12\Delta y} \\ \frac{\partial^2 \hat{\mathbf{q}}_j}{\partial y^2} &= \frac{-\hat{\mathbf{q}}_{j-2} + 16\hat{\mathbf{q}}_{j-1} - 30\hat{\mathbf{q}}_j + 16\hat{\mathbf{q}}_{j+1} - \hat{\mathbf{q}}_{j+2}}{12(\Delta y)^2} \end{aligned}\right\} \tag{2-27}$$

便可以将这一个微分算子的广义特征值问题转化为矩阵的广义特征值问题。求解该特征值问题，得到特征向量 $\hat{\mathbf{q}}$ 即为扰动分布，特征值 α 虚部 $-\alpha_i$ 为扰动增长率，实部 α_r 为扰动流向波数。

2.2.2.2　抛物化扰动方程

线性稳定性理论有两个缺陷。首先，其采用平行流假设，导致边界层延流向的变化被忽略了。另外，线性假设忽略了非线性项，导致不同模态间的相互作用没有被考虑。抛物化扰动方程（PSE）可以克服上述这两点缺陷，并且具有很高的求解效率。首先将物理扰动 $\tilde{\mathbf{q}}$ 和非线性项与外加源项之和 $\mathbf{N}+\mathbf{F}$ 进行 Fourier 展开：

$$\tilde{\mathbf{q}}(x,y,z,t) = \sum_{m=-M}^{M}\sum_{n=-N}^{N} \hat{\mathbf{q}}_{mn}(x,y)\,\Theta_{mn}, \tag{2-28}$$

$$\mathbf{N}+\mathbf{F} = \sum_{m=-M}^{M}\sum_{n=-N}^{N} \mathbf{S}_{mn}(x,y)\,\Theta_{mn}, \tag{2-29}$$

$$\Theta_{mn} = \exp\left(i\int_{x_0}^{x}\alpha_{mn}(\xi)\,d\xi + in\beta z - im\omega t\right). \tag{2-30}$$

其中Θ_{mn}是波数函数。代入扰动方程（2-19），整理得到

$$\hat{\mathbf{A}}\frac{\partial \hat{\mathbf{q}}_{mn}}{\partial x} + \hat{\mathbf{B}}\frac{\partial \hat{\mathbf{q}}_{mn}}{\partial y} + \hat{\mathbf{C}}\frac{\partial^2 \hat{\mathbf{q}}_{mn}}{\partial x^2} + \hat{\mathbf{D}}\hat{\mathbf{q}}_{mn} - \mathbf{H}_{yy}\frac{\partial^2 \hat{\mathbf{q}}_{mn}}{\partial y^2} = \mathbf{S}_{mn}, \tag{2-31}$$

其中

$$\begin{aligned}
\hat{\mathbf{A}} &= \mathbf{A} - 2i\alpha_{mn}\mathbf{H}_{xx} - in\beta\mathbf{H}_{xz},\\
\hat{\mathbf{B}} &= \mathbf{B} - i\alpha_{mn}\mathbf{H}_{xy} - in\beta\mathbf{H}_{yz},\\
\hat{\mathbf{C}} &= \mathbf{H}_{xx},\\
\hat{\mathbf{D}} &= \mathbf{D} - im\omega\mathbf{\Gamma} + i\alpha_{mn}\mathbf{A} + in\beta\mathbf{C} + \mathbf{H}_{xx}\left(\alpha_{mn}^2 - i\frac{d\alpha}{dx}\right) + n^2\beta^2\mathbf{H}_{zz} + n\beta\alpha_{mn}\mathbf{H}_{xz}.
\end{aligned} \tag{2-32}$$

根据量级分析[7]， $d\alpha/dx$ 这一项非常小可以忽略。为了使得形函数$\hat{\mathbf{q}}$在流向缓变，提出针对 α的波数迭代条件：

$$\int_0^{\infty} \hat{\mathbf{q}}^H \mathbf{M}\frac{\partial\hat{\mathbf{q}}}{\partial x}\,dy = 0 \qquad \forall x. \tag{2-33}$$

这里$\mathbf{M} = \mathrm{diag}(0,1,1,1,0)$， “$H$”表示复共轭。式（2-33）又可以叫做形函数的缓变条件，这一条件使得形函数在流向的二阶偏导数可以被忽略掉，即$\partial^2\hat{\mathbf{q}}_{mn}/\partial x^2 = 0$[8]。虽然二阶偏导数项被忽略掉了，但是方程（2-31）依然有一些残余椭圆性[9]。针对这一问题，将方程中的压力项修正为：

$$\frac{\partial\tilde{p}_{mn}}{\partial x} = i\alpha_{mn}\hat{p}_{mn}\Theta_{mn}. \tag{2-34}$$

采用上面所提到的诸多假设，方程（2-31）可以完全被抛物化，可以流向推进求解。完整的方程为：

$$\mathscr{L}_{\mathrm{PSE}}\hat{\mathbf{q}}_{mn} = \hat{\mathbf{A}}\frac{\partial\hat{\mathbf{q}}_{mn}}{\partial x} + \hat{\mathbf{B}}\frac{\partial\hat{\mathbf{q}}_{mn}}{\partial y} + \hat{\mathbf{D}}\hat{\mathbf{q}}_{mn} - \mathbf{H}_{yy}\frac{\partial^2\hat{\mathbf{q}}_{mn}}{\partial y^2} = \mathbf{S}_{mn}, \tag{2-35}$$

其中$\mathscr{L}_{\mathrm{PSE}}$线性PSE算子。本文对方程（2-35）在流向采用隐式欧拉差分，法向采用五阶中心差分进行离散求解。

为了验证程序的正确性，我们与Malik等人1994年的工作[8]进行对比。该工作重点研究了后掠Hiemenz流动的失稳，计算相关参数详见他们的文献。这里计算对比$\bar{R} = 500$①工况中主模态的能量在流向的演化，结果如图2.3示。

2.2.3　扰动发展的敏感性分析

为了更好地理解流动，同时选取较优化的控制参数，本文中对三维边

① 这个符号采用与文献[8]中相同的定义

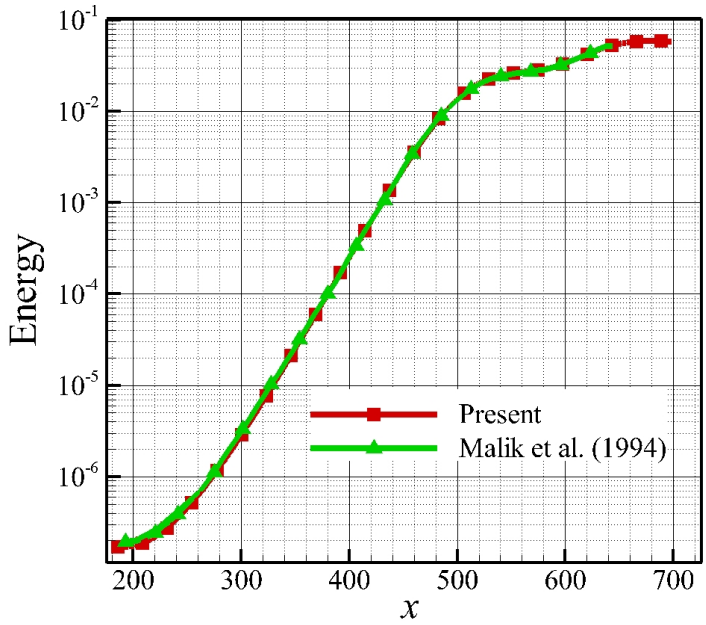

图 2.3　PSE计算程序验证

界层失稳进行了敏感性分析。关于流动失稳的敏感性分析最早始于2003年，是Bottaro[10]等人针对Couette流动开展的。通过求解线性稳定性问题的伴随问题，他们找出了容易受基本流变化影响的失稳模态。之后，2008年Marquet等人[11]分析了圆柱尾迹流动对于基本流和外加体积力的敏感性，并采用这一结果进行了优化，降低了尾迹的湍流度。Alizard等人[12]2010年，对角域流动进行了分析，得到了不同失稳模态的敏感函数（敏感因子）的空间分布。2011年Brandt等人[13]对平板边界层做了相应的敏感性分析，之后学者们又对D形圆柱[14]，空腔[15]，甚至湍流边界层的猝发过程进行了相应的分析[16]，更加深入的了解了其流动机理。本文分别从线性稳定性理论和抛物化扰动方程出发，推导他们的伴随方程，并进而分析三维边界层失稳的敏感性。

2.2.3.1　基于线性稳定性理论的敏感性分析

记方程（2-24）的伴随方程为：

$$\mathscr{L}^{+}\hat{\mathbf{p}} = \mathscr{L}_0^{+}\hat{\mathbf{p}} + \alpha\mathscr{L}_1^{+}\hat{\mathbf{p}} + \alpha^2\mathscr{L}_2^{+}\hat{\mathbf{p}} = 0 \tag{2-36}$$

伴随方程与原方程的关系是，对于任意向量$\mathbf{a}, \mathbf{b}$,都有：

$$\int_0^{+\infty} \mathbf{a}\cdot(\mathscr{L}\mathbf{b})^T dy = \int_0^{+\infty} (\mathscr{L}^{+}\mathbf{a})\cdot\mathbf{b}^T dy \tag{2-37}$$

若定义内积$< \mathbf{a}, \mathbf{b} >= \int_0^{+\infty} \mathbf{a} \cdot \mathbf{b}^T dy$,则有：

$$< \mathbf{a}, \mathscr{L}\mathbf{b} >=< \mathscr{L}^{+}\mathbf{a}, \mathbf{b} > \tag{2-38}$$

引入体积力后，方程变为：

$$\left[\mathscr{L}_0 + (\alpha + \delta\alpha)\mathscr{L}_1 + (\alpha + \delta\alpha)^2\mathscr{L}_2\right](\hat{\mathbf{q}} + \delta\hat{\mathbf{q}}) = \mathbf{F} \tag{2-39}$$

其中$\delta\alpha$和$\delta\hat{\mathbf{q}}$为因为引入体积力产生的特征值和特征向量的变化。由于本文中均采用的是微弱的体积力控制失稳，所以这两个量都是小量。将上式与伴随向量（伴随方程的解）做内积，并忽略高阶小量，得到：

$$\begin{aligned} < \hat{\mathbf{p}}, \mathbf{F} > &=< \hat{\mathbf{p}}, \left[\mathscr{L}_0 + (\alpha + \delta\alpha)\mathscr{L}_1 + (\alpha + \delta\alpha)^2\mathscr{L}_2\right](\hat{\mathbf{q}} + \delta\hat{\mathbf{q}}) > \\ &\approx< \hat{\mathbf{p}}, (\delta\alpha\mathscr{L}_1 + 2\delta\alpha\mathscr{L}_2)\hat{\mathbf{q}} > \end{aligned} \tag{2-40}$$

最终得到空间模式的复特征值关于体积力的敏感性为：

$$\delta\alpha \approx \frac{< \hat{\mathbf{p}}, \mathbf{F} >}{< \hat{\mathbf{p}}, (\mathscr{L}_1 + 2\mathscr{L}_2)\hat{\mathbf{q}} >} \tag{2-41}$$

2.2.3.2　基于抛物化扰动方程的的敏感性分析

The sensitivity is usually defined as the gradient of the input of a system with respect to the output. Here, we chose the body force as the input while the disturbance energy at outlet as the output. Previous stability investigations[11] have demonstrated that sensitivity analyses can provide the key control parameters. The present method for sensitivity analyses refers to the work by Pralits[17]. Since the mode interaction is not considered, the term $\mathbf{S}_{mn}$ in Eq. (2-35) only includes the body force term and excludes the nonlinear term. Thus, the governing equation of each mode is decoupled from the others, and thus the index *nm*, which denotes the spanwise wave number and frequency of the harmonic modes, can be discarded. Thus, the governing equation is written as the following:

$$\mathscr{L}\hat{\mathbf{q}} = \hat{\mathbf{A}}\frac{\partial\hat{\mathbf{q}}}{\partial x} + \hat{\mathbf{B}}\frac{\partial\hat{\mathbf{q}}}{\partial y} + \hat{\mathbf{D}}\hat{\mathbf{q}} - \mathbf{H}_{yy}\frac{\partial^2\hat{\mathbf{q}}}{\partial y^2} = \mathbf{S} \tag{2-42}$$

with the output defined as:

$$J = E = \left[\frac{1}{2}\int_0^{T_z}\int_0^{\infty}\tilde{\mathbf{q}}^H\mathbf{M}\tilde{\mathbf{q}}dydz\right]_{x=x_1} = \frac{1}{2}\int_0^{T_z}\int_0^{\infty}|\Theta_1|^2\,\hat{\mathbf{q}}_1^H\mathbf{M}\hat{\mathbf{q}}_1 dydz \tag{2-43}$$

The subscript '1' represents the quantities at the outlet. T_z is the spanwise wave length of the instability mode. Then we differentiate the output function, the governing equation (2-42) and the auxiliary condition (2-33) with respect to the control variables, namely the distributed body force, and the state variables α and $\hat{\mathbf{q}}$:

$$\begin{aligned}\delta J = &\frac{1}{2}\int_0^{T_z}\int_0^{\infty}|\Theta_1|^2\,\hat{\mathbf{q}}_1^H\mathbf{M}\delta\hat{\mathbf{q}}_1 dydz \\ &+\frac{1}{2}\int_0^{T_z}\int_0^{\infty}|\Theta_1|^2\,\hat{\mathbf{q}}_1^H\mathbf{M}\hat{\mathbf{q}}_1\left(\mathrm{i}\int_{x_0}^{x_1}\delta\alpha(x')dx'\right)dydz + c.c\end{aligned} \tag{2-44}$$

$$\mathscr{L}\delta\hat{\mathbf{q}} - \delta\mathbf{S} + \frac{\partial\mathscr{L}}{\partial\alpha}\delta\alpha\hat{\mathbf{q}} = 0 \tag{2-45}$$

$$\int_0^{\infty}\left(\delta\hat{\mathbf{q}}^H\mathbf{M}\frac{\partial\hat{\mathbf{q}}}{\partial x} + \hat{\mathbf{q}}^H\mathbf{M}\frac{\partial\delta\hat{\mathbf{q}}}{\partial x}\right)dy = 0 \tag{2-46}$$

Here, $c.c.$ is the complex conjugate of all the terms in the equation, x_0 and x_1 the streamwise coordinates of the inlet and the outlet, respectively. Next, we define the inner product of two arbitrary vectors $\mathbf{a}$ and $\mathbf{b}$ as the following:

$$<\mathbf{a},\mathbf{b}>=\int_0^{T_z}\int_{x_0}^{x_1}\int_0^{\infty}(\mathbf{a}^H\mathbf{b})dydxdz \tag{2-47}$$

A complex adjoint vector $\hat{\mathbf{q}}^*$ and a complex function $r^*(x)$ are then introduced. Taking inner product of the adjoint vector with Eq. (2-45) and $r^*(x)$ with Eq. (2-46), adding the complex conjugates of each term, we obtain the following identity:

$$\int_0^{T_z}\int_{x_0}^{x_1}r^*\int_0^{\infty}\left(\delta\hat{\mathbf{q}}^H\mathbf{M}\frac{\partial\hat{\mathbf{q}}}{\partial x} + \hat{\mathbf{q}}^H\mathbf{M}\frac{\partial\delta\hat{\mathbf{q}}}{\partial x}\right)dydxdz + <\hat{\mathbf{q}}^*,\mathscr{L}\delta\hat{\mathbf{q}} - \delta\mathbf{S} + \frac{\partial\mathscr{L}}{\partial\alpha}\delta\alpha\hat{\mathbf{q}}> + c.c. = 0 \tag{2-48}$$

Any arbitrary vector $\hat{\mathbf{q}}^*$ and complex function r^* can satisfy Eq. (2-48). To eliminate unnecessary terms, appropriate $\hat{\mathbf{q}}^*$ and r^* must be identified. First, we let the adjoint

vector satisfy the adjoint equation and the adjoint auxiliary condition shown in Eq. (2-50) and Eq. (2-49). Due to the parabolic feature of the original equation, this adjoint equation is also parabolic and can be solved using a marching scheme. The only difference is that this equation should be marched from the outlet to the inlet.

$$\mathscr{L}^*\hat{\mathbf{q}}^* = (\bar{r}^* - r^*)\,\mathbf{M}\frac{\partial\hat{\mathbf{q}}}{\partial x} + \frac{\partial\bar{r}^*}{\partial x}\mathbf{M}\hat{\mathbf{q}} \tag{2-49}$$

$$\int_0^\infty \left(\hat{\mathbf{q}}^{*H}\frac{\partial\mathscr{L}}{\partial\alpha}\hat{\mathbf{q}}\right)dy = \int_0^\infty \mathrm{i}\,|\Theta_1|^2\,\hat{\mathbf{q}}_1^H\mathbf{M}\hat{\mathbf{q}}_1\,dy \tag{2-50}$$

the $\mathscr{L}^*$ is the adjoint operator of the linear PSE and the bar overhead means complex conjugate. The initial value of the adjoint vector and the function r^* at the outlet is shown below:

$$\begin{aligned} c &= \frac{-\int_0^\infty \mathrm{i}\,|\Theta_1|^2\,\hat{\mathbf{q}}_1^H\mathbf{M}\hat{\mathbf{q}}_1\,dy}{\int_0^\infty \left(\hat{\mathbf{q}}_1^H\mathbf{M}\left(\hat{\mathbf{A}}\right)^{-1}\frac{\partial\mathscr{L}}{\partial\alpha}\hat{\mathbf{q}}\right)dy\Big|_{x=x_1}} \\ \hat{\mathbf{q}}_1^* &= -\bar{c}\left(\hat{\mathbf{A}}^H\right)^{-1}\mathbf{M}\hat{\mathbf{q}}_1 \\ r_1^* &= c + |\Theta_1|^2 \end{aligned} \tag{2-51}$$

If the adjoint vector and r^* satisfy the Eq. (2-49) (2-50) and (2-51), Eq. (2-48) can be written as follows:

$$\delta J = \frac{1}{2} < \hat{\varphi}^*, \delta\mathbf{S} > + c.c. \tag{2-52}$$

To investigate the body-force effect on the disturbance energy growth in boundary layers, **F** and **S** are set to zero for the unexcited case. The variation of the output is thus exactly the difference between the unexcited and excited cases. The variation of the body force can be expressed as the following:

$$\delta\mathbf{F} = \Theta\delta\mathbf{S} + \mathbf{S}\mathrm{i}\int_{x_0}^{x}\delta\alpha(x')dx' = \Theta\delta\mathbf{S} \tag{2-53}$$

According to Eq. (2-53), Eq. (2-52) can be rewritten as follows:

$$\delta J = \frac{1}{2} < \hat{\varphi}^*, \frac{\delta \mathbf{F}}{\Theta} > + c.c. \tag{2-54}$$

Note that the body force term is simply a Fourier component of the total physical force because we only focus on one instability mode. To compute the variation of the kinetic energy caused by a spanwise periodical body force, the first step is to transform it into a Fourier space and then extract the corresponding component as the body-force term. Taking this transformation into account and expanding Eq. (2-54), the variation of the disturbance kinetic energy is expressed in the following Integral form:

$$\delta J = \int_0^{T_z} \int_{x_0}^{x_1} \int_0^{\infty} \left(G_u \delta f_x + G_v \delta f_y + G_w \delta f_z \right) dy dx dz \tag{2-55}$$

$$\begin{aligned} G_u &= \text{real}(\hat{u}^{*H} \exp(-\text{i} \int_{x_0}^{x} \alpha(x') dx' - in\beta z)) \\ G_v &= \text{real}(\hat{v}^{*H} \exp(-\text{i} \int_{x_0}^{x} \alpha(x') dx' - in\beta z)) \\ G_w &= \text{real}(\hat{w}^{*H} \exp(-\text{i} \int_{x_0}^{x} \alpha(x') dx' - in\beta z)) \end{aligned} \tag{2-56}$$

Here the three coefficient, G_u, G_v and G_w, are sensitivity functions that indicate the disturbance sensitivity to the body force.

2.3　充分发展槽道的直接数值模拟

第3章　后掠Hiemenz流动的失稳分析与控制

后掠Hiemenz流动与后掠翼上的三维边界层流动非常相似，是非常好的模型流动。本文从这一流动出发，研究三维边界层的横流失稳。原始的二维Hiemenz流动就是一股平面射流，自上而下打到一块平板上，并向平板两边溢流开来。在无粘流的假设下，这与直角的角域流动完全等价。因此，我们可以通过构造幂指数复势解得到无粘的Hiemenz流动的流场分布。这里，将无粘流动壁面上的流速分布作为边界层外缘的速度分布。这一分布的流向速度分量是线性增加的，如式（3-1）。式中上标'†'表示有量纲量，c是一个常系数。在二维Hiemenz流动的基础上，引入展向均匀的流动，就是后掠Hiemenz流动，如图（3.1）所示。有一些研究主要着眼于其附着线的失稳研究[18,19]，本文重点分析研究远离附着线区域的横流转捩问题。研究区域如图（3.1）中虚线所示。Malik等人[8]对这一问题的首次失稳和二次失稳做了充分的研究，本文的控制算例也是以他们研究过的工况作为基准算例。本文中采用与文献中[8]相同的方法求得这一流动的自相似解，并以此作为基本流。

$$U_\infty = cx^\dagger \tag{3-1}$$

在后掠Hiemenz流动中，引入的边界层外缘展向速度W_∞在所有流向位置是相同的，因此将这一速度选作参考速度。Malik等人在研究这一问题时，也采用这一速度作为参考速度。$l^\dagger = (\nu/c)^{\frac{1}{2}}$ 可以用来表征边界层厚度，本文在这个算例中用这个长度作为参考长度。以W_∞作为参考长度定义的雷诺数叫做横流雷诺数，$Re_W = W_\infty l^\dagger/\nu$，这个雷诺数在Malik等人的文章[8]中被记做$\bar{R}$。

3.1　后掠Hiemenz流动的稳定性分析

Table 3.1 provides a summary of the parameter variations. The work by Malik et al[8] led to the choice of parameter values for Case 1. Figure 3.2 shows the streamwise evolution of disturbance energy for Case 1. More than 600 solution points are employed in the streamwise direction and there are approximately 14 points per streamwise wavelength. It has been shown that with only 3 points per streamwise wavelength, PSE can provide satisfactory results[?]. For the resolution in the wall-normal direction, Li et al[20] stated that 281 points were more than sufficient and 301 points are employed in the present

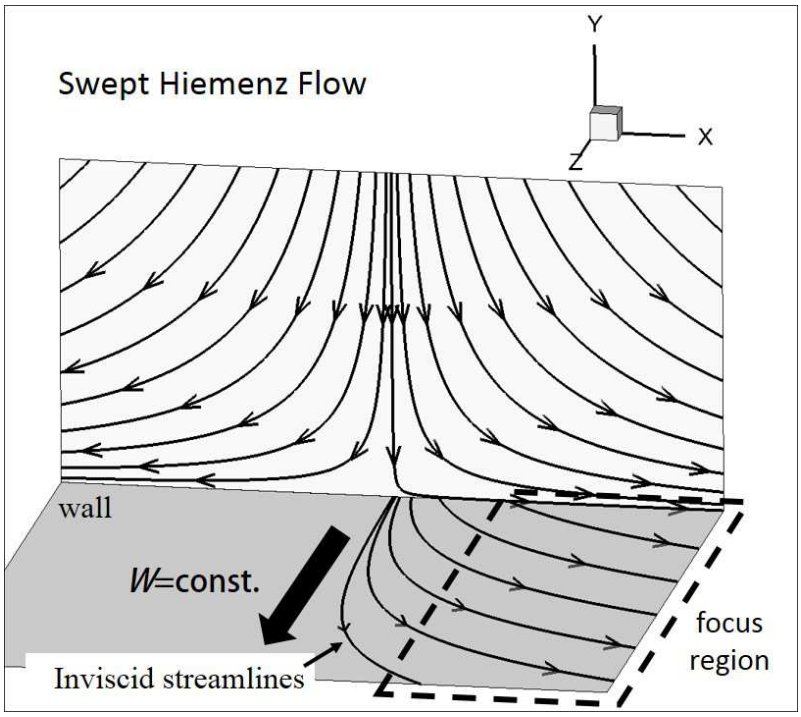

图 3.1　Swept Hiemenz flow

表 3.1　Parameters of test cases

	$c(\mathrm{s}^{-1})$	$l^{\dagger}=(\nu/c)^{\frac{1}{2}}(\mathrm{mm})$	$W_{\infty}(\mathrm{m/s})$	$Re_W=W_{\infty}l^{\dagger}/\nu$
Case1	40	0.6014	12	500
Case2	40	0.6014	24	1000

computation. The good agreement between the present results and Malik's[8] demonstrates the present code is reliable. In fact, this code had been successfully employed in the study of swept wing flows[21,22] and Görtler instabilities[23–27]. In NPSE computations, the data of body-force distribution are obtained from the experiment[28] with actuator operating voltages of 8, 9 and 10 kV. In the experiment, plasma actuators were used to generate near wall jets in the quiescent air and the corresponding jet velocities were 1.7, 2.8 and 3.8 m/s for the voltage 8 , 9 and 10 kV, respectively. However, for Case 1, transition delay can be achieved only with an operating voltage of 8 kV; higher voltages generate stronger disturbances that promote transition. Therefore, the crossflow velocity is doubled in Case 2 to investigate the operating voltage effect and the corresponding results will be shown in Section **??**.

The investigation of the actuators' location effect is mainly based on Case 1. Hence, some stability features are briefly introduced first. The linear local stability results are shown in Figure 3.3. The growth rate of primary crossflow modes with spanwise wave

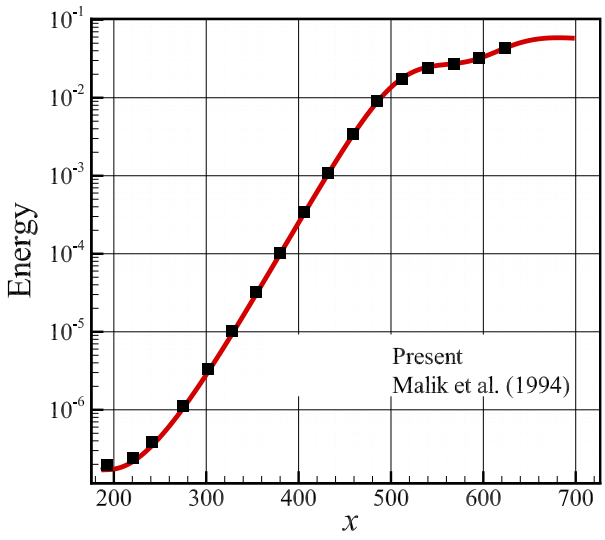

图 3.2　Comparison with the result in Ref.[8] ($Re_W = 500$)

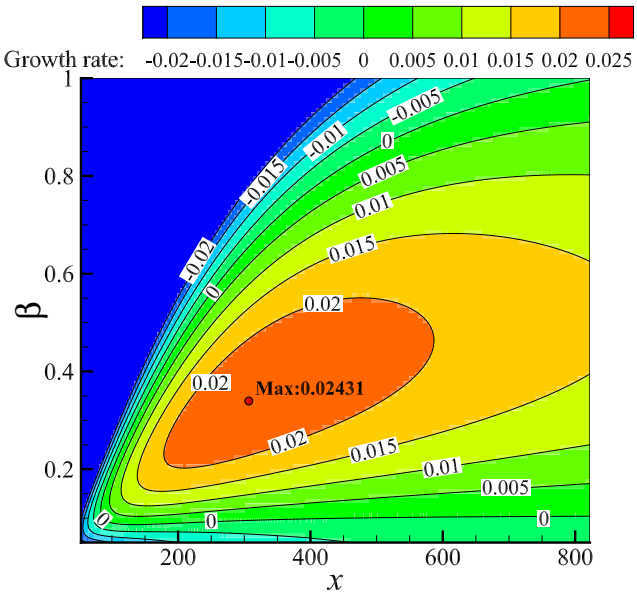

图 3.3　Spatial growth rate of stationary crossflow modes

number $\beta \in [0.1, 1]$ and circular frequency $\omega = 0$ is calculated. Here, the growth rate is defined as the negative imaginary part of complex streamwise wavenumber, namely $-\alpha_i$. The first unstable mode appears at $x = 83$, with β of 0.12; the maximum mode growth rate is 0.02431, with β of 0.33 at $x = 305$. The upper branch of the neutral point moves downstream as β increases. The lower branch of the neutral curve is nearly parallel to the x axis, and β is smaller than 0.085 for stable modes. Specifically, the growth rates of modes with $0.1 < \beta < 0.5$ are maintained at a high level.

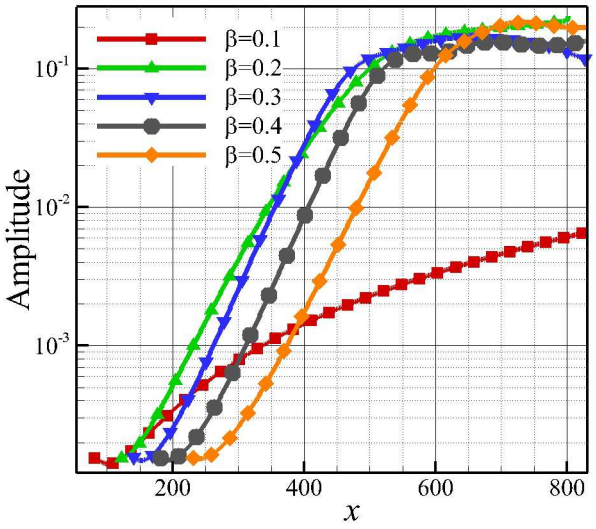

图 3.4　Evolution of primary crossflow modes' amplitude with different fundamental spanwise wave length

NPSE calculations are further conducted to determine the target mode, which probably dominates the transition. Since which mode will dominate highly depends on the environment, here we only consider one possible situation. The simulated spanwise wave numbers are 0.1, 0.2, 0.3, 0.4 and 0.5, with corresponding modes named Mode 1 to 5. Each of these modes are seeded as the primary mode at their own neutral point, which are located at $x = 86, 101, 134, 173$ and 218 for Mode 1 to 5, respectively. Their harmonics are excited by the nonlinearity. The amplitudes, defined as the maximum streamwise disturbance velocity, of these primary modes are compared in Figure 3.4 and the initial amplitudes of these modes are identical. Mode 1 first becomes unstable, but its amplitude increases slowly compared to the others. Mode 3 with β of 0.3 is the first to achieve saturation at $x = 470$ and it is chosen as the target mode. All the following sensitivity analyses aim at this mode and the control method is also designed to damp this mode.

3.2　后掠Hiemenz流动的敏感性分析

The sensitivity of the target mode to the body force is investigated to determine the optimal installation angle and location of the plasma actuators. Based on Eq.(2-56) (2-50), all sensitivity functions are dependent on the output of kinetic energy. Since the sensitivity analyses are based on the linear PSE, our study focuses on the linear stage of disturbance growth. Figure 3.5 shows the contours of streamwise velocity and isolines

of three sensitivity functions at the cross-section $x = 280$. The output location is set at $x = 500$. The solid lines indicate the positive values, while the dashed lines indicate the negative values. No rollover occurs in the contour of streamwise velocity; the low-momentum and high-momentum streaks are located side by side near the wall, and the crossflow vortices are forming. Note that similar patterns of the sensitivity function distributions can be found at other cross-sections; whether the sensitivity functions are positive or negative is of the most interest.

As shown in Figure 3.5(a), the positive values of G_u are distributed beneath the high momentum streaks and overlapping with the low momentum streaks. Otherwise values are negative. Figure 3.5(b) shows that the positive sensitivity function G_v is concentrated on the low momentum streak and vice versa. That means if we want to use wall-normal forcing, like blowing or suction, the suction should be under the low momentum streaks and the blowing need to be under the high momentum streaks. The neutral lines of G_v, where $G_v = 0$, are not as twisted as that of G_u and G_w and they are more vertical. The distribution of G_w is similar with that of G_u, only switched the positive and the negative. Let's remind the control method proposed by Dörr and Kloker[29]. They have two basic control setups called case ACF and CCF shown in Fig 4 in their paper. In the case ACF, the body force with positive spanwise component is imposed under the crossflow vortex where nearly the low momentum streaks locates and the G_w are all negative. In their case CCF, the force with opposite direction is introduced at the secondary vortex where the high momentum streaks locates and G_w is positive. According to Eq.(2-55), a negative product of forcing and the sensitivity function yields a dampening of the disturbance kinetic energy, which implies the correctness of the present sensitivity analyses.

Then, different output locations are considered at $x = 450, 400, 300$. Figure 3.6 shows the contours of streamwise velocity and isolines of three sensitivity functions at the cross-section $x = 280$ and with the output location at $x = 300$. Compared to the case at $x = 500$ (see figure 3.5), the most sensitive region with respect to streamwise and spanwise force components moves downward to the wall. However, similar patterns to figure 3.5 are found at $x = 350, 400$ and 450 (not shown). From this result, we can conclude that in terms of the vicinity influence, force near the wall works better than that away from the wall. Since we are concerned with the evolution of disturbance kinetic energy away from the actuator location, which means sensitivity functions away from the output location, all results shown hereafter are from the case output location at $x = 500$.

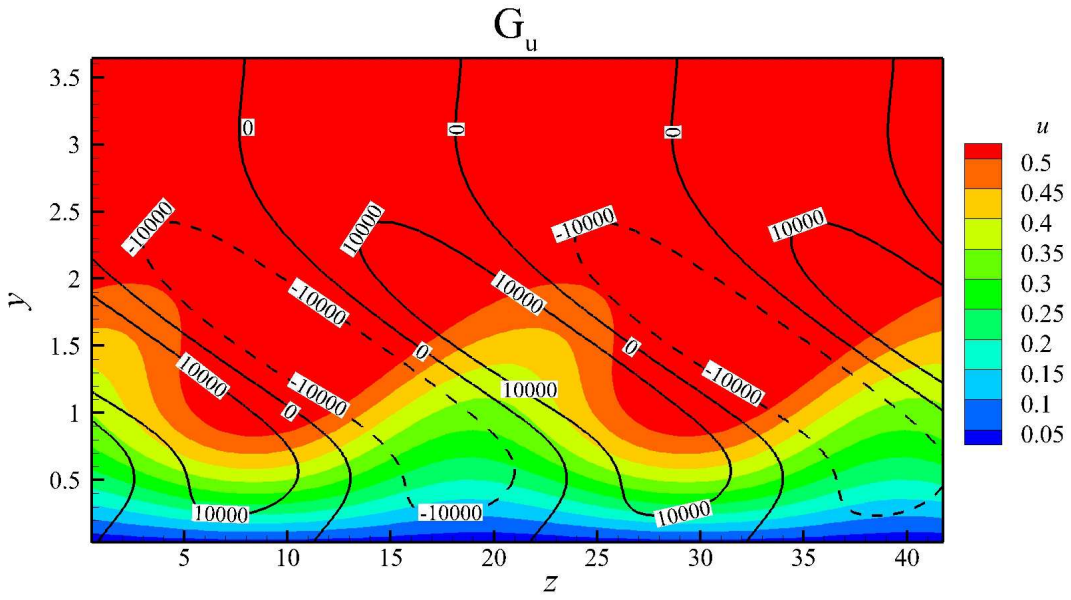
G_u
y
z
u
0.5
0.45
0.4
0.35
0.3
0.25
0.2
0.15
0.1
0.05

(a)

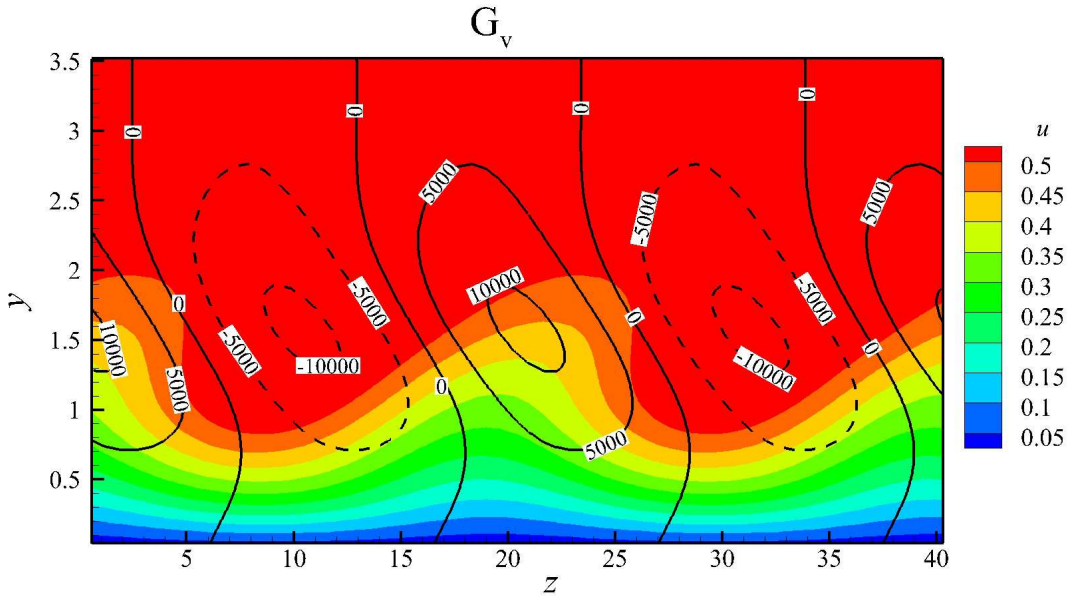
G_v
y
z
u
0.5
0.45
0.4
0.35
0.3
0.25
0.2
0.15
0.1
0.05

(b)

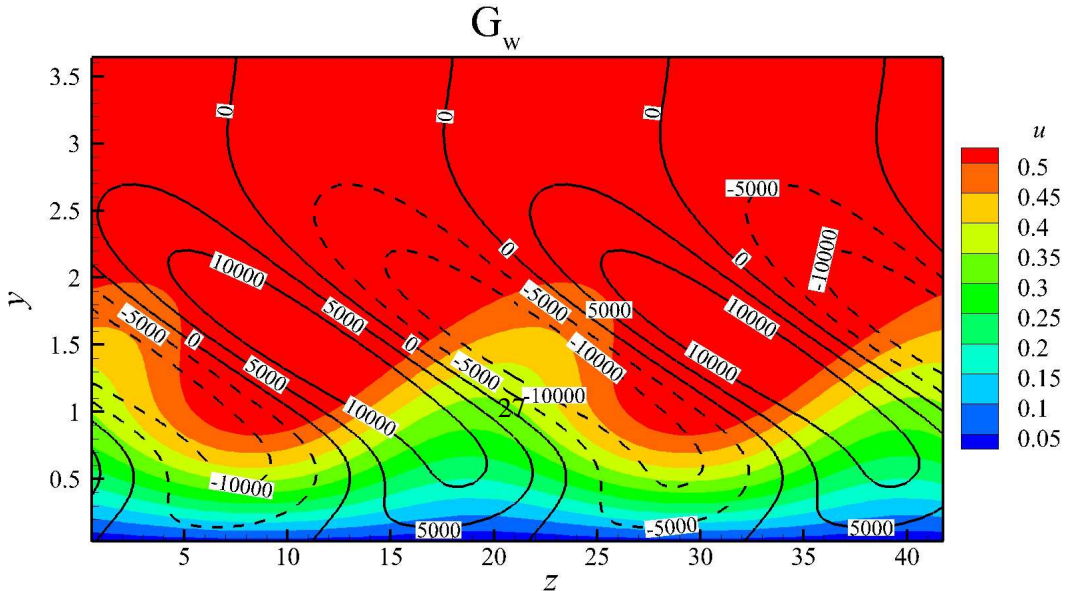
G_w
y
z
u
0.5
0.45
0.4
0.35
0.3
0.25
0.2
0.15
0.1
0.05

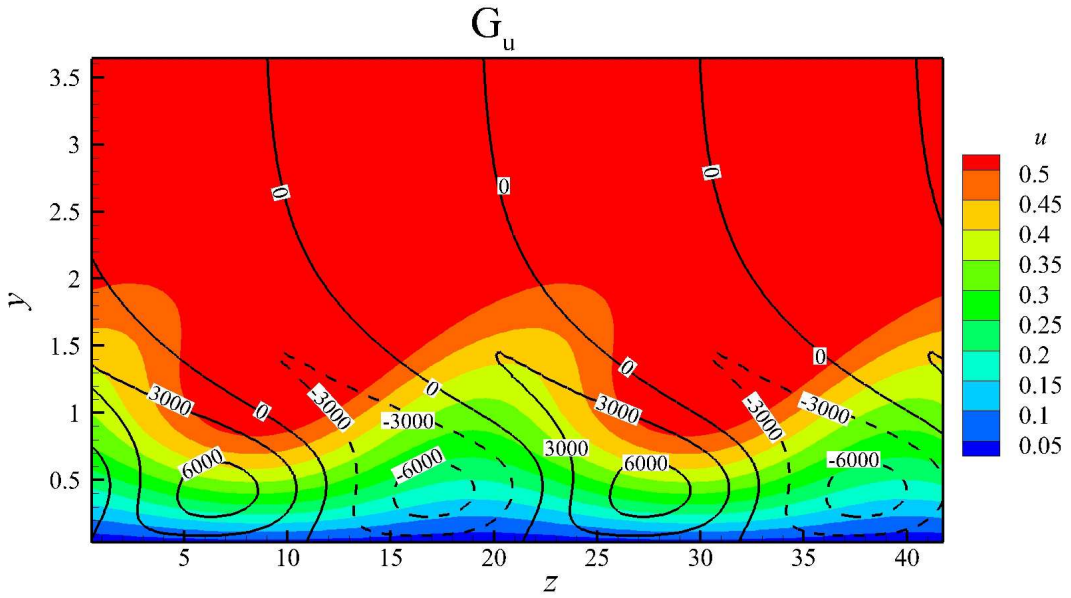
G_u
y
z
u
0.5
0.45
0.4
0.35
0.3
0.25
0.2
0.15
0.1
0.05

(a)

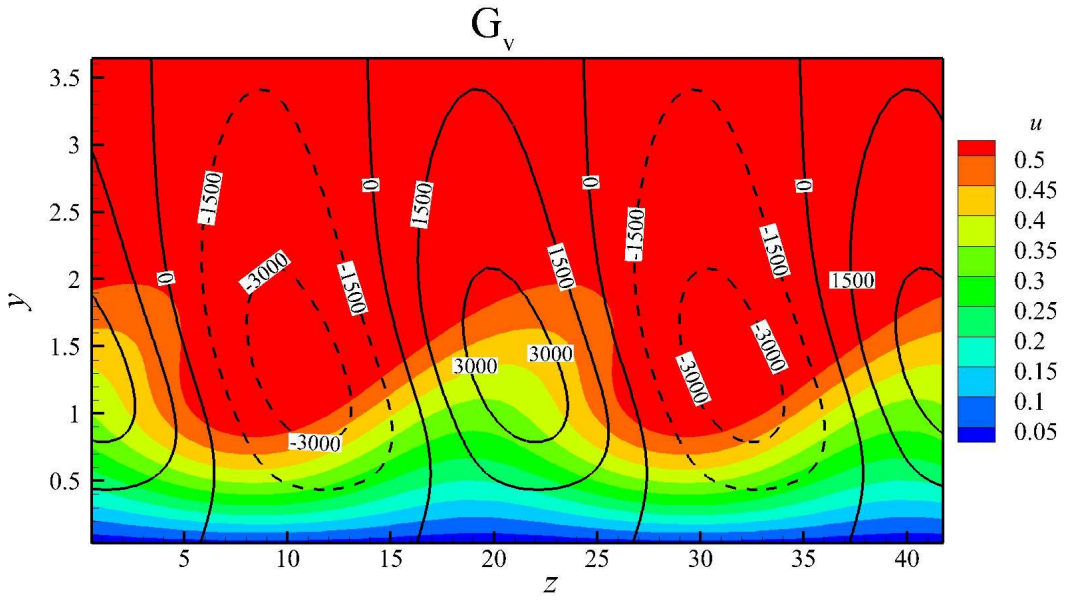
G_v
y
z
u
0.5
0.45
0.4
0.35
0.3
0.25
0.2
0.15
0.1
0.05

(b)

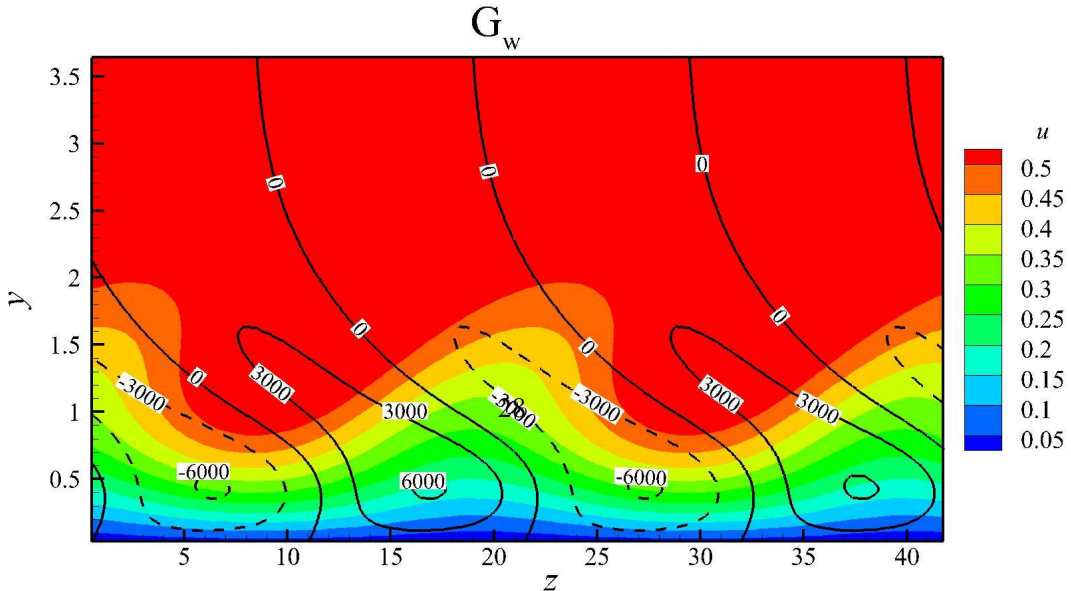
G_w
y
z
u
0.5
0.45
0.4
0.35
0.3
0.25
0.2
0.15
0.1
0.05

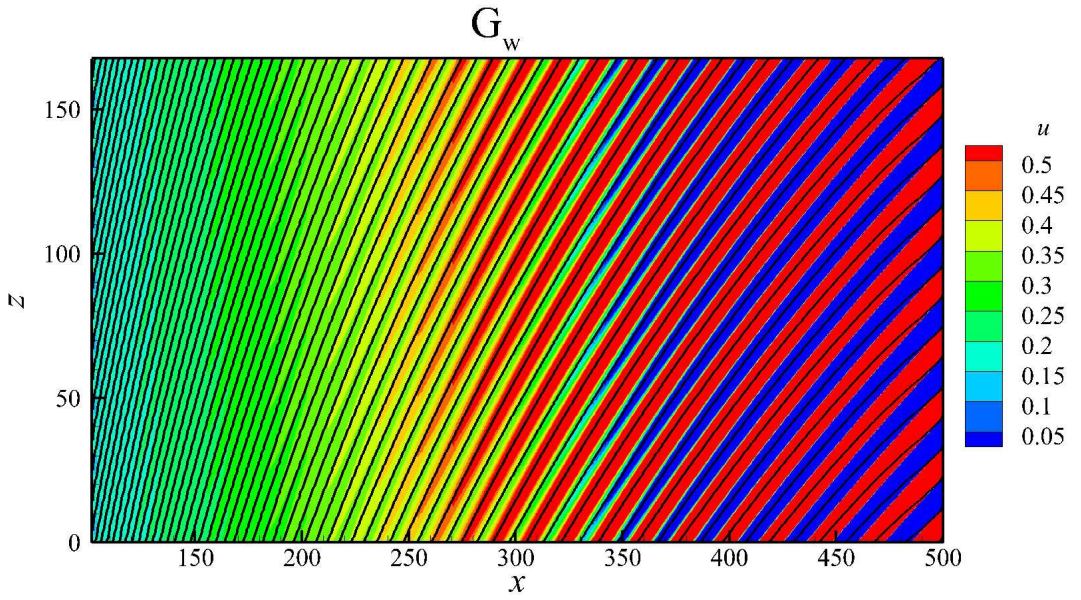

图 3.7　Distribution of sensitivity functions G_w at $y = 1$

Figure 3.7 plots the iso-lines of the sensitivity function, G_w, and the contours of the streamwise velocity component in a $z - x$ plane near the wall. From this figure, the streaks can be seen clearly. The red color indicates the high-momentum streak, and the blue indicates the low-momentum streak. Away from the output location, the G_w isolines are parallel to the streak direction. Therefore, the best choice is to set the actuated body-force direction parallel to the streak direction, the crossflow vortex axis, which ensures that the actuation affects the most sensitive region at each streamwise location. Dörr and Klocker[29,30] always put their control devices in this manner.

The maximum value of sensitivity functions over spanwise direction is shown in Y-X plane in Figure 3.8. Since we use the same contour level in all the three pictures, it is evident that the flow is more sensitive to streamwise forcing than that in other two directions. The most sensitive region is located inside the boundary layer but away from the wall. That is because too close to the wall viscous effect and no-slip boundary condition dominate and thus the body force effect declines.

Figure 3.9 shows the streamwise distributions of the maximum value of the sensitivity functions on each cross-section. As mentioned before, the neutral point is located at $x = 134$ and it is indicated with a vertical dash line in the figure. The maximum values appear immediately upstream of the neutral point consistent with the findings by Pralits[17] for a flat-plate case. Downstream of the neutral point, all sensitive functions decrease rapidly with increasing x. This indicates that the actuator is more effective when placed

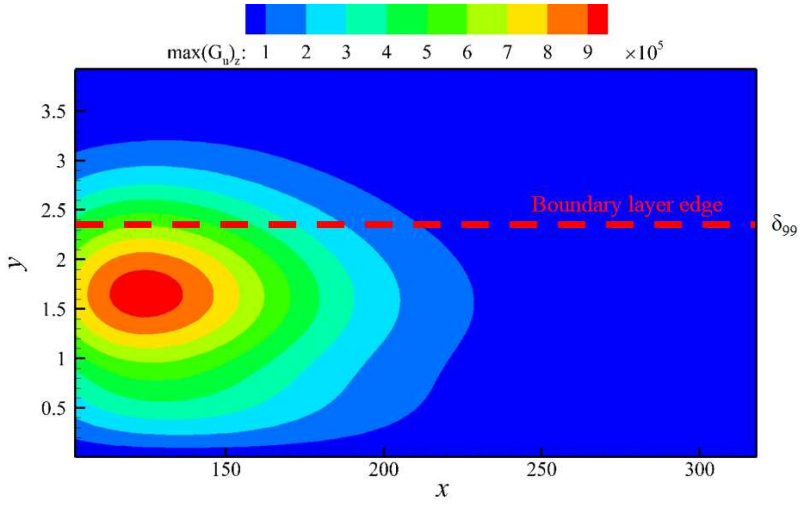

(a)

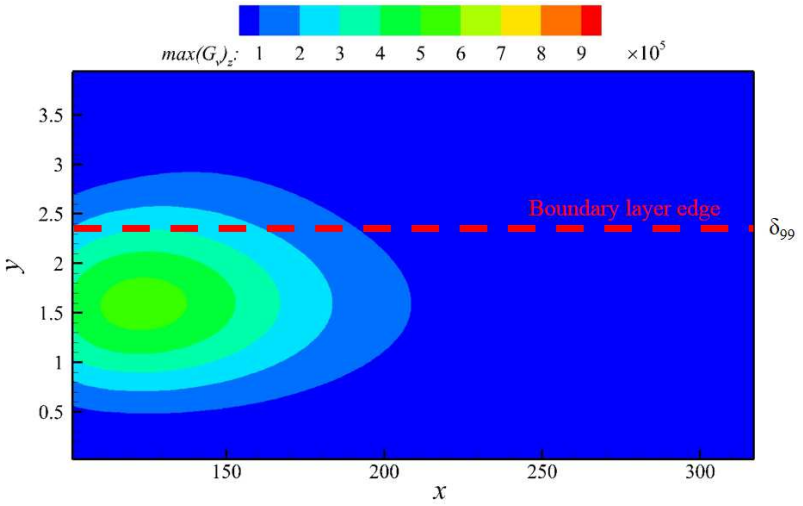

(b)

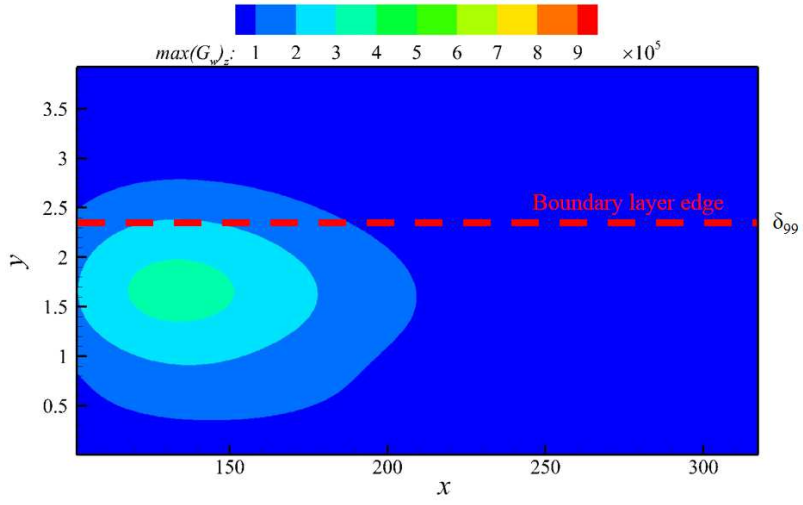

(c)

图 3.8　Contours of maximum (a) G_u, (b) G_v and (c) G_w along the Z direction with the output location at x=500.

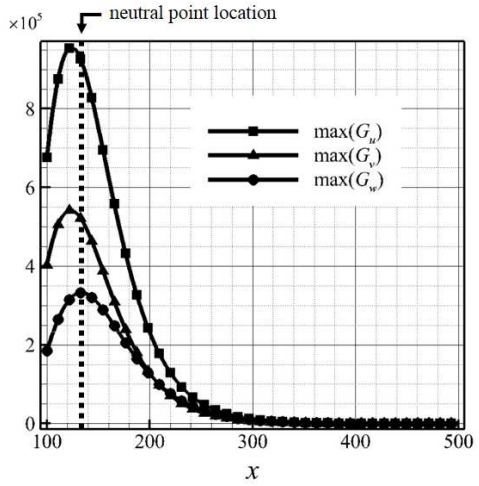

图 3.9　Streamwise distributions of the maximum value of the sensitivity functions on the y-z plane

further upstream until the neutral point. However, if the actuator is sufficiently close to the neutral point, it is likely to act as a strong disturbance that over-rides the natural disturbance and dominates transition. Nevertheless, from these sensitivity analyses, we have learnt about the features of this flow from one perspective and determined that the upstream control could be more efficient in the interval in which the natural disturbance have fully developed.

3.3　采用等离子体激发器推迟后掠Hiemenz流动转捩

However, the sensitivity analyses are based on a linear assumption, and NPSE computations are required to further investigate the actuator location effect. Here, the data for the body force distribution obtained from the experiment[28] with an actuator operating voltage of 8 kV are used. Figure 3.10 compares the streamwise mode-energy evolution with the actuator imposed at different spanwise locations. Here, the mode-energy is defined as following:

$$\text{Energy} = \frac{1}{2}\int_0^\infty (|\hat{u}|^2 + |\hat{v}|^2 + |\hat{w}|^2)dy \tag{3-2}$$

Since the mean flow correction mode, (0,0) mode, does not have a complex conjugate, its energy is defined as following:

$$\text{Energy}_{00} = \frac{1}{4}\int_0^\infty (|\hat{u}|^2 + |\hat{v}|^2 + |\hat{w}|^2)dy \tag{3-3}$$

Figure 3.11 depicts the actuator locations relative to the local crossflow vortex. The spanwise locations simulated are at $z/T_z = 0.5, 0.6, 0.7, 0.8, 0.9$ and 1.0, with the corresponding Cases (a) to (f). Here, T_z is the wavelength of the primary mode. In Figure 3.10, the extent of the actuation region is shown within 2 blue dots; (0,0) mode represents the meanflow correction mode, (0,1) mode the primary mode, and (0,2) mode the mode with double the spanwise wave number of the primary mode. All the first number 0 indicates the frequency is zero and they are all steady modes. The characteristic of the primary mode is consistent with that of the target mode in sensitivity analyses: In Cases (d) and (e), the primary-mode energy decreases considerably with the actuator imposed at the bottom of the crossflow vortex, the negative G_w region. The minimum values of the primary modes' energy are 0.0067 and 0.0077 for Cases (d) and (e), respectively. However, in Cases (a) to (d), the (0,2) mode is promoted, as also observed by Dörr and Kloker in their DNS study[29] (Fig 8 in their paper). The (0,2) mode's energy even exceeds that of the primary mode (see Figure 3.10(d)). Fortunately, in the actuation region all-mode energy decreases in Cases (e) and (f). Therefore, the optimal spanwise actuator location is $z/Tz = 0.9$. Note that results with only two spanwise locations are shown in Dörr and Kloker's DNS[29], and in both of them the (0,2) modes were promoted.

The optimal spanwise location of the plasma actuators is used to investigate their streamwise location effect on transition using NPSE. In sensitivity analyses, a plasma actuator location upstream as possible without contaminating the quiet boundary layer is suggested. Figure 3.12 compares the streamwise mode-energy evolution within different streamwise actuation regions. The actuation regions have the same extent (shown between the two large dots) but different start points, x_{start}, at $x = 315, 358$ and 400. Here, the body force's strength is reduced to one tenth of the original, because too strong force at upstream will contaminate the boundary layer. A much lower mode energy is obtained for the case with $x_{start} = 358$ compared to the one with $x_{start} = 400$ because x_{start} of the former case is closer to the neutral point at $x = 134$, as pointed out in the sensitivity analyses. Figure 3.13 further depicts the reduction of the maximum streamwise velocity of the primary mode downstream of x_{start}. The largest reduction is given for the case with $x_{start} = 315$ in the vicinity of x_{start}, where the actuated body-force integration is small and therefore the sensitivity analyses based on the linear assumption are still acceptable. However, downstream of $x_{start} + 18.7$, the primary mode suppression becomes weaker and weaker for the case with $x_{start} = 315$ because here disturbances are introduced so far

upstream that they contaminate the essentially quiet boundary layer. This explains why the case with $x_{start} = 358$ provides the most effective flow-transition delay control, as shown in Figure 3.12.

Figure **??** gives the LST results of the growth rate of steady crossflow modes for Case 2, where the crossflow velocity is doubled to investigate the operating voltage effect. The first unstable mode appears at $x = 85$, with β of 0.05; the maximum mode growth rate is 0.0336 with β of 0.26 at $x = 451$. The neutral-curve slope of the upper branch is smaller than that for Case 1. Figure **??** further shows the evolution of the mode energy obtained using NPSE. The simulated wave numbers are 0.1, 0.2, 0.3 and 0.4. The mode with β of 0.1 becomes the most unstable upstream but increases slowly compared to the others. Due to its relatively early start and large increase rate, the mode with β of 0.2 is chosen as the target mode in the following study.

The results of the sensitivity analyses (not shown) are similar to those for Case 1. The higher freestream spanwise velocity in Case 2 allows us to adopt higher operating voltages of 9kV and 10kV. Figure 3.15 compares the streamwise mode-energy evolution with different operating actuator voltages. The actuation region ranges from 500 to 550 in the x direction with the optimum spanwise location for each case. The simulated operating voltages are 8 kV, 9 kV and 10 kV, with corresponding maximum jet velocity magnitudes of 1.7 m/s, 2.8 m/s and 3.8 m/s, respectively. Note that only 8,9,10,11,12 kV voltages were provided in the measurement[28] and the last two were too strong for our case. An increase in operating voltage leads to more efficient disturbance suppression upstream for $x = 530$. However, for the case with a 10 kV operating voltage, the disturbance energy starts to increase downstream for $x = 530$, and the energy of the mean flow distortion mode (0, 0) as well as the harmonic mode (0, 2) even exceeds the energy of the primary mode (0, 1). Eventually the harmonic mode (0, 2) dominates the flow. Forcing that is too strong may cause the formation of nocent vortices that promote transition to turbulence, as also reported by the DNS study[29]. Therefore, it can be concluded that for Case 2, the moderate operating voltage of 9 kV provides the most effective flow-transition delay control.

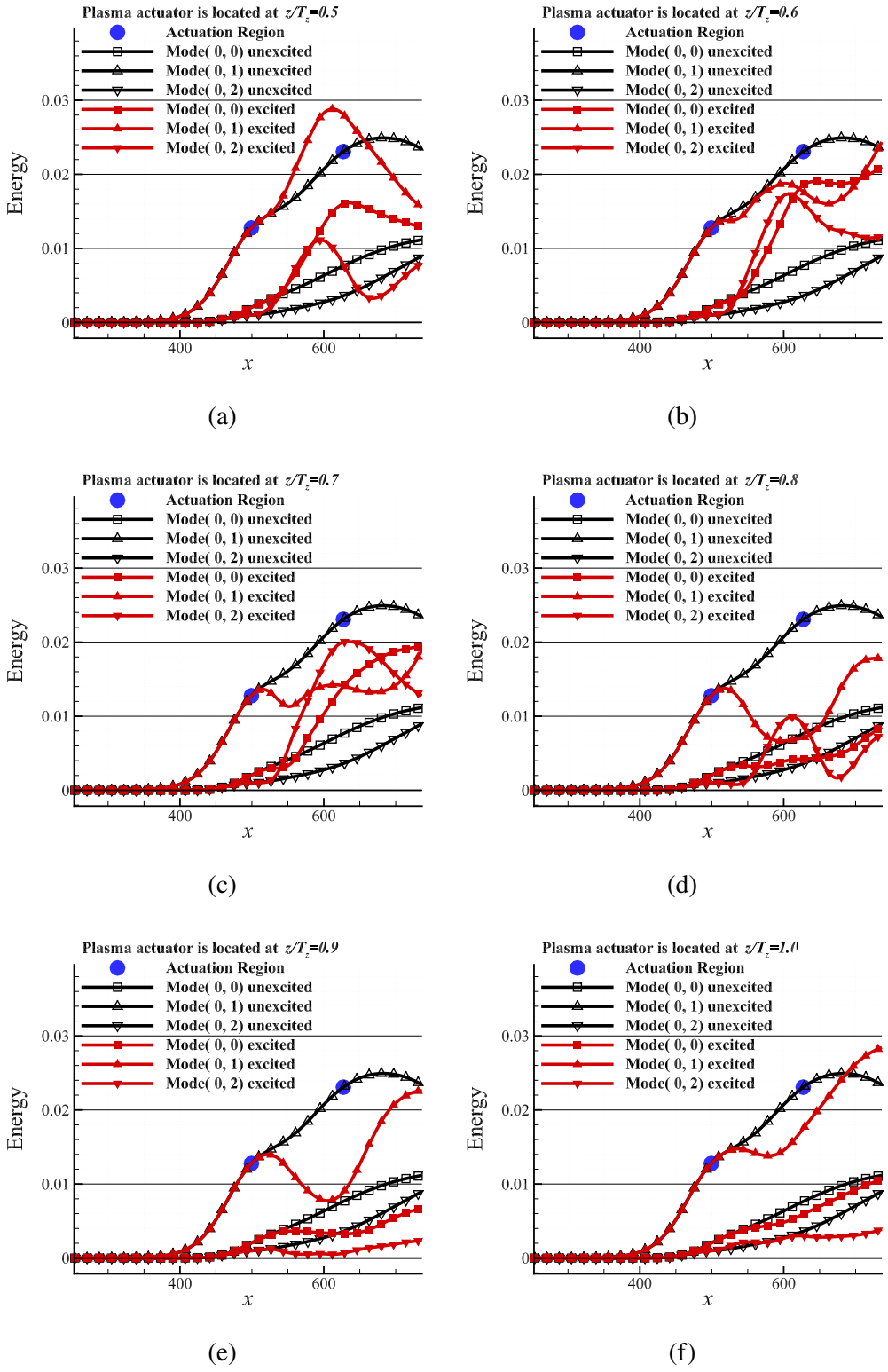

图 3.10　Comparison of the streamwise mode-energy evolution with the actuator imposed at different spanwise locations: (a) $z/T_z = 0.5$, (b) $z/T_z = 0.6$, (c) $z/T_z = 0.7$, (d) $z/T_z = 0.8$, (e) $z/T_z = 0.9$, (f) $z/T_z = 1.0$.

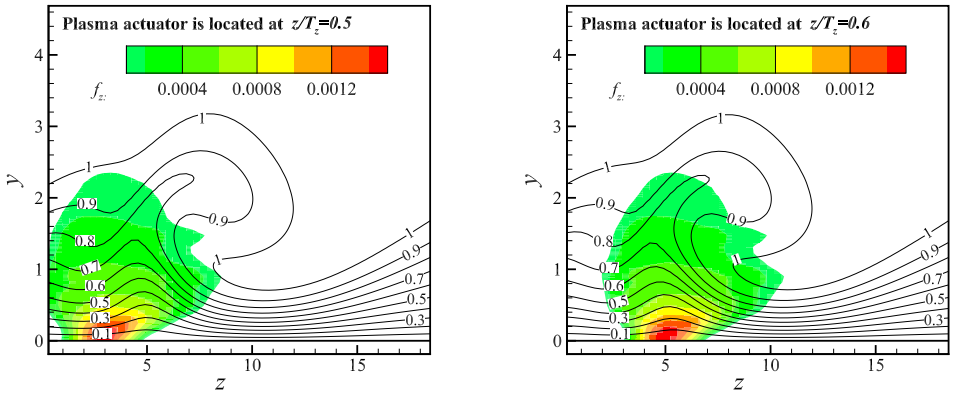

(a)　(b)

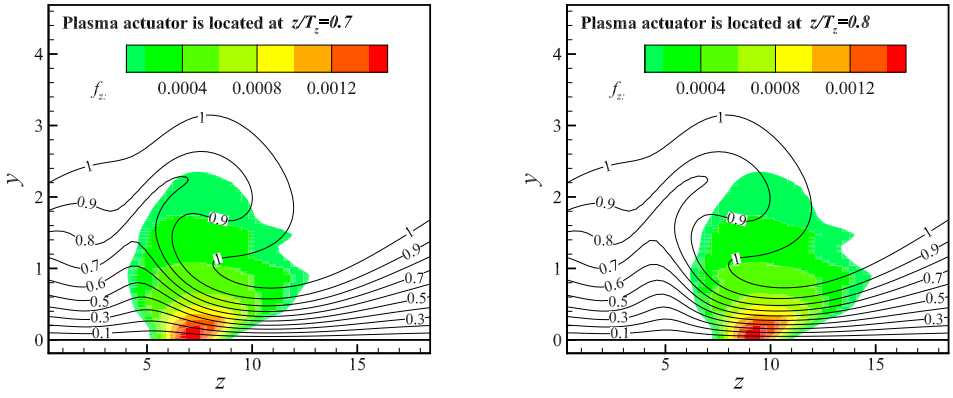

(c)　(d)

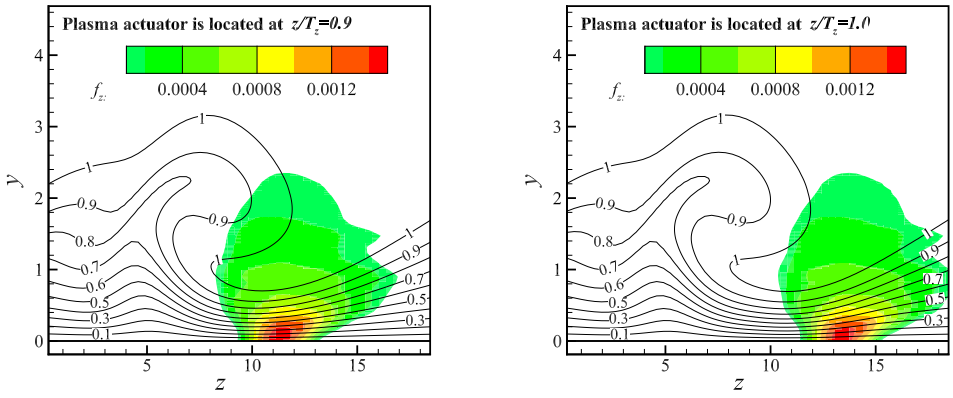

(e)　(f)

图 3.11　Comparison of the streamwise mode-energy evolution with the actuator imposed at different spanwise locations: (a) $z/T_z = 0.5$, (b) $z/T_z = 0.6$, (c) $z/T_z = 0.7$, (d) $z/T_z = 0.8$, (e) $z/T_z = 0.9$, (f) $z/T_z = 1.0$.

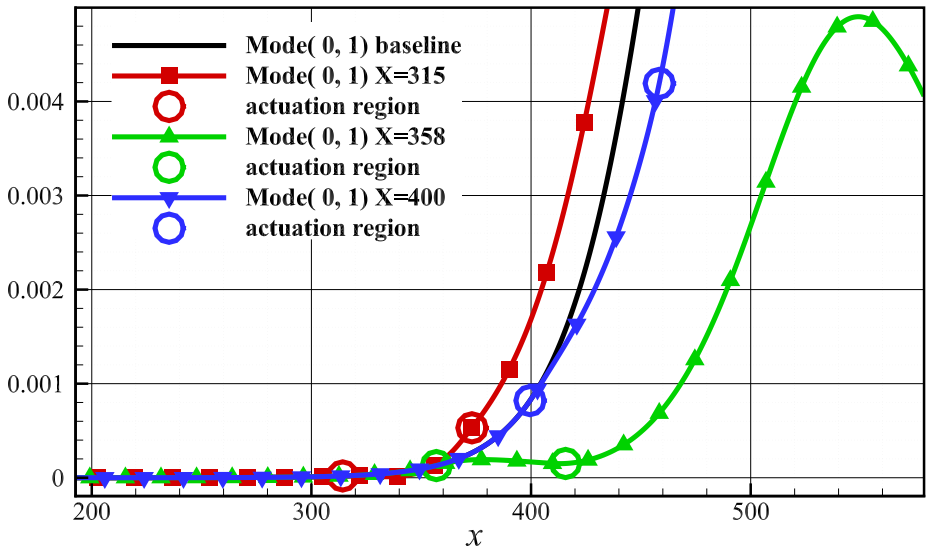

图 3.12　Comparison of control cases with actuators put on different streamwise location

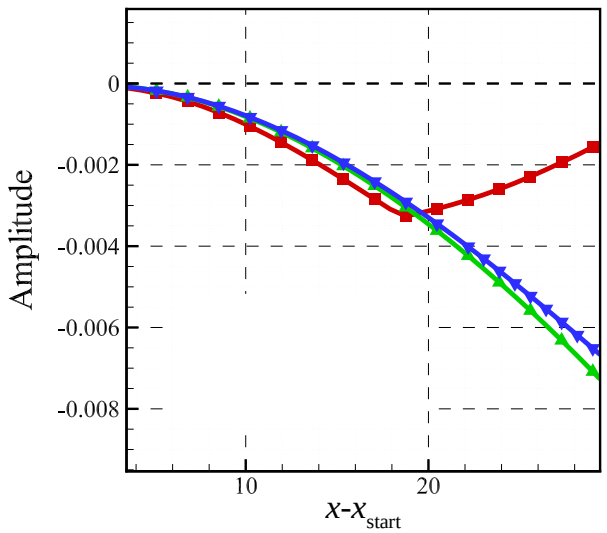

图 3.13　Differences of maximum streamwise velocity of primary mode between uncontrolled and controlled cases in the control regions (x_{start}: start point of control region)

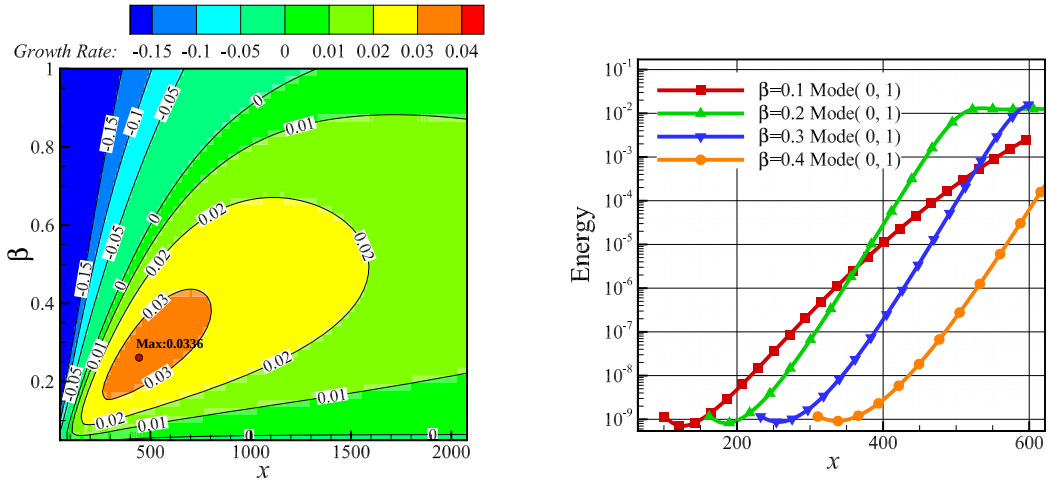

图 3.14　Growth rate of steady crossflow modes (a) and evolution of mode energy (b) computed using LST and NPSE, respectively.

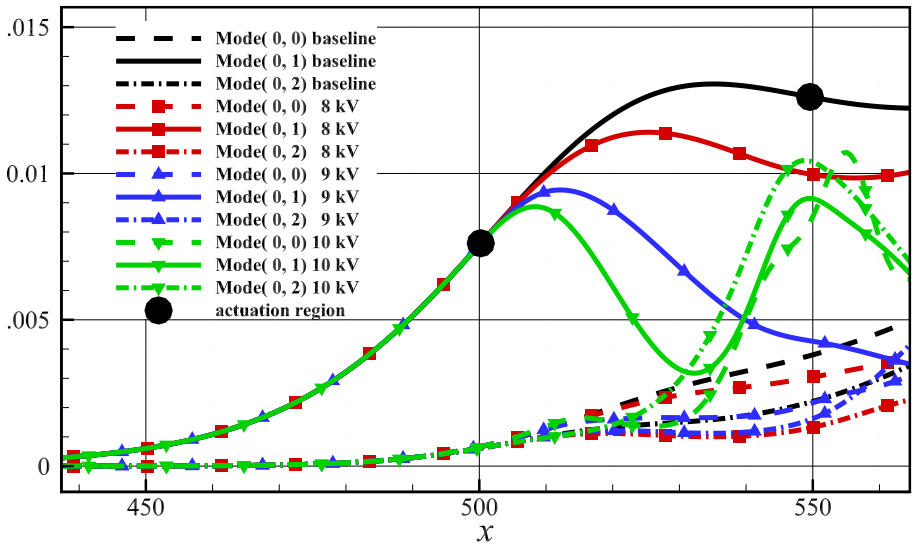

图 3.15　Evolution of modes energy controlled by plasma actuator with different operating voltage

第4章　后掠翼上流动失稳分析与控制

4.1　后掠翼上流动的稳定性分析

数值研究了后掠Hiemenz流动转捩控制之后，本文将研究目标转移到更贴近实际的工况，研究一个真实的后掠翼流动的转捩控制。清华大学（Tsinghua University）在2018年进行了NLF-0415后掠翼上翼面的转捩实验研究工作[?]，本文以该实验的工况作为基准，研究等离子体在实际的后掠翼流动中控制转捩的效果。这一实验在后文中将会被简记为“THU实验”或“THU experiment”。这里先简述一下实验的设备和工况。该实验是在清华大学自己的低湍流度风洞中进行的，风洞试验段大小为1.2m×1.2m×3m。风洞内安装NLF-0412翼型，如图4.1所示。在实验中采用的直角坐标系为($X_{\mathrm{wt}}, Y_{\mathrm{wt}}, Z_{\mathrm{wt}}$)，其$X_{\mathrm{wt}}$方向与风洞的流向平行。在计算中本文用的到直角坐标系为x, y, z（如图4.1）。计算所用坐标系的z方向与翼型前缘线平行，这样在采用了无限展长假设之后，这一方向的物理量就是均匀的。该风洞运行时测试段的风速可以为5.0到90.0m/s，湍流度可以低到0.05%。此次试验采用的翼型的弦长c=1.2m，有45°后掠和-4°攻角。该翼型在上翼面有很强的顺压梯度，可以有效的抑制T-S波失稳[?]。翼型中间到风洞入口大约1.25m。

The free stream was surveyed by a single hot wire. The free stream is uniform and with low turbulence intensity of 0.08~0.1%. The streamwise velocity profile of the boundary layer on the laminar region along with the middle span, namely X/C = 0.2, 0.4 and 0.6, respectively, was measured using a boundary layer hot wire sensor (TSI Model 1261A). The hot wire sensor was driven by a computer controlled three-dimensional moving mechanism. The minimum movement can be controlled within 10μm. Along the normal direction at each location, U_{wt}, the velocity component in X_{wt} direction, was measured at every 0.05mm till the double thickness of the boundary layer. To protect the hot wire sensor from physical damage and make sure the wall-heat-effect be as small as possible, the first measure-point is fixed at 0.15mm from the airfoil surface. The distance is observed by a microscopic camera mounted over the transparent wall of the wind tunnel. The hot wire signal was amplified, filtered by a constant temperature anemometer (CTA, TSI IFA-300), acquired by a 12-bit UEI A/D board, and then recorded by a computer. The sampling frequency was fixed at 20kHz, and the duration was taken as 10s.

实验中采用了单一的热线测量了来流的情况。来流风速均匀，湍流度0.08~0.1%。采用边界层热线(TSI Model 1261A)测量翼型X/C = 0.2，0.4，0.6位

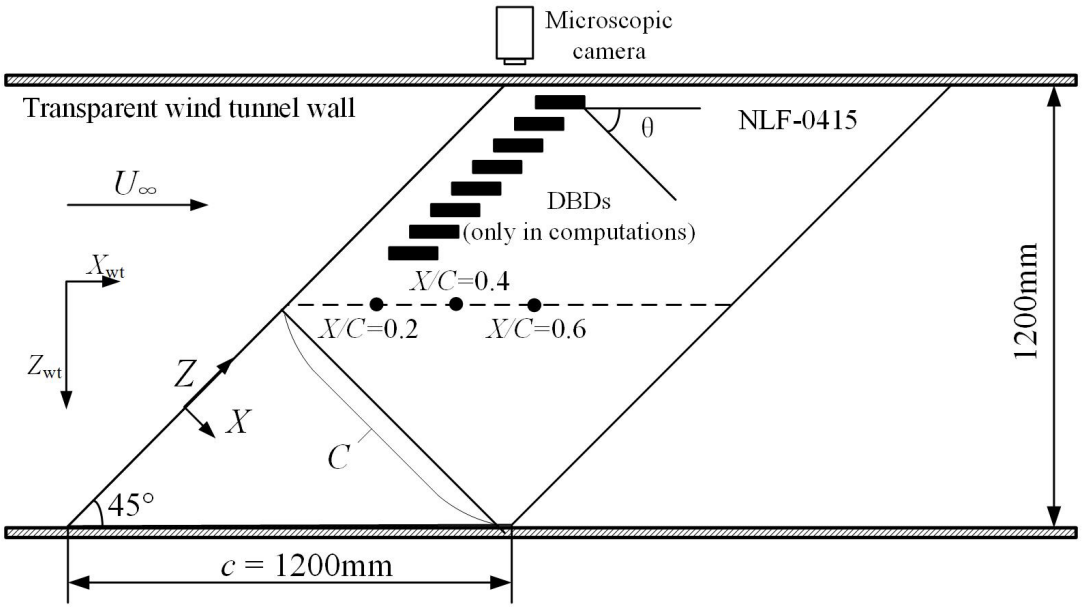

图 4.1　Hot wire measurements in the wind tunnel. Symbol " • " represents the location of the hotwire measurement.

置处的边界层速度剖面。

To verify the baseflow calculation, the experimental Reynolds number Re is 1.81×10^6 corresponding to the free-stream velocity U_∞=22.3m/s ($Re = U_\infty c/\nu$ where U_∞ is the free stream velocity, c is the chord length and ν is the kinematic viscosity coefficient of the air). The flow in this case is laminar overall 70% of the chord length. For plasma control cases in computation, U_∞ is doubled to give higher Reynolds number.

Code with a high-precision Correction Procedure via Reconstruction (CPR)[31? ?] scheme was employed to resolve the inviscid flow field. The computed inviscid stream velocities on the wall and the experimentally measured velocities at the edge of the boundary layer are compared in figure 4.2. The black line was obtained from the computations, and the three dots show the experimental data. The agreement between the computation and the experiment is good. The computed flow quantities over the upper surface of the wing were therefore adopted as the boundary conditions for the boundary layer equation, and the calculated velocity profiles at 20% and 40% chord length, where the flow is still laminar are compared with experimental results in figure 4.3. Again, the lines are from the computation and the dots from the experiment. Their excellent agreement demonstrates that the present baseflow profile and the computational code is reliable.

In this subsection, the stability characteristic of the baseline case, in which DBD actuators are not added, is investigated at first.[32] also studied the stability features of

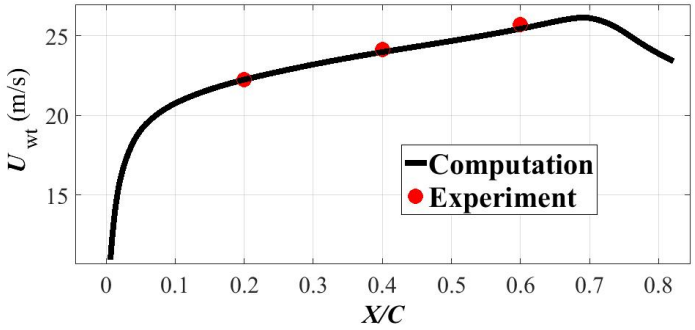

图 4.2　Comparison of computed and experimental U_{wt} at the edge of the boundary layer.

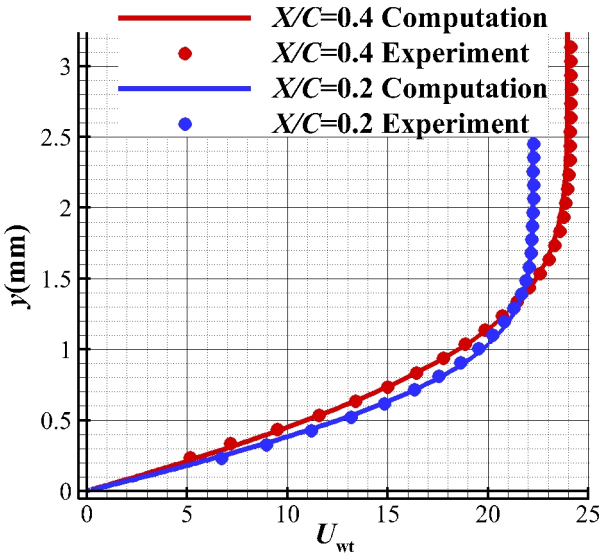

图 4.3　Comparison of computed and experimental U_{wt} profiles at X/C = 20% and 40%.

this airfoil with the same angle of sweep and the same angle of attack. Their experiment will be referred to as "Reibert's experiment" in the following. However, the sizes of the wind tunnels and the wing models are different. In Reibert's experiment, the cord length is 1.83m and the size of their wind tunnel's working section is 1.4m×1.4m×5m. Besides, the distance between the model and the wind tunnel's wall was not reported in their paper. These differences lead to different pressure coefficient distributions, as shown in figure 4.4. The pressure gradient in the THU experiment was stronger than that in Reibert's experiment. In the THU experiment, the flow accelerated more rapidly. To clarity the difference in pressure gradient, four different computational cases are set. Two of them use the pressure coefficient distribution from Reibert's experiment, with free-stream velocities of 22.3 and 44.5 m/s. The others adopt the THU pressure coefficient distribution, again with free-stream velocities of 22.3 and 44.5 m/s. The velocities at the

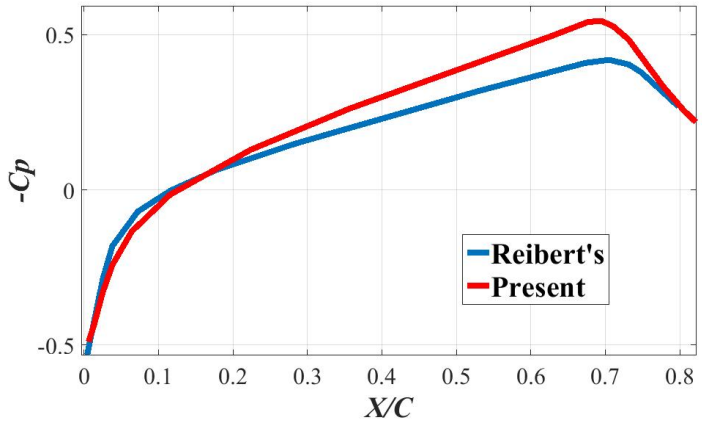

图 4.4　Pressure coefficients from the THU experiment (red) and as given in Reibert's dissertation[32] (blue).

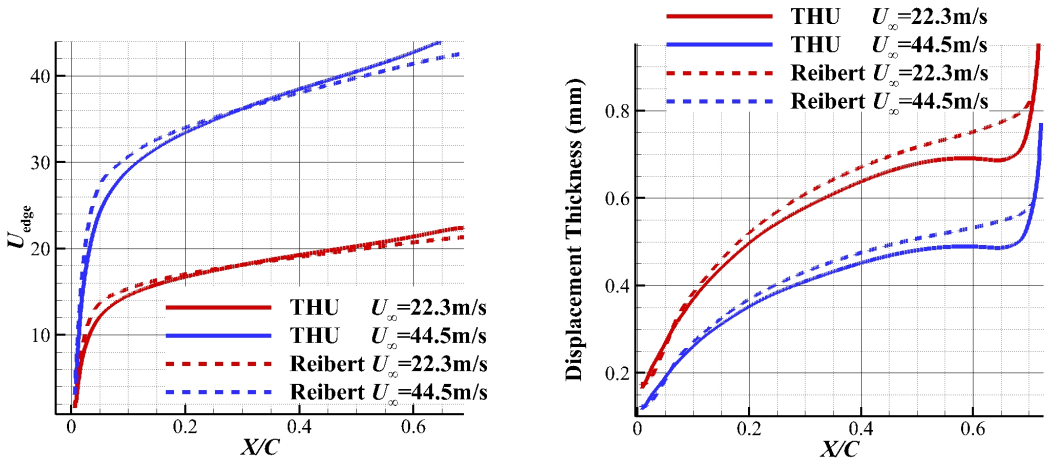

(a)　　(b)

图 4.5　(a) Comparison of streamwise velocity at the edge of the boundary layer in different cases. (b) Comparison of boundary layer displacement thickness in different cases.

edges of the boundary layers and the displacement thicknesses of the boundary layers in these four cases are shown in figure 4.5. It can be seen that with the THU pressure coefficients, the inviscid stream velocity increases slowly near the leading edge. However, it accelerates rapidly in the middle section of the airfoil, and exceeds the velocity in the case with Reibert's pressure coefficient at nearly 30% chord length. The boundary layers in the THU experiment are thicker than those in Reibert's, for both 22.3 and 44.5 m/s free-stream velocities. The pressure reaches its lowest value at nearly 70% chord length. Hence, the boundary layer thickness increases dramatically at that position.

Figure 4.6 plots the crossflow velocity profiles at the position of 20%, 40%, and 60% chord length. The crossflow velocity must vanish outside the boundary layer, with the

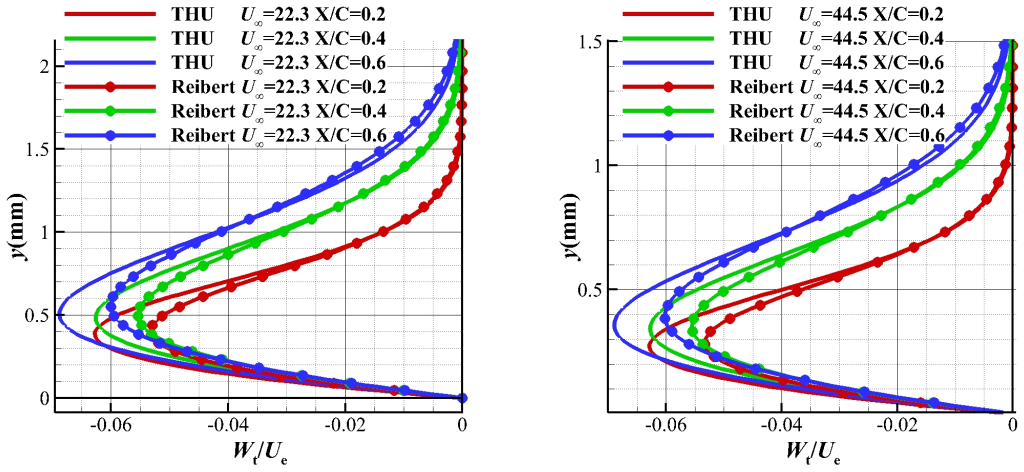

(a) $U_\infty = 22.3m/s$　　(b) $U_\infty = 44.5m/s$

图 4.6　Comparison of crossflow profiles at different streamwise locations.

heights of vanishment increasing from 20% to 60% chord length for all cases, owing to boundary layer growth. At the same free-stream velocities, the peak values of the crossflow velocities with the THU pressure coefficient are higher than those with Reibert's pressure coefficient. This is mainly because at these three streamwise locations, the THU pressure gradients are all stronger than Reibert's. It is well known that crossflow forms owing to an imbalance in the pressure gradient and to circular acceleration in the boundary layer. A stronger pressure gradient leads to a greater imbalance and subsequently to a stronger crossflow. Hence, a difference in pressure gradient leads directly to a difference in crossflow intensity, which is very important for crossflow instability.

The e^N method is employed to investigate the stability features of all four cases, with the results shown in figure 4.7. The N-value is defined as

$$N = \int_{x_0}^{x} (-\alpha_i)\, dx, \tag{4-1}$$

where α_i is the imaginary part of the streamwise wave number, which is computed using the local linear stability equation (in LST). Its negative value $-\alpha_i$ represents the spatial growth rate of the corresponding instability mode. x_0 is the position at which the mode first became unstable. The envelopes of the N-value, that is, the maximum N-values of all the steady modes at each streamwise location, are shown in figure 4.7(a). The blue and red curves stand for the cases with 44.5 and 22.5 m/s free-stream velocities, respectively. Curves with square symbols show the results with the THU pressure coefficient distribution and those with circles the results with Reibert's distribution. It can be seen that the N-

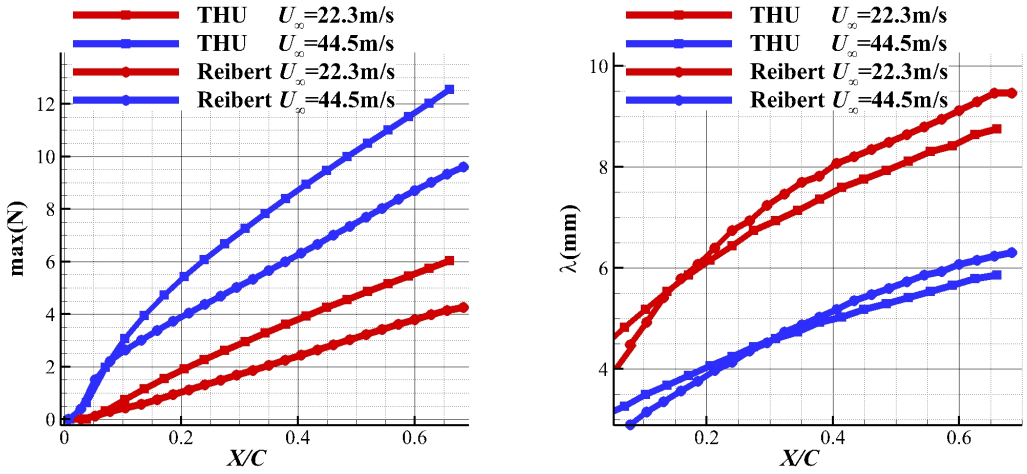

(a)　(b)

图 4.7　Comparison of (a) the maximum N-value and (b) the spanwise wavelength of the corresponding modes at each streamwise location.

values from both cases with 44.5 m/s free-stream velocity are higher than the other two cases, because increasing the free-stream velocity, equivalent to increasing the Reynolds number, makes the flow more unstable. The figure also shows that for the same free-stream velocity, the THU pressure coefficient distribution always makes the flow less stable. Recalling the crossflow comparison in figure 4.6, it can be seen that a small reduction in the crossflow velocity will lead to a big difference in the N-value. Since the mode amplitude is calculated as $A = A_0 e^N$ (where A_0 is the initial amplitude), the effect on the amplitude will be more significant. The spanwise wavelengths of the most unstable modes, that is, the modes that have the biggest N-value at each streamwise location, are shown in Fig. 4.7(b). There is no significant difference between the results for the two different pressure coefficient distributions. It can be concluded from the figures that a stronger pressure gradient results in a higher crossflow velocity and higher growth rate of unstable modes. However, the spanwise wavelength of the most unstable mode changes slightly.

The most unstable case, namely, the one with the THU pressure coefficient and 44.5 m/s free-stream velocity, is chosen as the baseline case to test the plasma control method. The free-stream velocity of 44.5 m/s is chosen as the reference velocity with respect to which all the velocities and their components are scaled. Figure 4.8 shows the N-factors of steady modes with different spanwise wave numbers for the baseline case. Generally, the transition caused by crossflow instability takes place at $N = 6$. With this criterion, the 4 mm mode will trigger transition at 24% chord length. However, with a

polished leading edge and in a low-turbulence environment, the critical N-factor can be greater than 14[33]. In our case, none of the N-factor reaches 14 before 70% cord length, where the pressure is minimum. The modes with 4, 5, and 6 mm spanwise wavelength have the greatest N-factor in succession, and they are all promising candidates for the dominant mode. The 3 mm mode grows rapidly near the leading edge and reaches a peak at 20% chord length, after which it declines. The modes with 2 mm and shorter spanwise wavelength are always stable, which are not shown in the figure.

The e^N method is based on the assumption of linearity. However, when the mode amplitudes are large enough, such as 10% of the free-stream velocity, the nonlinearity will affect disturbance evolution. Therefore, NPSE has to be employed to resolve the disturbance in the boundary layer. The promising modes predicted by the e^N method are seeded at the inlet, all with initial amplitude of 5×10^{-5}. The mode amplitude in the NPSE computation is defined as

$$\mathrm{Amp} = \exp\left(\int_{x_0}^{x} -\alpha_i \, d\xi\right) \max\left(\sqrt{|\hat{u}|^2 + |\hat{v}|^2 + |\hat{w}|^2}\right)_y . \tag{4-2}$$

Amplitudes of the primary modes as functions of the streamwise coordinate are shown in figure 4.9. All the harmonics are excited by the nonlinearity, which are not shown in the figure. The peak value of the 3 mm mode amplitude is nearly one order of magnitude lower than the others. The 5 mm mode is first to reach the saturation. Therefore, the 5 mm mode is chosen as the target mode, and the following control methods all aim at this mode.

4.2　采用等离子体激发器推迟后掠翼上流动转捩

4.2.1　Harmonic control: one actuator per wavelength

As mentioned before, there are seven constants (a_0, a_1, a_2, b_0, b_1, b_2, and c_{force}) that need to be determined in the plasma model. Dörr and Kloker pointed out that the body force should spread over the boundary layer but not extend beyond its edge[30]. Figure 4.10 shows the primary and crossflow velocity profiles at streamwise locations $X/C = 0.15, 0.2,$ and 0.25. It can be seen that the boundary-layer edge is at roughly 1.2 mm height. Beyond this height, the primary velocities became constant and the crossflow velocities vanish rapidly. Based on these baseflow velocity profiles, the designed body force distribution is shown in figure 4.11 and the corresponding constants are listed in Table 4.1. The

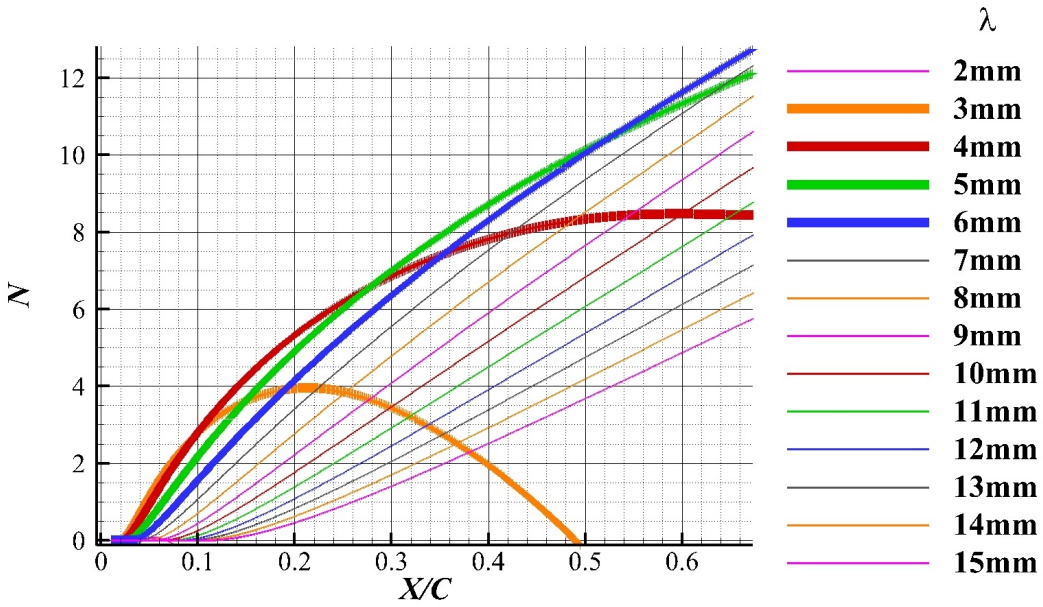

图 4.8　N-factor for the case U_∞ = 44.5 m/s.

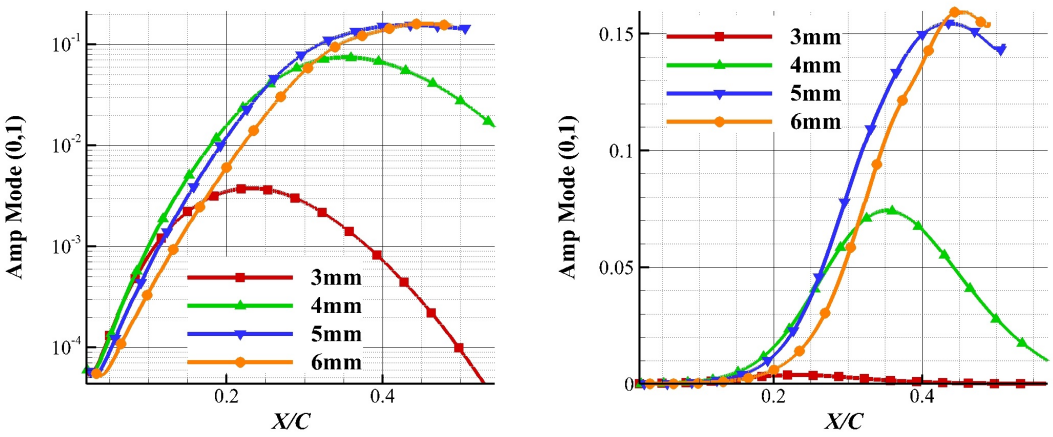

图 4.9　Amplitudes of modes with different spanwise wavelengths (NPSE results).

coefficient c_{force} controls the force strength. The force strength effect is thus studied by choosing 3 values of c_{force}. Figure 4.11 shows the case with $c_{\text{force}} = 30$. For the other two cases, the distributions have the same shape, but with the values all increased proportionally. The body force is distributed under 1.2 mm and the spread length in the z direction is less than 2.5 mm, nearly half of the target mode wavelength. The maximum force densities are 2986, 4976, and 6967 N/m^3 corresponding to c_{force} of 30, 50, and 70, respectively. The total forces, obtained by integrating over the whole y-z cross-section containing a DBD, are 1.467×10^{-3}, 2.446×10^{-3}, and 3.424×10^{-3}N/m, respectively. It is worth mentioning that the maximum force density was as high as 7000 N/m^3 in Kriegseis's experiment[28].

Actuators with the previously described body force distribution are utilized to attenuate crossflow instability. To hinder crossflow vortices directly, one actuator is positioned per wavelength. The distribution of the dimensionless force f in the X–Z plane at $y = 0.1$ mm is shown in Fig. 4.12. All the electrodes are parallel to the isophasal lines of the primary crossflow instability mode. The spanwise distance of each pair of neighboring actuators is just the wavelength of the primary mode. The control region starts at 23.7% chord length and ends at 26.2% chord length. In this case, $c_{\text{force}} = 30$. Ten different spanwise locations of the actuators are examined to find the optimal one. The flow does not always become stabler in all cases, with some arrangements can promote the transition. Figure 4.13 shows the evolution of the fundamental modes in the most stable and unstable cases. The black curve stands for the case without control, and the green and red curves for the most stable and unstable cases, respectively. Here, T_z is the fundamental spanwise wavelength and z_0 is the spanwise coordinate of the central point of the middle actuator. The control region is indicated by the two vertical blue lines. When the actuators locate at $z_0/T_z = 0.4$, the primary mode is weakened in the control region and its amplitude is lower than that in the case without control downstream. However, when the actuators locate at $z_0/T_z = 0.9$, just half a wavelength away from the formal most stable case, the primary instability mode is promoted. The amplitudes increase in the control region and become much higher than that in the no-control case.

Figures 4.14 depict the actuator locations relative to the instability disturbance. The colors denote the body force, and the iso-lines show the disturbance velocities without control. All the forces and velocities are projected onto the direction perpendicular to the crossflow vortex. It can be seen that when the force and the local disturbance have the

表 4.1　Constants in the plasma model

a_0	a_1	a_2	b_0	b_1	b_2	c_{force}
2.0	0.08	0.001	7.76	2.1	1.8	30,50,70

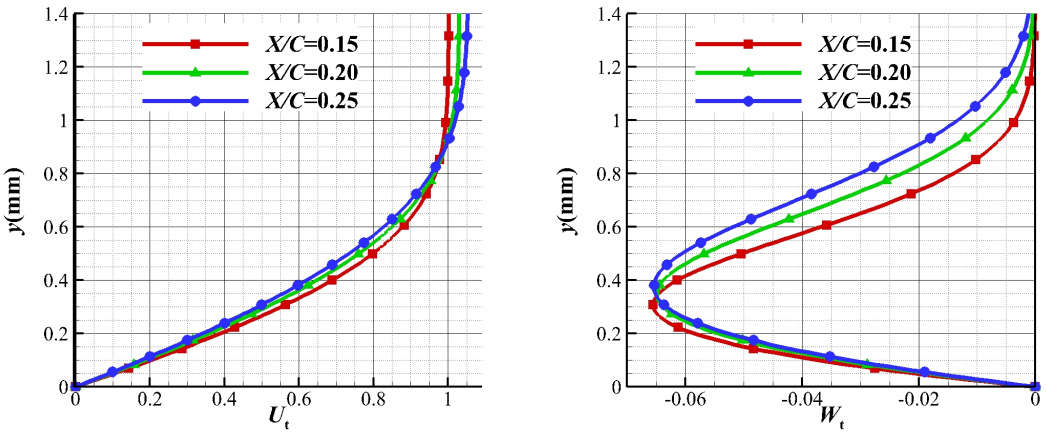

图 4.10　Primary velocity profiles (left) and crossflow (secondary) velocity profiles (right).

same sign, both negtive shown in figure 4.14(b), instability is promoted. In contrast, when the force and the disturbance velocities are in opposite directions (see figure 4.14(a)), the disturbance will be damped and thus the instability will be attenuated. This result implies that the spanwise position is critical, and an unfavorable position can even lead to a stronger disturbance that may bring the transition further upstream. For application of this control method to a real aircraft, it would be essential to locate the positions of all the crossflow vortices, which would be a tremendous challenge. Hence, in our view, this method is not suitable for practical application.

4.2.2　Subharmonic control: two actuators per wavelength

Since it is known that the magnitude of the crossflow velocity greatly influences crossflow instability, another idea is to use plasma actuators to attenuate the crossflow velocity. To avoid exciting the primary mode, two actuators are positioned per wavelength. The body force distribution in the X—Z plane is shown in figure 4.15. The number of plasma actuators is doubled compared with the previous scheme. The control region starts at 18.7% chord length and ends at 21.2% chord length. The electrodes are still parallel to the isophasal curves of the primary instability mode. $c_{\text{force}} = 50$ in the first case; the cases

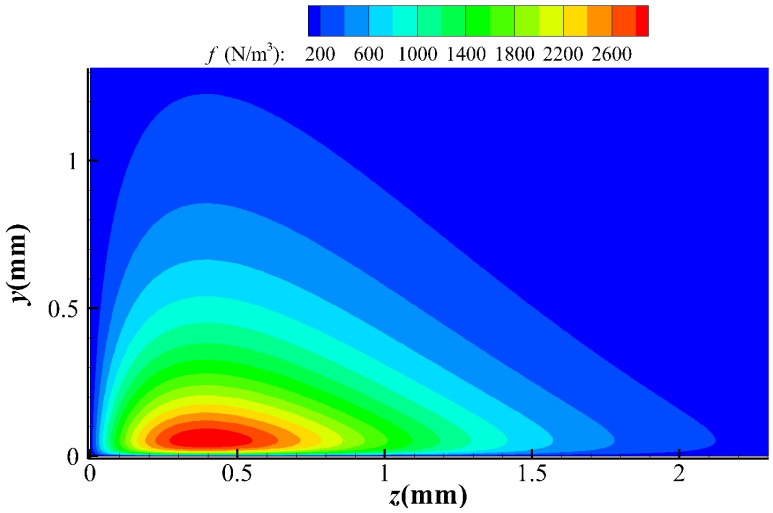

图 4.11　Distribution of body force induced by a single plasma actuator

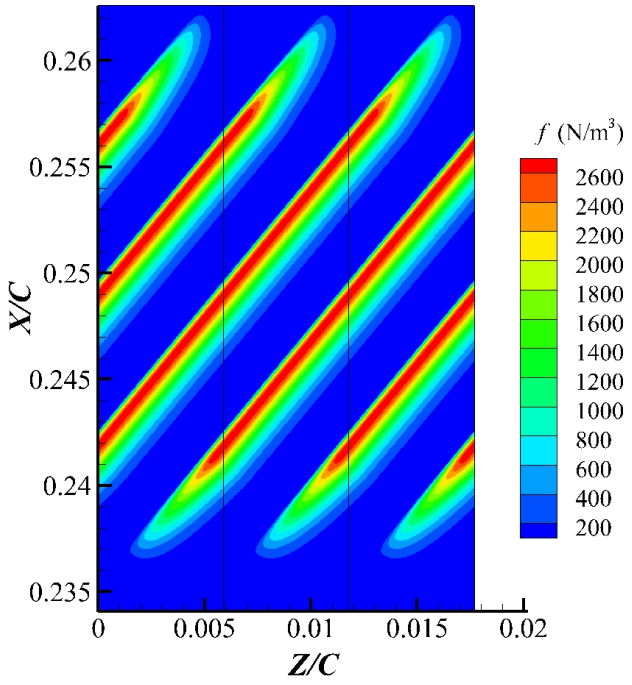

图 4.12　Distribution of body force in the X–Z plane (y = 0.1 mm) with one actuator per wavelength.

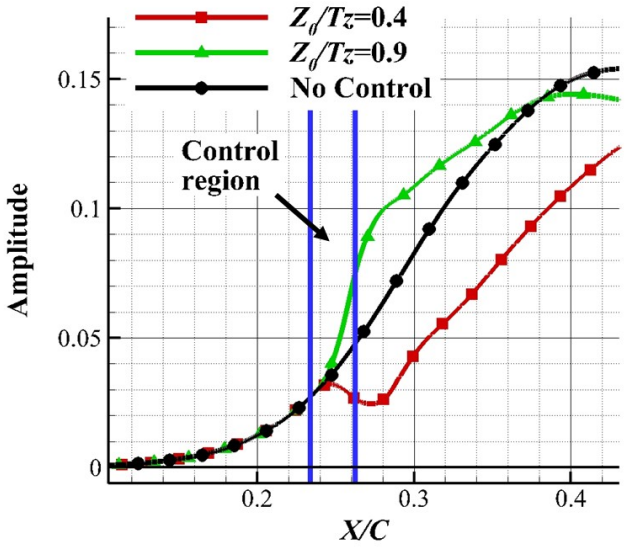

图 4.13　Amplitudes of fundamental modes with actuators placed at different spanwise locations.

with $c_{\text{force}} = 30$ and 70 will be given afterwards.

Figure 4.16 shows the evolution of the disturbance energy. The red curves stand for the controlled case and the black curves for the uncontrolled case. The right figure uses a normal coordinate, whereas the left uses a logarithmic coordinate to show the harmonics more clearly. Again, the control region is denoted by two blue vertical lines in both figures, and the center of the region is at 20% chord length. Since the distance between two neighboring actuators is half the fundamental wavelength, the harmonic mode $(0, 2)$, whose wavelength is also half the fundamental wavelength, is excited directly. It can be seen that there exists a small peak right at the end of the control region. When the mode leaves the control region, its energy decreases rapidly, and at 30% chord length its energy becomes two orders of magnitude lower than the peak value. The reason for this energy decline is because this mode with 2.5 mm wavelength is predicted to be stable by the e^N method, meaning that it will die out soon without plasma stimulation. The behaviors of other harmonics, from $(0, 3)$ to $(0, 5)$ modes, and all the higher-order harmonics (not shown) are all similar to that of the $(0, 2)$ mode. However, in the middle section of the wing, from 30% to 40% chord length, all the modes are weaker than their counterparts from the case without control.

Figures 4.17 and 4.18 show contours of the streamwise velocity at $X/C = 0.216$ and 0.35, respectively. At $X/C = 0.216$, close to the end of the control region $X/C = 0.212$, the boundary layer looks quiet and clean without control. The instability modes are very

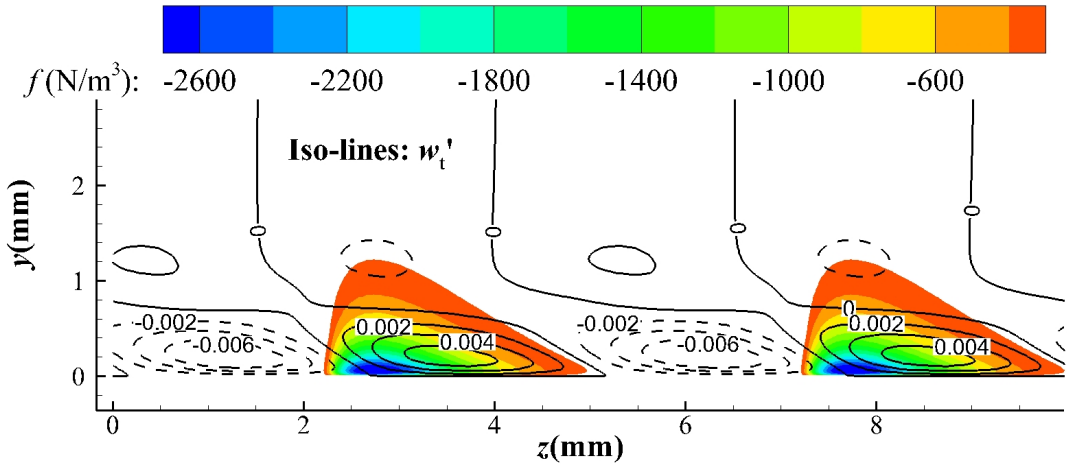

(a) $z_0/Tz = 0.4$

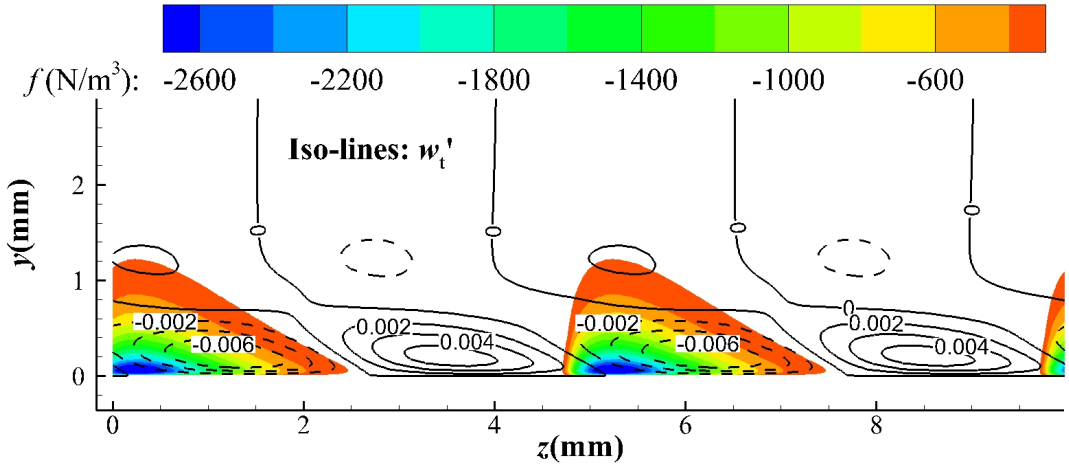

(b) $z_0/Tz = 0.9$

图 4.14　Relative positions of body force and crossflow-wise disturbance velocity. The colors denote the body force, and the iso-lines show the disturbance velocities without control.

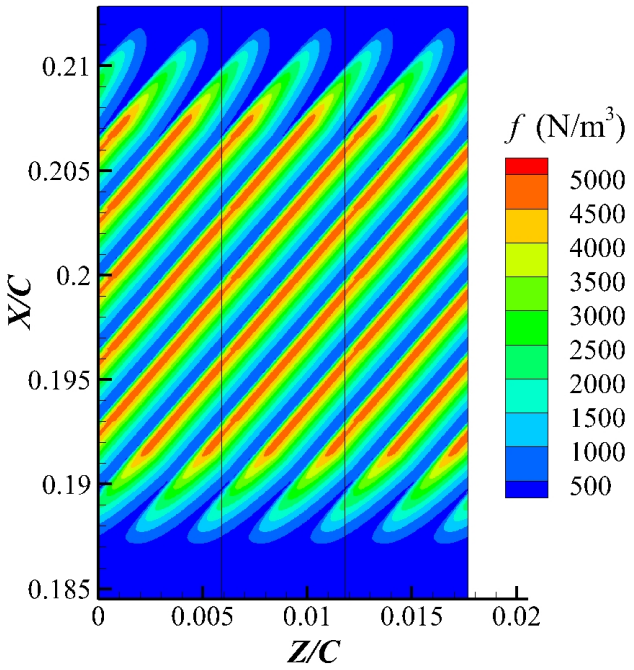

图 4.15　Distribution of body force in the X–Z plane (two actuators per wavelength).

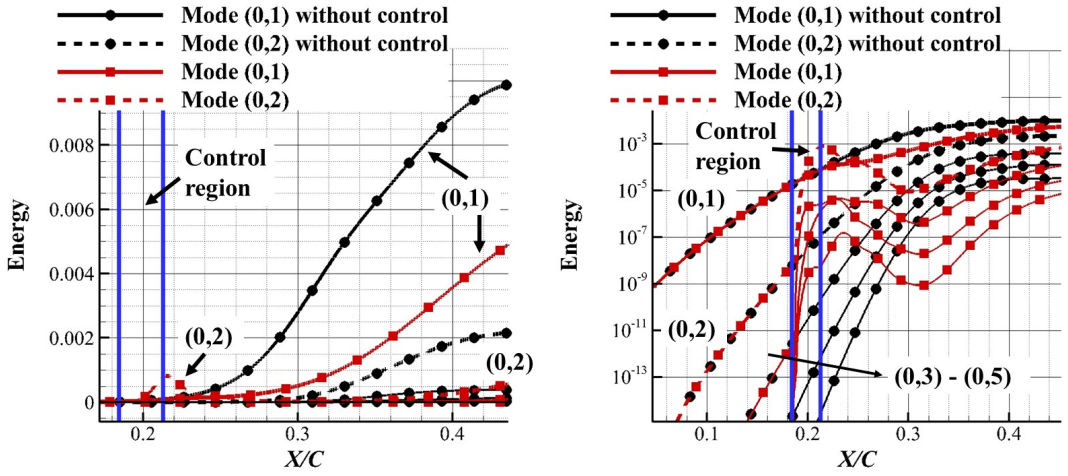

(a)　(b)

图 4.16　Evolution of mode energy with and without control.

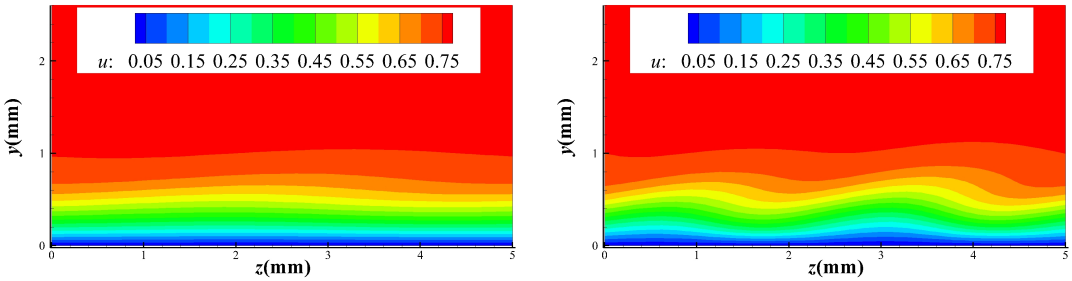

(a)　(b)

图 4.17　Contours of streamwise velocity at X/C = 0.216 (a) without and (b) with control.

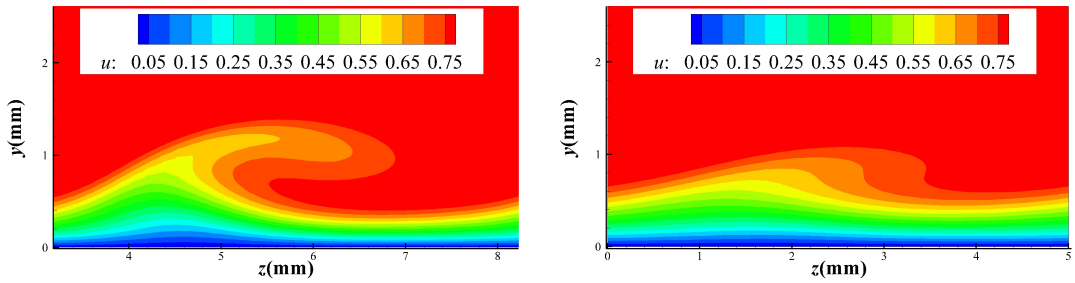

(a)　　(b)

图 4.18　Contours of streamwise velocity at $X/C = 0.35$ (a) without and (b) with control.

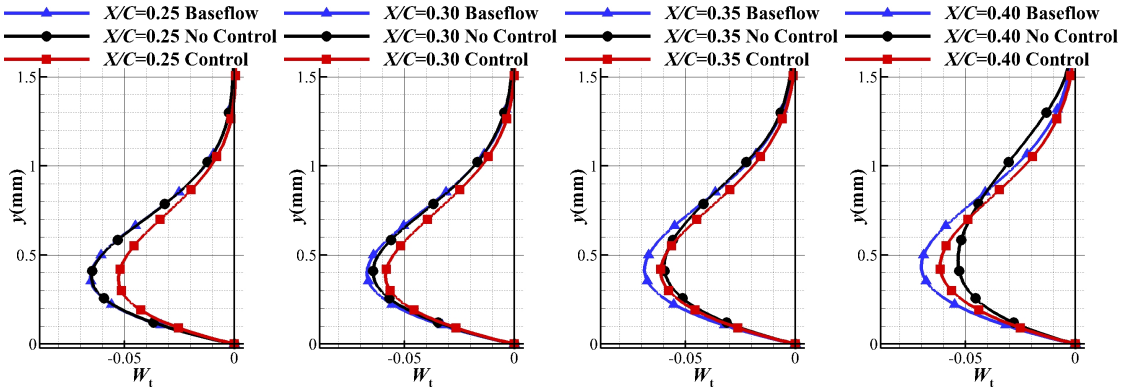

图 4.19　Crossflow velocity profiles.

weak there. When the plasma is induced, small waves are generated, seen in figure 4.17(b). These small waves are mainly caused by the (0,2) mode and have wavelength 2.5 mm. At 35% chord length, in the case without control, a strong crossflow vortex appears and convects low-momentum fluid away from the wall. A rollover structure that indicates the beginning of the saturation stage also appears. However, for the controlled case, there appear only small ripples, and no strong convection emerges. From these figures, it can be concluded that even though the plasma actuators do not affect the primary mode directly, their effects do ultimately hinder the evolution of crossflow vortices.

Figure 4.19 shows the crossflow velocity profiles at different streamwise locations. The blue curves stand for the crossflow velocity profiles of the baseflow. The black curves represent the uncontrolled case, and they deviate from the baseflow profile owing to the mean flow distortion mode, namely, the $(0, 0)$ mode. The red curves stand for the controlled case. It can be seen that at $X/C = 0.25$, the black curve coincides with the blue one, because all the disturbance modes, including the mean flow distortion mode $(0, 0)$, are weak there. Meanwhile, since the direction of the plasma-induced body force is opposite to that of the crossflow velocity, the profile in the controlled case is lower than in the other

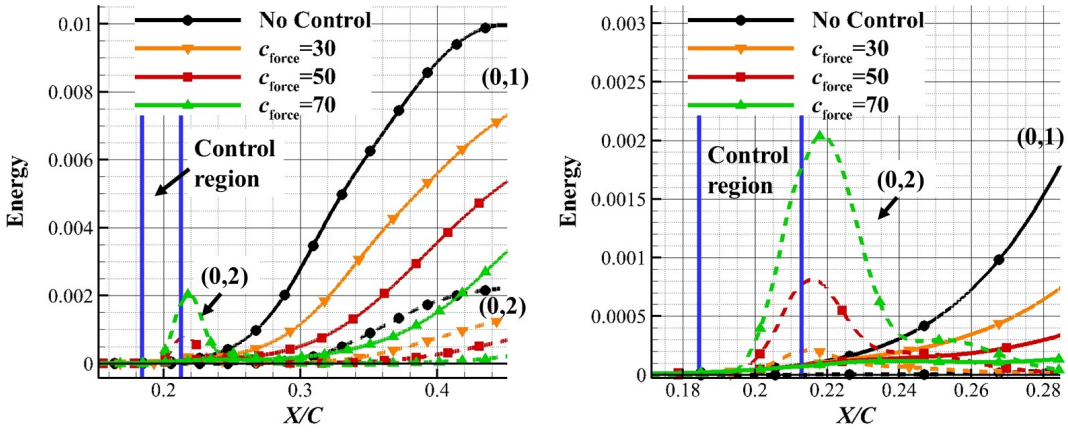

图 4.20　Evolution of mode energy for different body force strengths.

two cases. The situation is similar at $X/C = 0.3$. The controlled crossflow profile grows marginally, but it is still lower than that in the other two cases. From 25% to 30% chord length, all the instability modes in the controlled case grow slower than their counterparts in the uncontrolled case, and some of them even shrink [see figure 4.16(b)]. This is mainly attributed to the decrease in the crossflow velocity profile. At 35% and 40% chord length, the effect of nonlinearity promotes distortion of the mean flow and a decrease in the crossflow for the uncontrolled case. However, since the development of these instability modes is hindered in the controlled case, the nonlinearity is not significant and thus the distortion of the controlled baseflow is not as intense as that in the case without control. Then, the controlled crossflow become stronger than in the case without control, as can be seen in the last picture in figure 4.19.

The effect of force strength is studied by varying the coefficient c_{force}, and the results are shown in figure 4.20. The right figure zooms in the vicinity of the control region in the left figure. The orange, red, and green curves stand for the cases with $c_{\text{force}} = 30$, 50, and 70, respectively. In all the controlled cases, the energies of the primary modes and the $(0, 2)$ modes are all lower than those in the case without control, and a stronger body force results in weaker instability. A stronger body force also leads to higher peak value of the energy of the harmonic $(0, 2)$ mode near the end of the control region. It can be seen that the peak values are 2×10^{-4}, 8×10^{-4}, and 2×10^{-3} for the cases with $c_{\text{force}} = 30$, 50, and 70, respectively.

Figure 4.21 compares the results for cases with actuators positioned at different streamwise locations. The green, red, and orange curves stand for the cases with DBD centers located at 15%, 20%, and 25% chord length. The control regions are not plotted

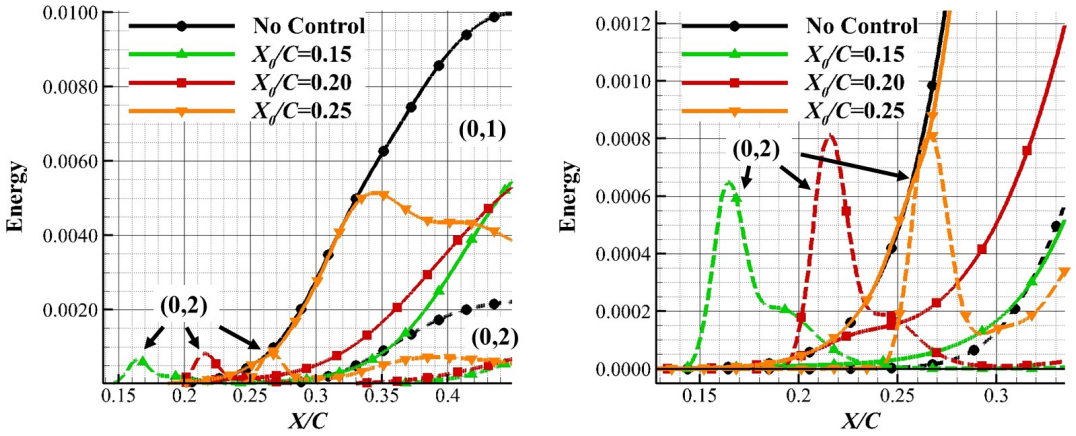

图 4.21　Evolution of mode energies with plasma actuators at different streamwise locations.

on the figure, but they can still be recognized by the small peaks on the dashed curves denoting the $(0, 2)$ instability modes, because, like all the other cases shown previously, in the vicinity of the control region, the $(0, 2)$ modes are all excited. The peak of the $(0, 2)$ mode in the case with excitation at 15% chord length is lower than that at 20% chord length, which in turn is lower than that at 25% chord length. The reason is that the amplitude of the uncontrolled $(0, 2)$ mode is larger downstream, and thus, when it is excited by the same force, the originally strong mode reaches an even higher level. From 30% to 40% chord length, all the mode energies for the case controlled at 15% chord length are lower than their counterparts in the other two cases. The primary mode controlled by the DBD actuators at 25% chord length does not deviate from the primary mode without control until 33% chord length. Fortunately, its energy decreases after that. No matter where the actuators are placed, all the mode energies are lower than in the original case without control.

It has already been mentioned in Section 4.2.1 that the controlled results with one plasma actuator per wavelength are remarkably sensitive to the spanwise location of the actuators. The sensitivity of the control method with two actuators per wavelength to spanwise location is examined here, as shown in figure 4.22. Since the wavelength of the array of plasma actuators is half the fundamental wavelength T_z, the actuators are moved one-quarter of the fundamental wavelength reversed for phase in the spanwise direction. The red curves stand for the original case, and the green curves represent the new case with the spanwise location of the actuators shifted. Again, the energy of the $(0, 2)$ mode increases in the control region and decreases elsewhere. The energies of the $(0, 1)$ modes in both cases remain the same in the control region. However, they begin to deviate from

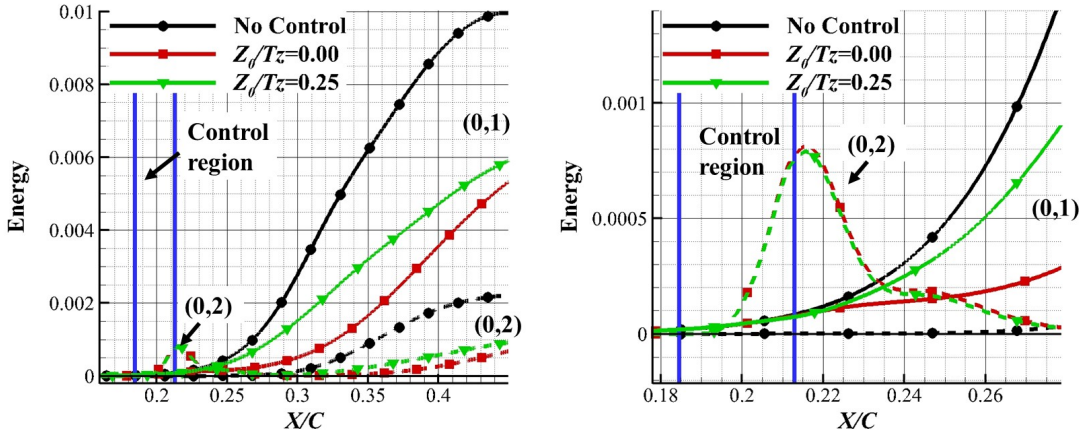

图 4.22　Evolution of mode energies with plasma actuators at different spanwise locations.

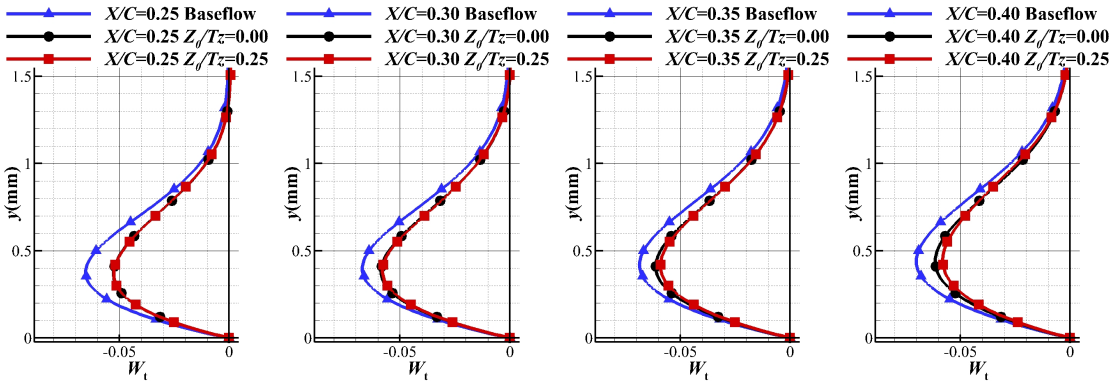

图 4.23　Comparison of modified mean flow profiles with plasma actuators at different spanwise locations.

each other just slightly downstream of the control region. From 25% to 45% chord length, there is only a small difference between these two curves. In addition, both of them are below the black curve, the one without control, indicating that the spanwise locations of the actuators are not crucial.

To explain the slight difference between the primary modes from the cases with and without a shift in the spanwise location of the actuators, the mean flow profiles in the crossflow direction are compared in figure 4.23. The blue and red curves denote the mean crossflow velocity profiles in the cases with and without a spanwise shift of the actuators, respectively. At 25% and 30% chord length, the red curves are perfectly superposed on the blue curves. It should be recalled that at these two streamwise locations, the energies of the primary modes have already deviated from each other. Hence, it can be concluded that the difference between the $(0, 1)$ modes in the two cases is not caused by the mean crossflow velocity profile.

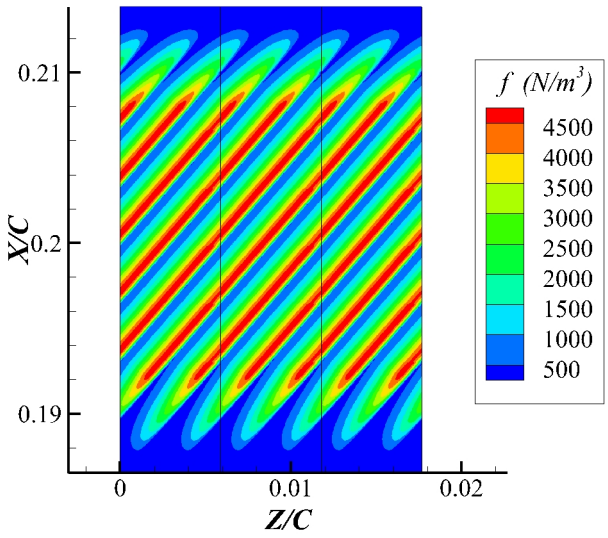

图 4.24　Body force distribution of inverse plasma actuators in the X–Z plane.

To date, it is clear that manipulation of the $(0, 0)$ mode[34] or the $(0, 2)$ mode can result in a decrease in the energy of the primary mode. In the DBD plasma actuators control scheme presented here, the $(0, 0)$ and $(0, 2)$ modes are both altered directly and the primary mode is affected only downstream of the control region. It is not clear which mode, $(0, 0)$ or $(0, 2)$, contributes more to the decline in the energy of the primary mode. To answer this question, a reversed control case is examined. All the DBD actuators are turned 180°, with the body force in the opposite direction. In the computation, the force appears as a source term. When analyzing each mode, the force term is decomposed into Fourier series with respect to the spanwise coordinate. These Fourier components affect the corresponding instability modes. For instance, the zeroth-order Fourier component affects the $(0, 0)$ mode directly and the second affects the $(0, 2)$ mode. For this reverse control, the sign of the force term and that of its Fourier component are switched. Owing to the properties of trigonometric functions, the sign switch of the second Fourier component is equivalent to a phase shift. This phase shift effect has been investigated above by comparing results with actuators at different spanwise locations, and has been shown to be trivial. Thus, the biggest difference in this reverse control is that the sign of the force term corresponding to the $(0, 0)$ mode is switched. If this reverse control still works and reduces the energy of the primary mode, then the $(0, 2)$ mode rather than the $(0, 0)$ mode will play a more important role in our control scheme. Otherwise, the conclusion will be that the $(0, 0)$ mode is more important.

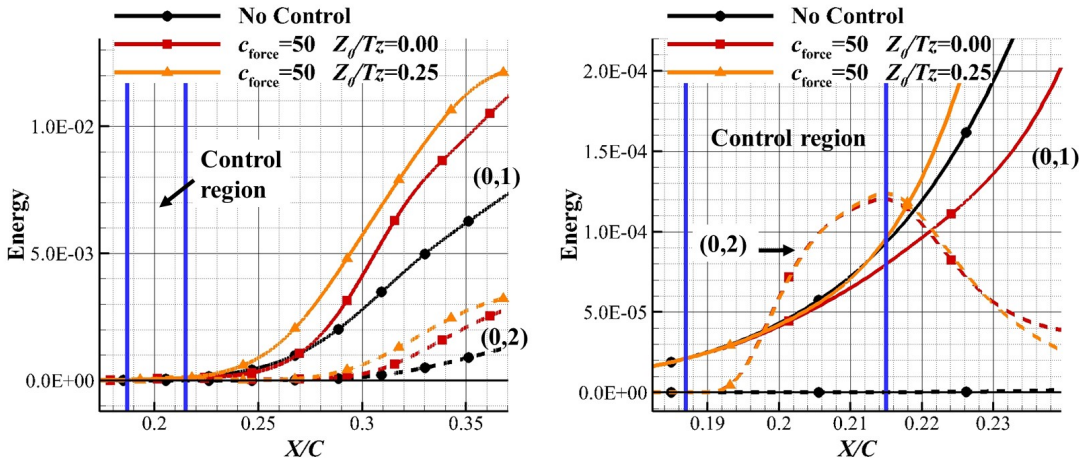

图 4.25　Evolution of mode energy in reversed control cases (with actuators at two different locations).

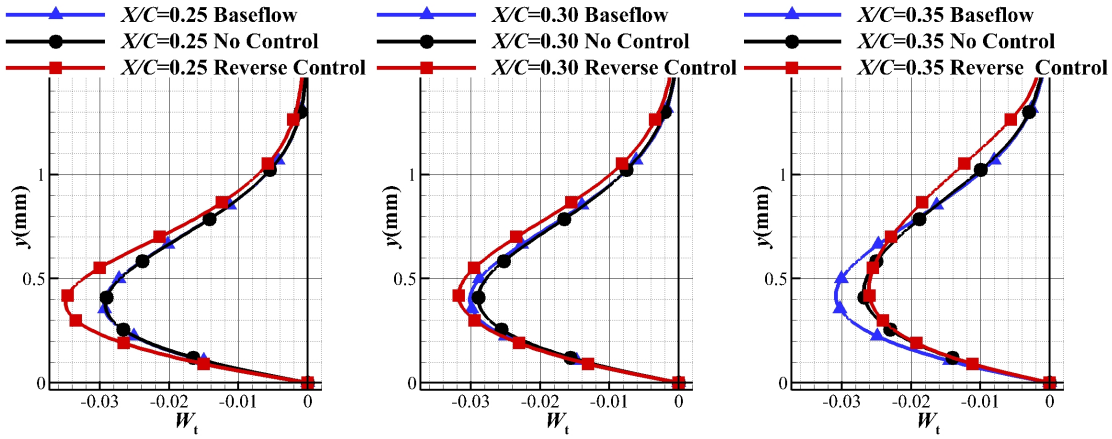

图 4.26　Mean crossflow profile in the reversed control case.

The body force distribution in the $X-Z$ plane is shown in figure 4.24. The evolution of the mode energies in reverse control cases is shown in figure 4.25. As mentioned above, reversal of the force direction will also lead to a phase shift of the Fourier component corresponding to the $(0, 2)$ mode. This phase shift can be achieved by moving the actuators in the spanwise direction. To eliminate this small ambiguity, actuators located at $Z_0/T_z = 0.0$ and $Z_0/T_z = 0.25$ are both simulated. It can be seen that in both cases the energies of the primary modes are higher than that in the controlled case. Also, the effect of actuator spanwise location is not significant, and this agrees well with the conclusion reached above (see Fig. 4.23). This result indicates that the $(0, 0)$ mode is more important than the $(0, 2)$ mode and is the main cause of the decline in the energy of the primary mode.

Figure 4.26 shows the mean crossflow velocity profiles at different streamwise loca-

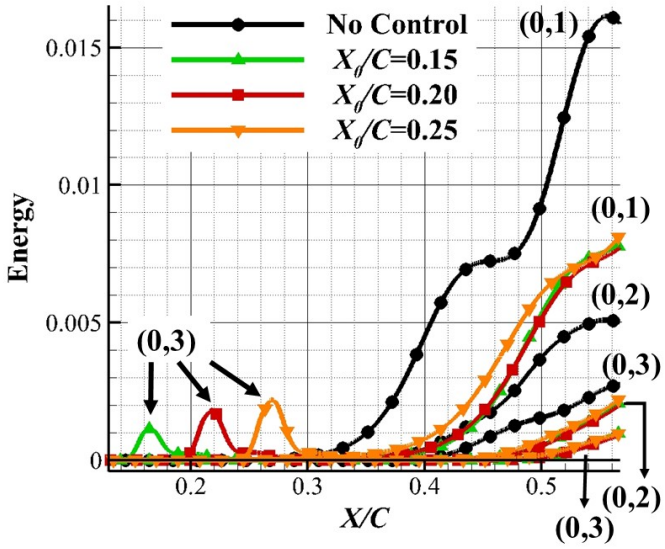

图 4.27　Evolution of mode energy in cases targeted at the 7.5 mm wavelength mode.

tions in the reverse control case. It is obvious that the crossflow is enhanced at 25% chord length, just downstream of the control region. Thereafter, the crossflow falls back and finally returns to the same level as that in the case without control. From this result, it can be concluded that the crossflow velocity has a significant effect on crossflow instability. When the crossflow is weakened by the actuator, the instability is attenuated. Otherwise, the instability is intensified.

4.2.3　Off-designed case

All the simulations shown above assume that the mode with 5 mm spanwise wavelength dominates the transition, and the 2.5 mm mode, happens to be the $(0, 2)$ mode with respect to the 5 mm fundamental wavelength. Here, another situation is considered in which the 7.5 mm mode becomes dominant but the distance between two neighboring actuators is still 2.5 mm. Thus, the control mode is the $(0, 3)$ mode. Plasma actuators are positioned at three different streamwise locations, and the evolution of the mode energy is shown in figure 4.27. The green, red, and orange curves stand for the cases controlled at 15%, 20%, and 25% chord length, respectively. The small peak in the energy of the $(0, 3)$ mode, that is, the control mode, becomes stronger and stronger when the actuators are moved downstream. Fortunately, all the modes in all the controlled cases are weaker than those in the uncontrolled case downstream of 30% chord length. This result proves that the presented control method performs well even in an un-designed case.

第5章　等离子体激发器控制充分发展槽道湍流

本文进行控制的基本算例选取为壁面摩擦尺度雷诺数$\mathrm{Re}_\tau = 180(\mathrm{Re}_m = 5600)$的湍流槽道。计算程序采用的是王志坚课题组的hpMusic[?]，时间步长dt=0.00015，用三阶的显式Eular进行时间推进；空间采用4阶精度计算，单元内采用高斯点，每个单元内有$5 \times 5 \times 5$个点，三个方向总的自由度数分别为$235 \times 155 \times 200$。在后处理的时候，对分布在单元界面，空间位置相同的点进行了平均。平均处理之后用于显示的网格点数与Kim（1987）[?]文献中的网格相近。计算域大小为$4\pi \times 2 \times 2\pi$。$\gamma$=1.4，气体常数为1.0，普朗特常数Pr = 0.72，粘性系数$\mu = 3.571428571428571 \times 10^{-4}$， Ma=0.1。计算时在流场内添加全场均匀的体积力，使得槽道内的质量平均流速在稳定在1.0；计算的初始条件为抛物线形速度刨面，流速峰值$u_{\max} = 1.327$。为了加快转捩，在这个流场上叠加上10个不同流向展向波数的扰动波。初始的密度$\rho = 1.0$；压力$p = 31.74603174603175$；这两个量在计算的时候基本上不会变化。计算得到的近壁涡结构和条带结构如下图： 计算得

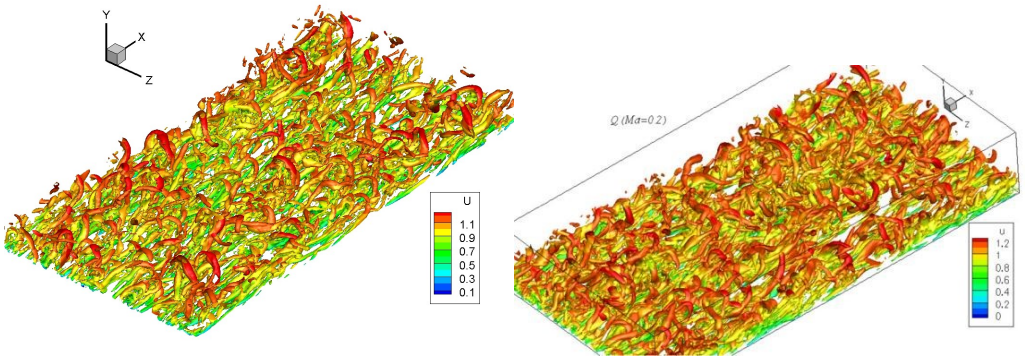

(a) 本文计算结果　　(b) Liang Wei 和 Andrew Pollard (2011)[?]

图 5.1　计算得到涡结构对比

到的对数律分布如下： 图5.3中结果为采用190万瞬时结果时间平均加流向和展向平均之后的结果。计算得到的二阶统计量对比： 计算得到的瞬时流场的涡结构图如下： 对于这一基本流动，对其进行条件平均，分别在$y^+ = 10, 15, 20$的平面上进行涡探测，用Q作为探测标准。然后进行条件平均，得到：

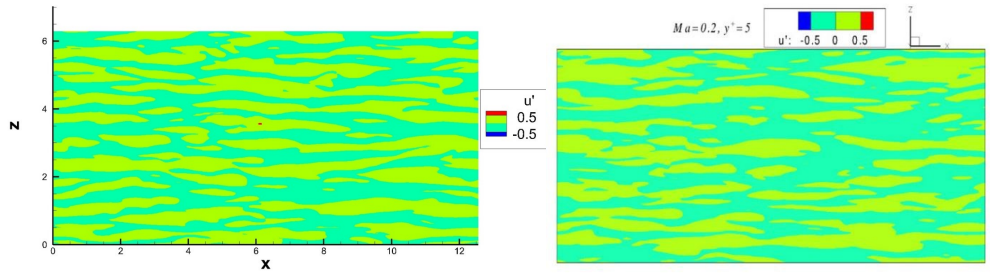

(a) 本文计算结果　　(b) Liang Wei 和 Andrew Pollard (2011)[?]

图 5.2　计算得到条带结构对比

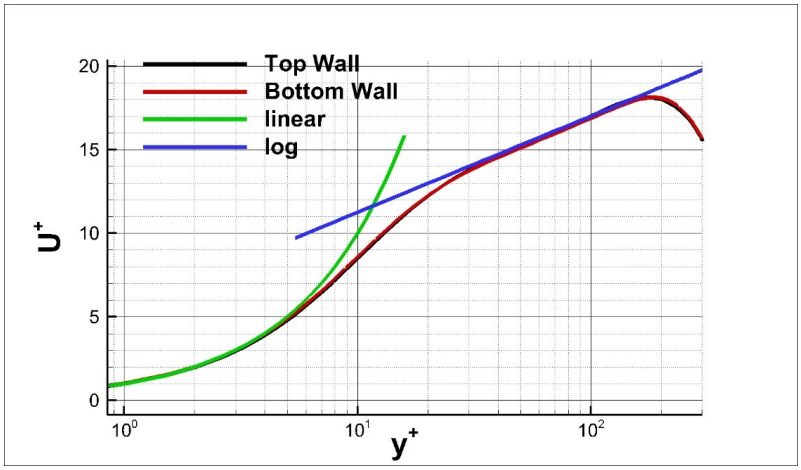

图 5.3　计算结果与对数律对比

5.1　定常激励控制方案

文献中给出了一种大涡形状的体积力分布用于减阻 他们对这种减阻控制方式进行了参数研究： 然而，实际中并不能产生这种形状的体积力，所以本文考虑采用DBD产生相同的效果。本文中采用的体积力分布情况如下： 在没有背景流动的槽道中诱导出来的流动如下： 由于最开始并不知道体积力诱导的涡强度与真实涡强度的关系，所以做了很多参数的实验。最终发现确实过大的体积力反而会起到增阻的的作用。这里仅展示一个增阻的算例和一个减阻的算例，他们的产生的涡强度如下： 各个算例下壁面阻力对比： 流向平均与时间平均对比： Plasma

表 5.1　不同算例产生的涡强度

算例名称	$\max(V)/U_b$
Plasma(Strong)	0.19
Plasma(Weak)	0.05
Vortex Force	0.06

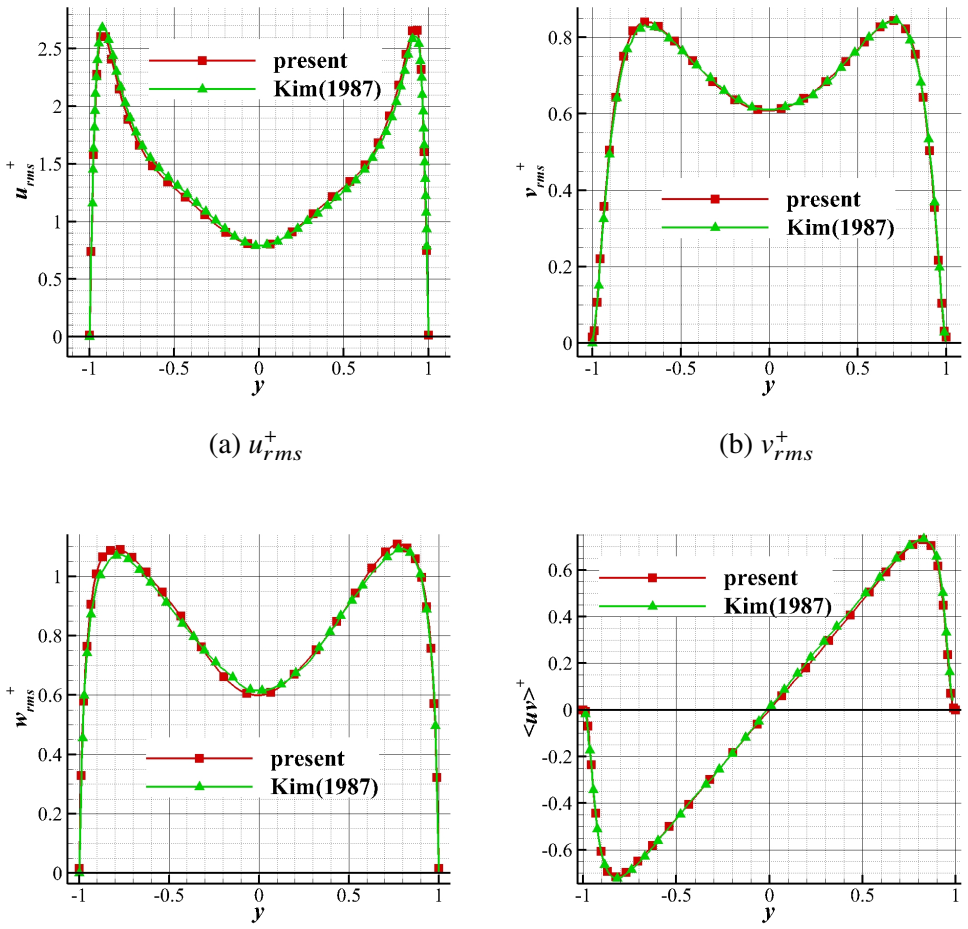

(a) u^+_{rms}　　(b) v^+_{rms}

(c) w^+_{rms}　　(d) $< uv >^+$

图 5.4　计算得到的二阶统计量与文献中的结果对比

（Weak）算例中的涡结构： Plasma（Weak）湍动能和湍动能生成项：

5.2　周期激励控制方案

米兰理工体积力形式：

$$F_z = F_z(y,t) = A_f e^{-y/D} \cos\left(2\pi \frac{t}{T}\right); A_f = 2; D = 0.04 \tag{5-1}$$

控制效果： $T^+ = 52$相平均： 涡结构图： 各阶统计量对比：

图 5.5　瞬时流场的涡结构图

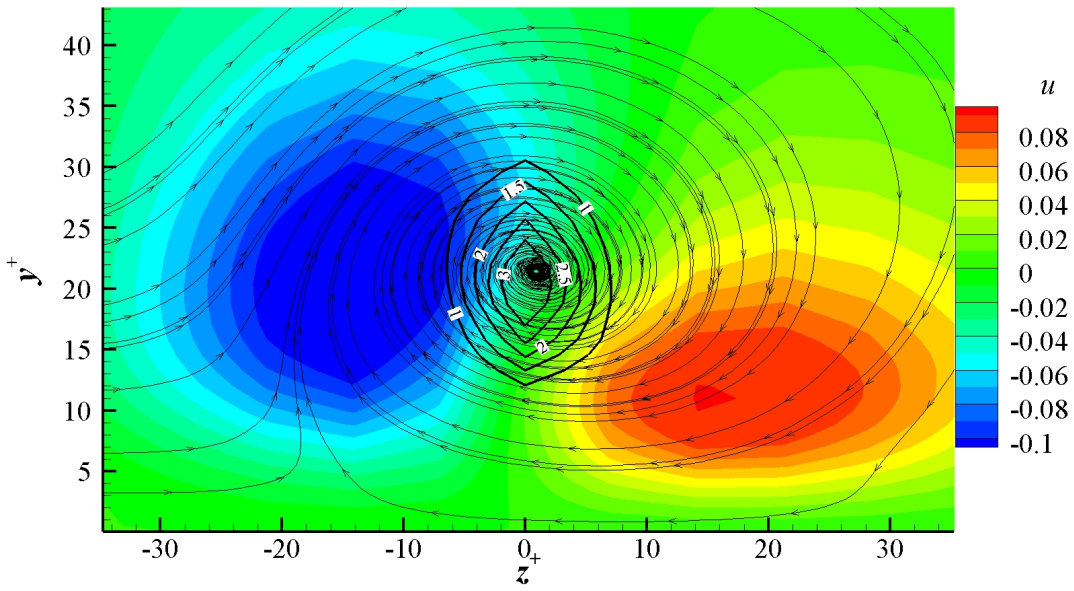

图 5.6　$y^+ = 20$条件平均

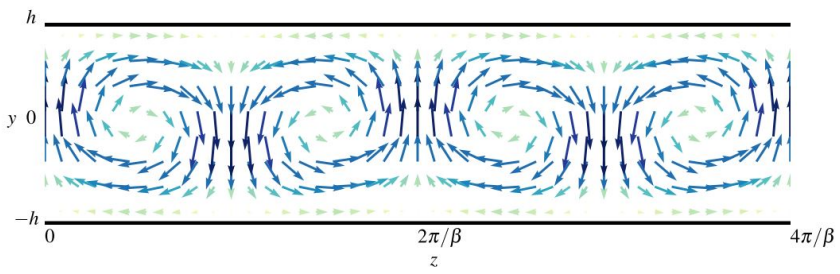

图 5.7　J Canton et al. (2016 FTC)采用的减阻控制的体积力

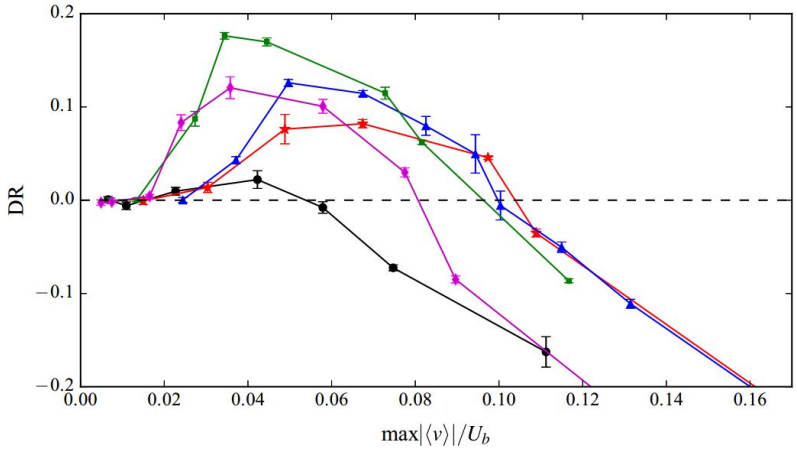

图 5.8　涡强度与减阻率的关系

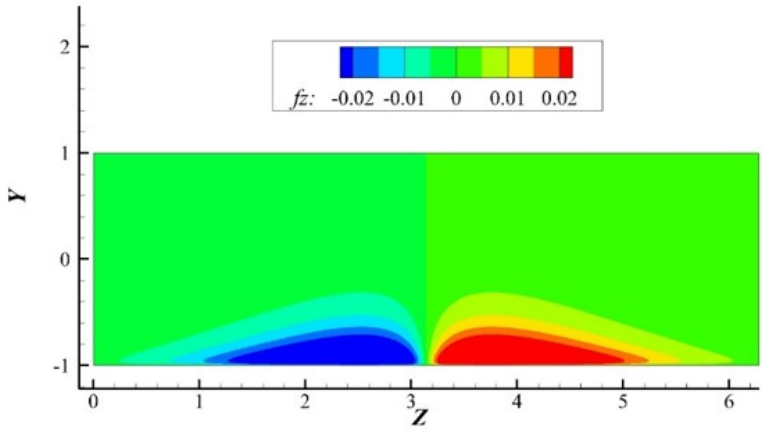

图 5.9　定常激励采用的DBD体积力示意图

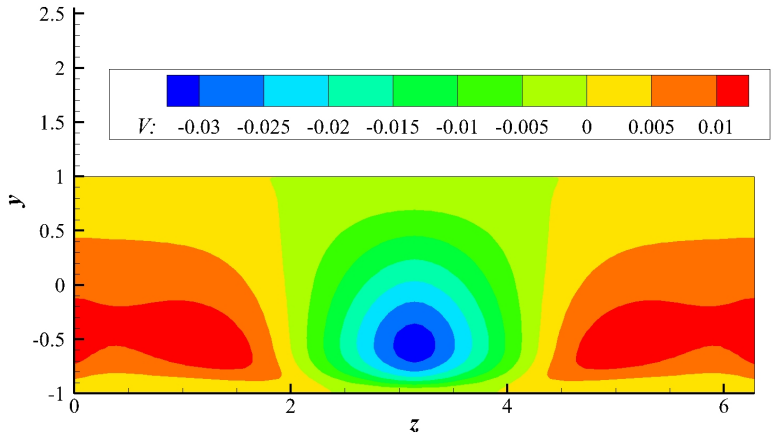

(a) V

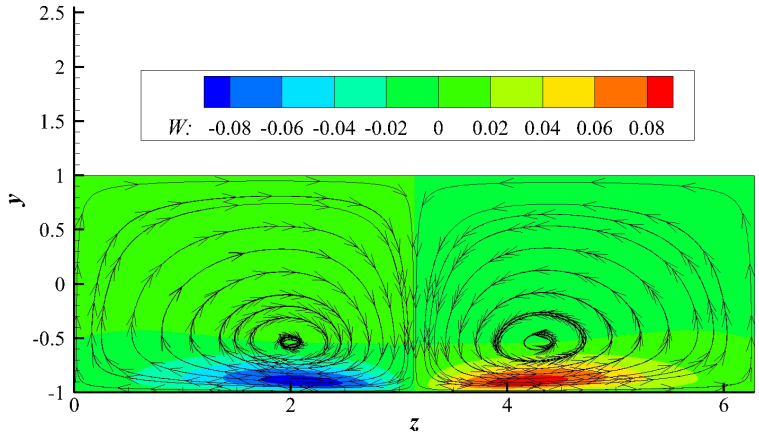

(b) W

图 5.10　定常DBD在无背景流动的槽道中诱导出来的流场

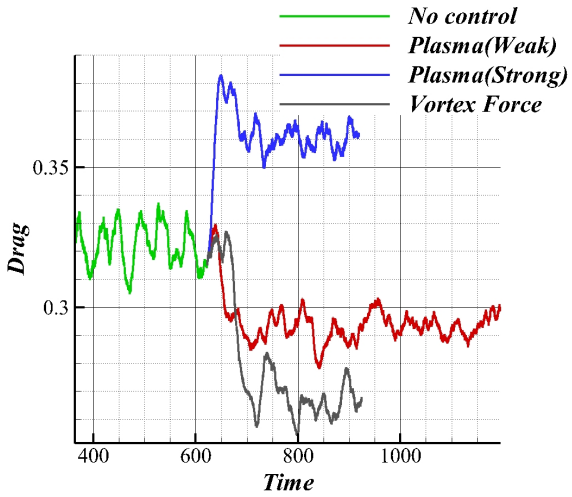

图 5.11　各个算例下壁面阻力对比

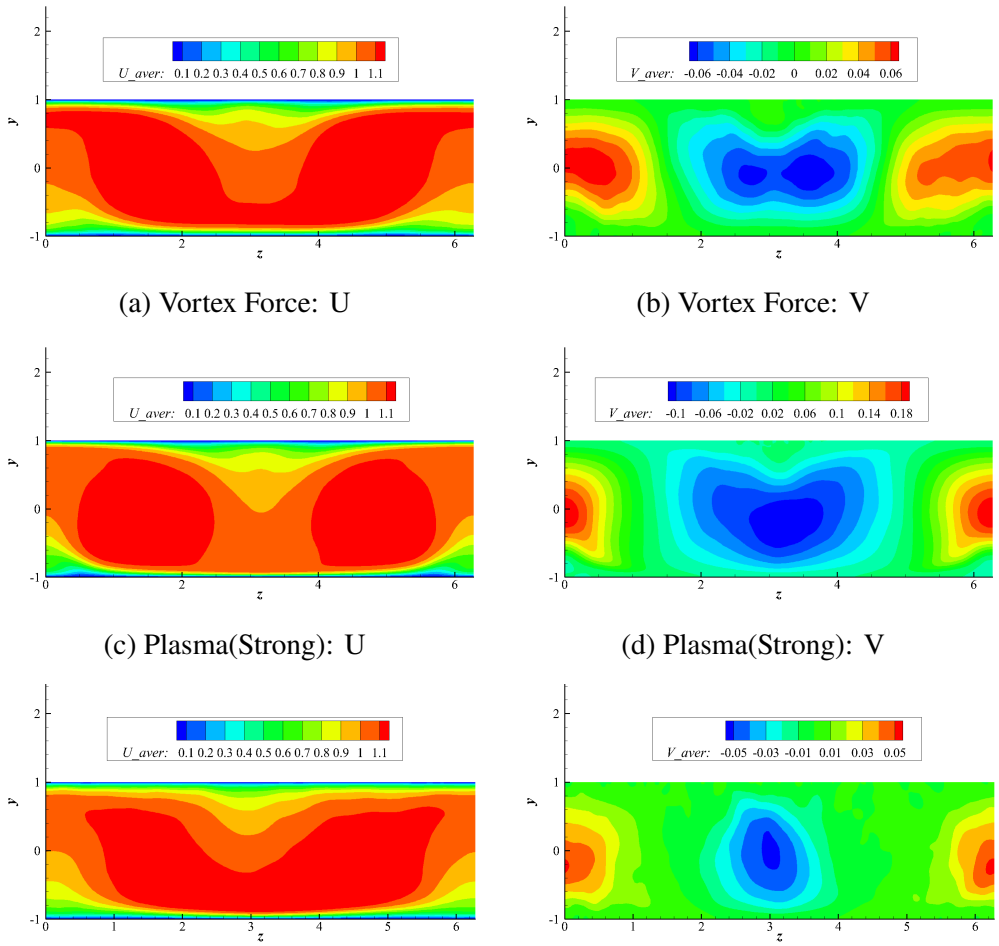

(a) Vortex Force: U　　(b) Vortex Force: V

(c) Plasma(Strong): U　　(d) Plasma(Strong): V

(e) Plasma(Weak): U　　(f) Plasma(Weak): V

图 5.12　流向与法向平均速度

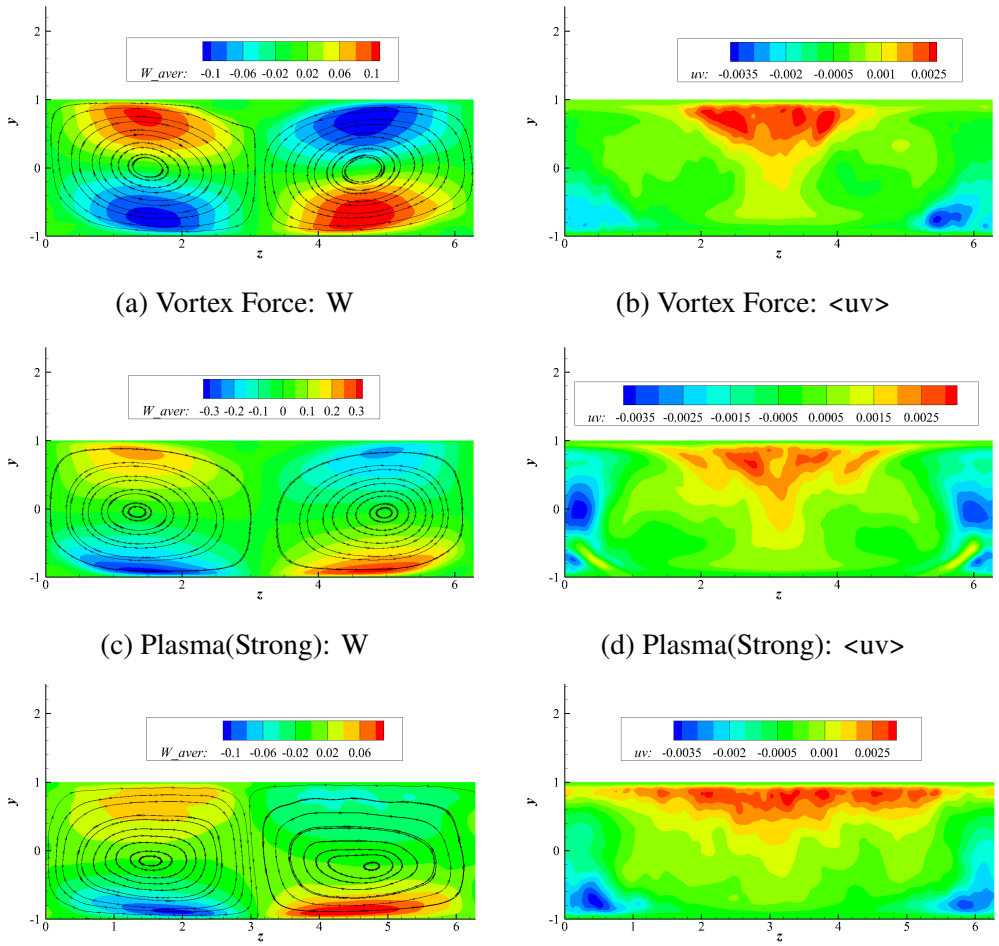

(a) Vortex Force: W　　(b) Vortex Force: <uv>

(c) Plasma(Strong): W　　(d) Plasma(Strong): <uv>

(e) Plasma(Weak): W　　(f) Plasma(Weak): <uv>

图 5.13　展向平均速度与雷诺切应力

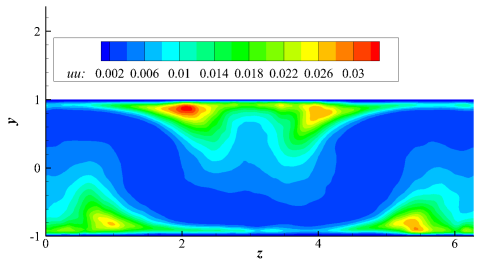

(a) Vortex Force: $< uu >$

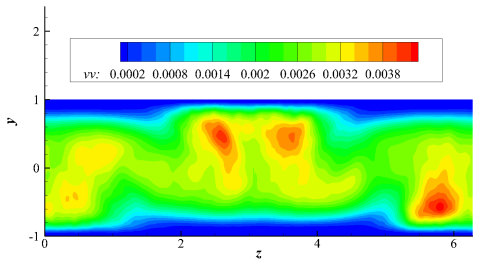

(b) Vortex Force: $< vv >$

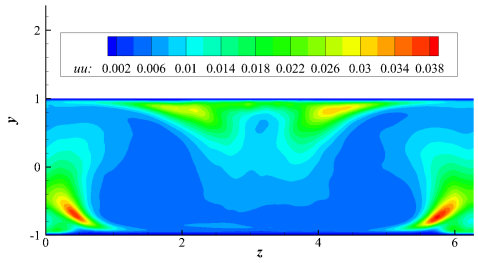

(c) Plasma(Strong): $< uu >$

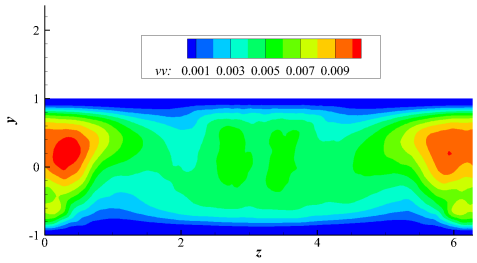

(d) Plasma(Strong): $< vv >$

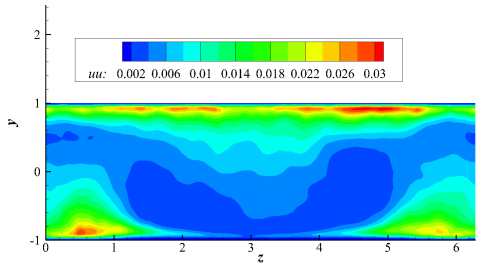

(e) Plasma(Weak): $< uu >$

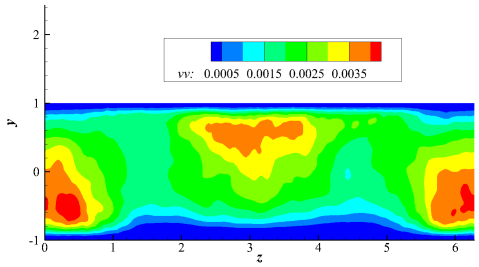

(f) Plasma(Weak): $< vv >$

图 5.14　流向与法向雷诺主应力

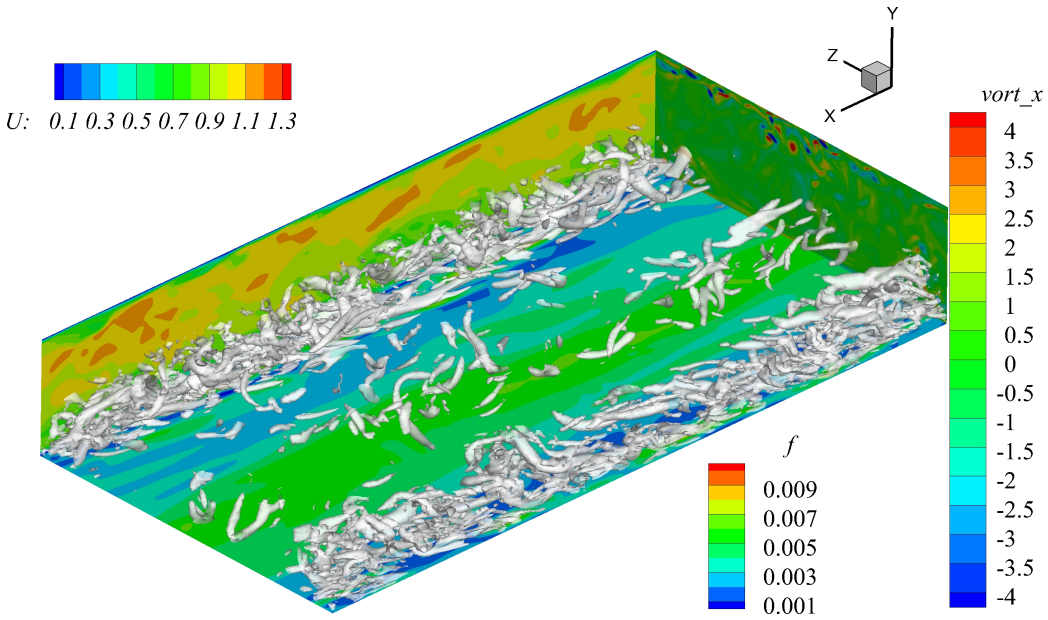

图 5.15　Plasma(Weak)涡结构

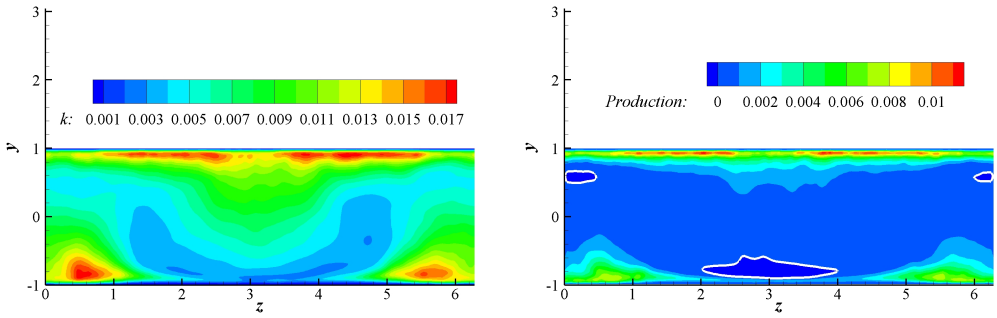

(a) 湍动能　　(b) 湍动能生成项

图 5.16　Plasma（Weak）湍动能和湍动能生成项

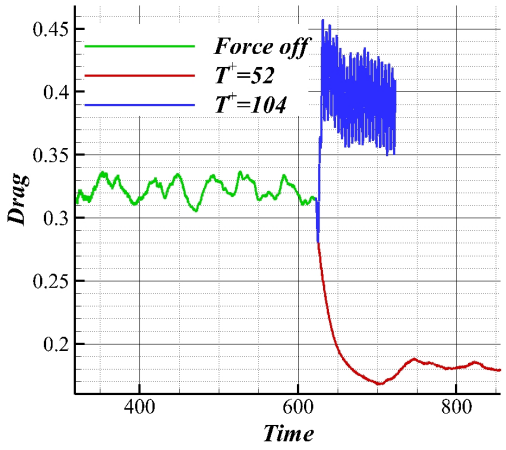

图 5.17　米兰理工体积力激励方案阻力变化

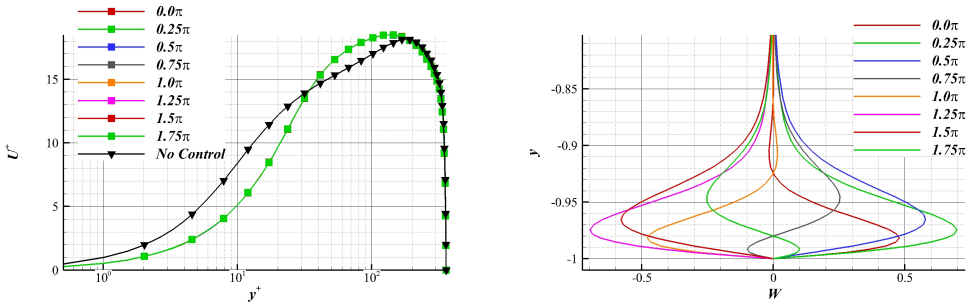

(a) U^+　　(b) W

图 5.18　$T^+ = 52$相平均

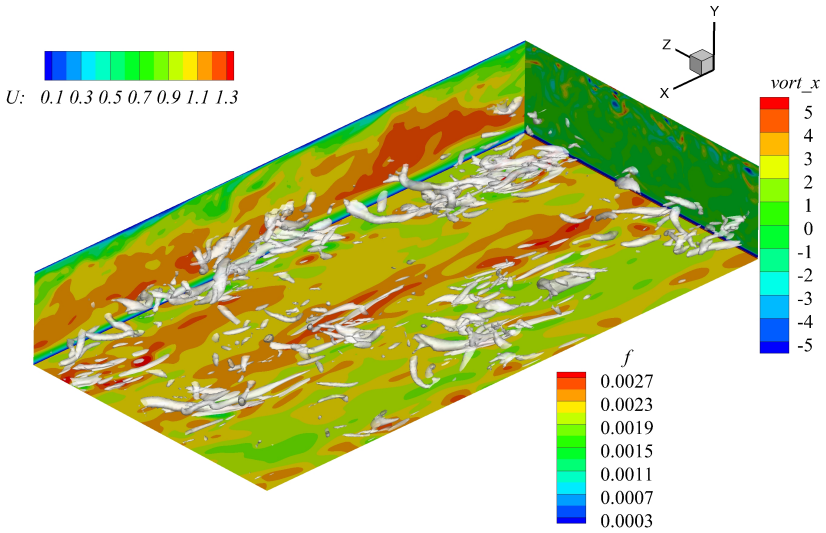

图 5.19　POLIMI涡结构图

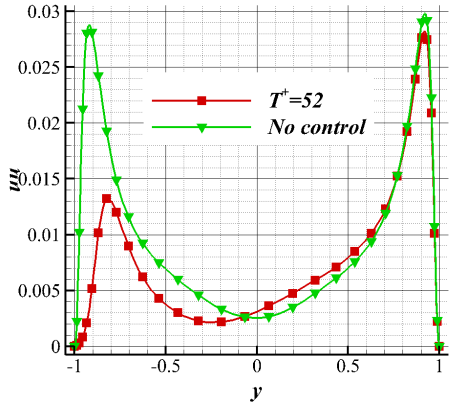

(a) < *uu* >

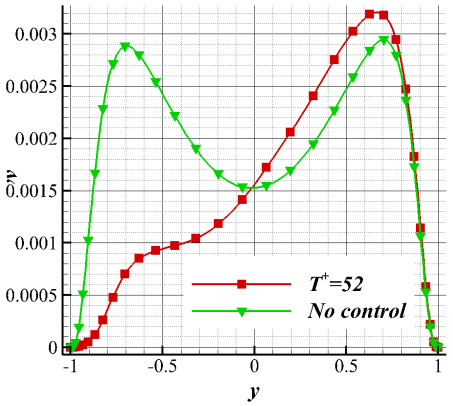

(b) < *vv* >

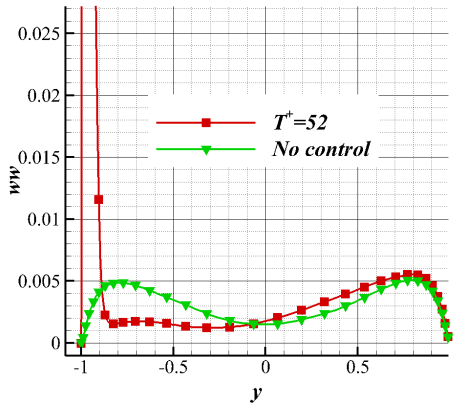

(c) < *ww* >

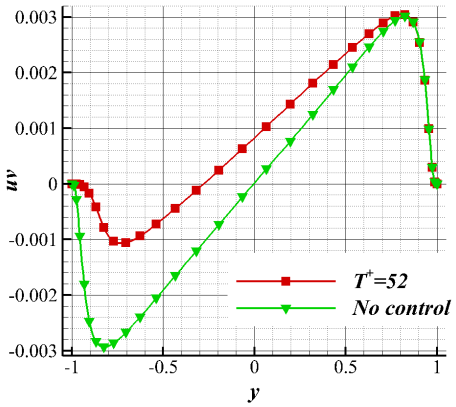

(d) < *uv* >

图 5.20　POLIMI二阶统计量对比

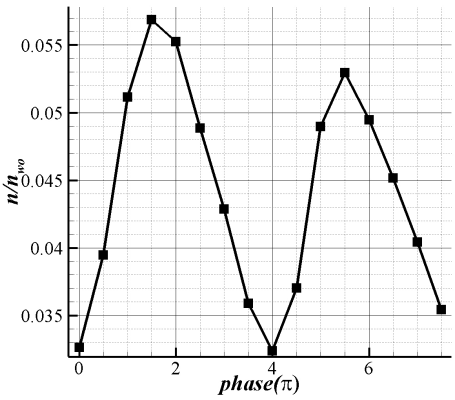

(a) POLIMI

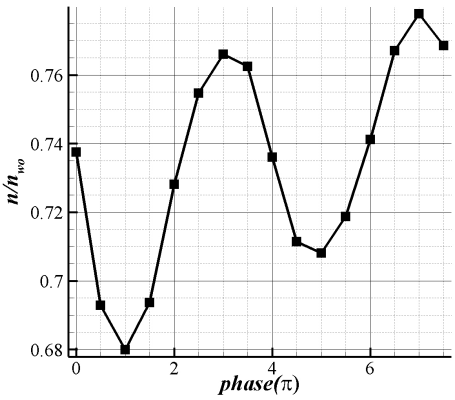

(b) 16DBD

图 5.21　不同相位探测到的涡个数

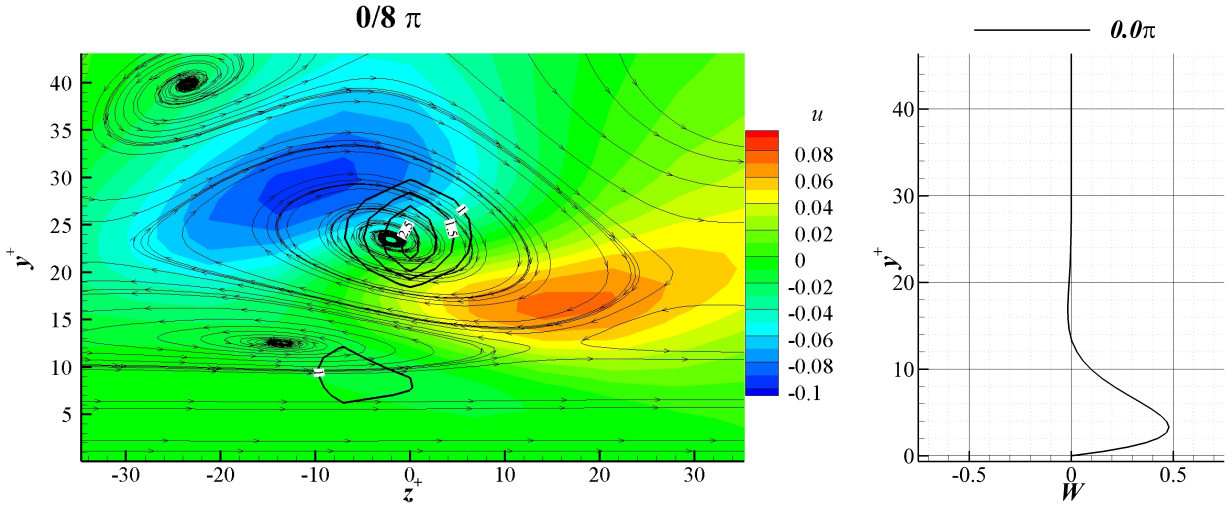

(a) 条件平均　　(b) 展向速度

图 5.22　POLIMI体积力分布0/16π相平均

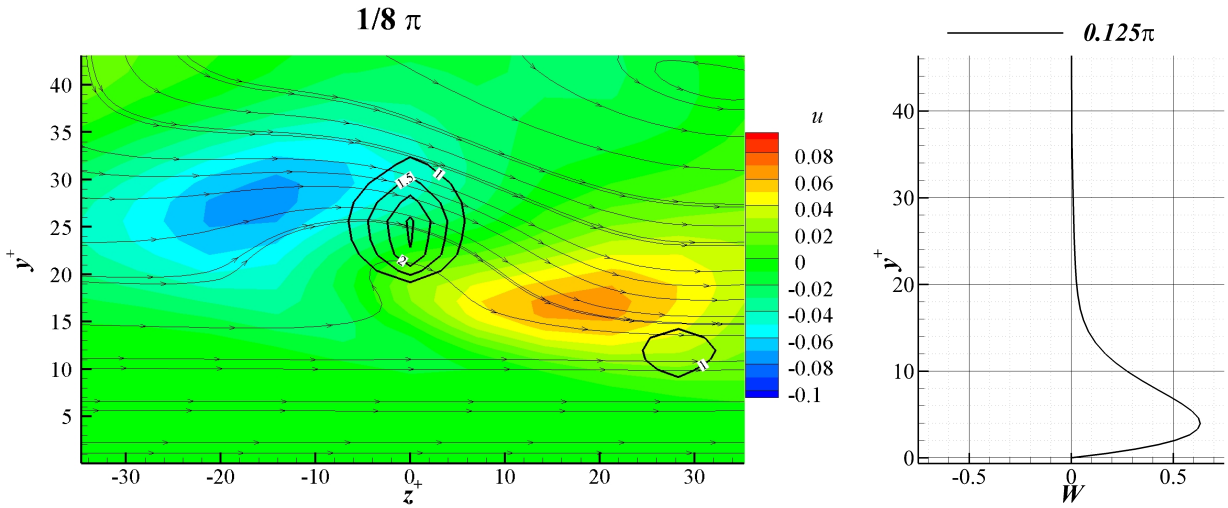

(a) 条件平均　　(b) 展向速度

图 5.23　POLIMI体积力分布1/16π相平均

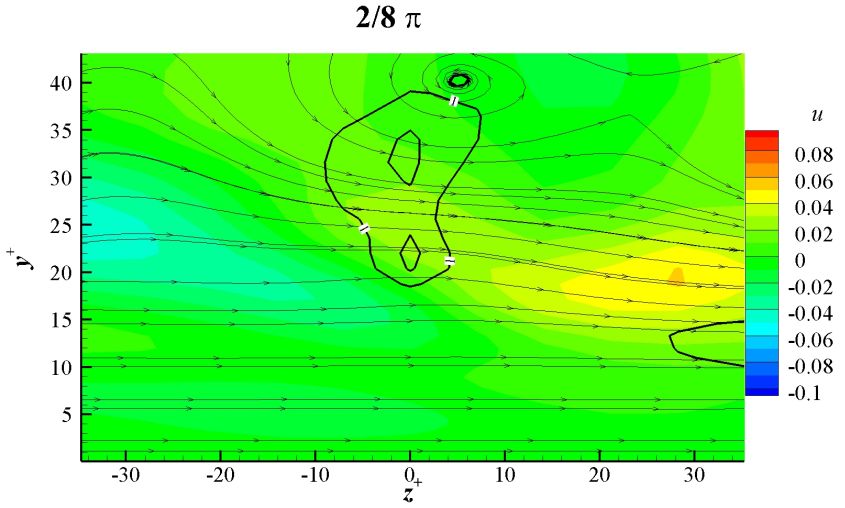

(a) 条件平均　　(b) 展向速度

图 5.24　POLIMI体积力分布2/16π相平均

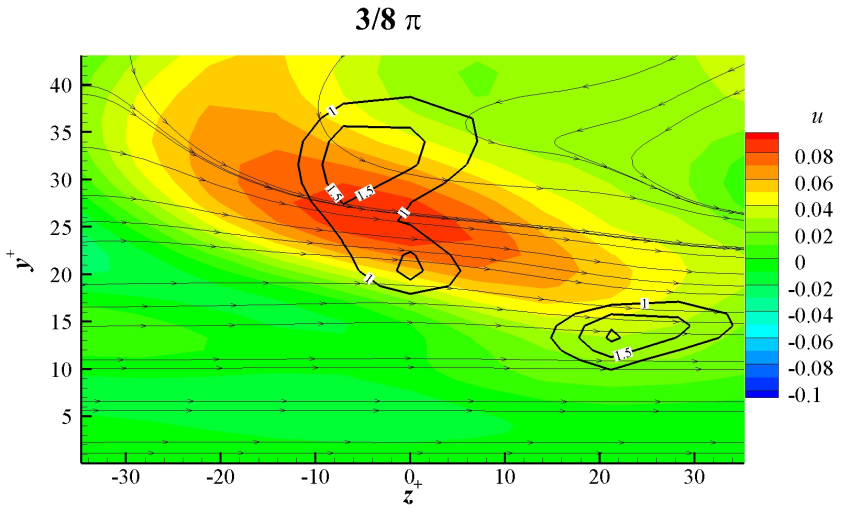

(a) 条件平均　　(b) 展向速度

图 5.25　POLIMI体积力分布3/16π相平均

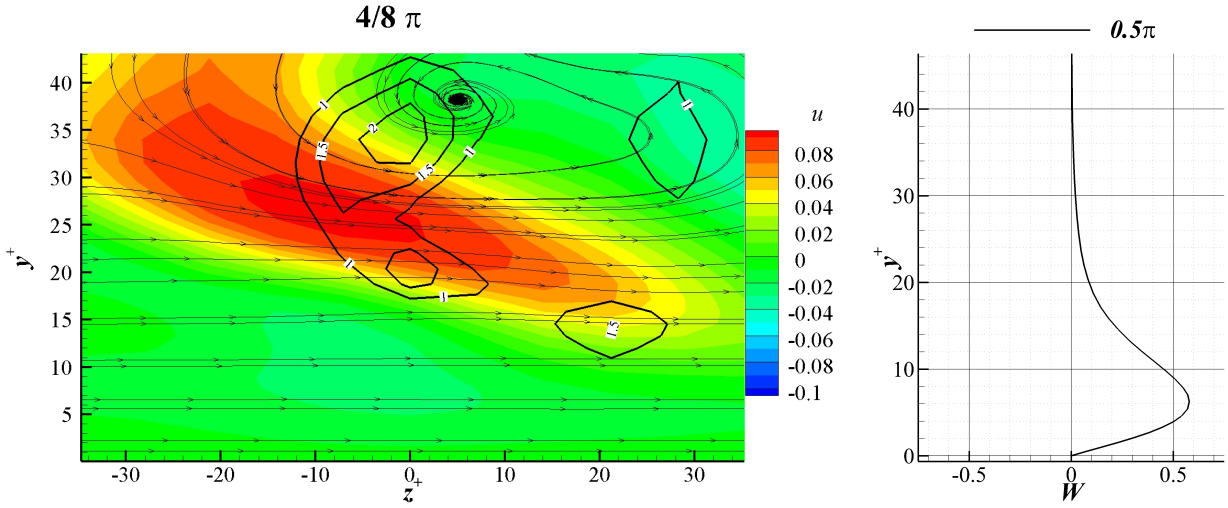

(a) 条件平均　　(b) 展向速度

图 5.26　POLIMI体积力分布4/16π相平均

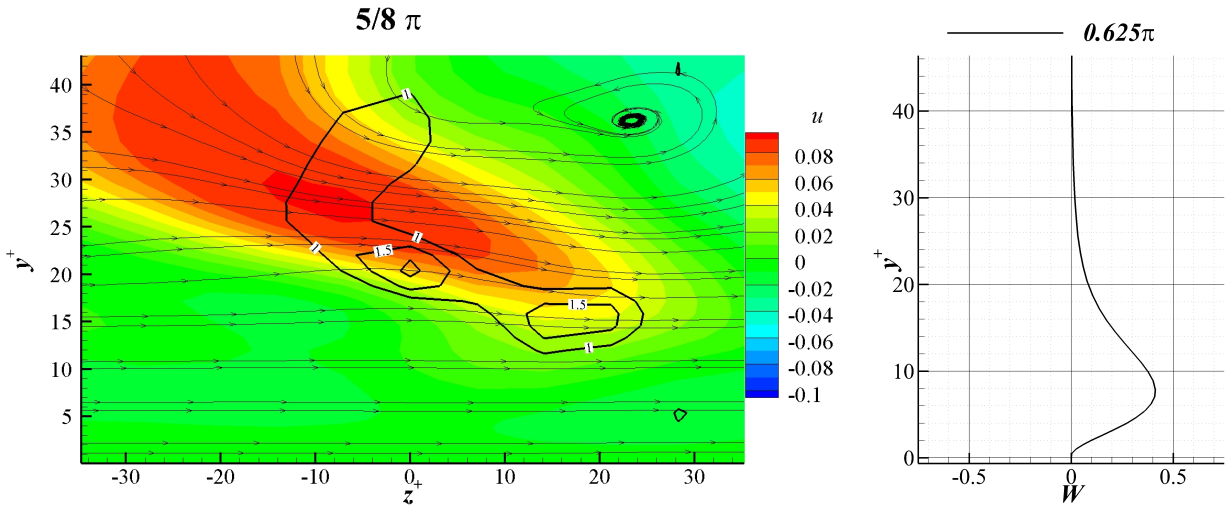

(a) 条件平均　　(b) 展向速度

图 5.27　POLIMI体积力分布5/16π相平均

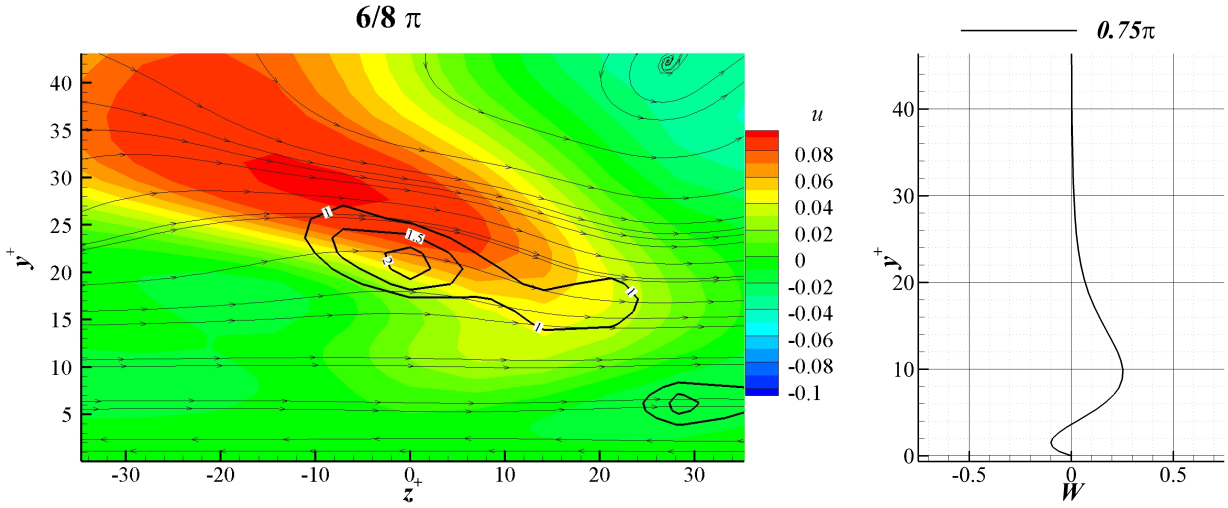

(a) 条件平均　　(b) 展向速度

图 5.28　POLIMI体积力分布6/16π相平均

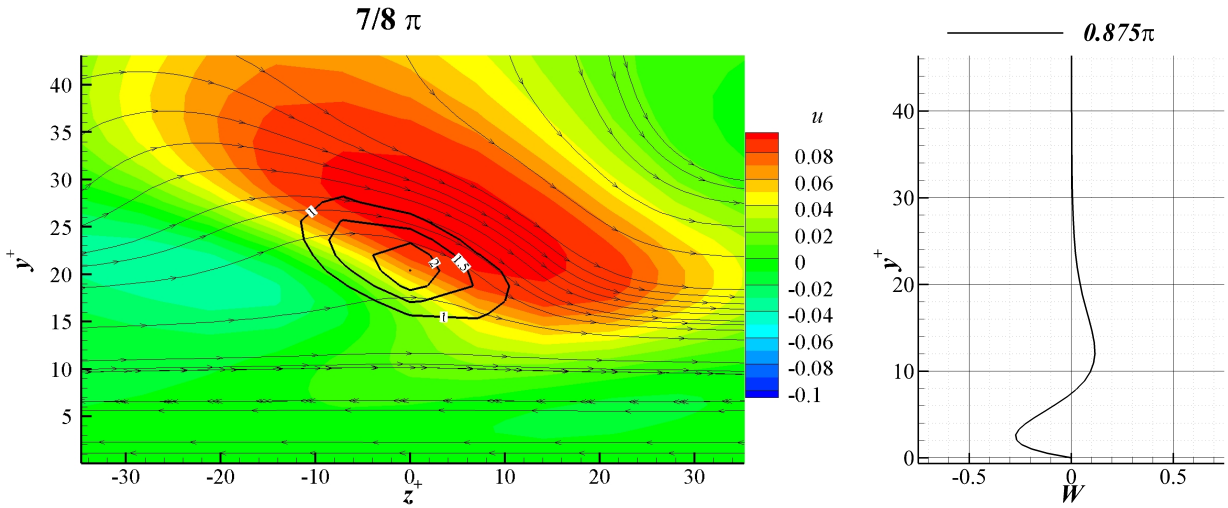

(a) 条件平均　　(b) 展向速度

图 5.29　POLIMI体积力分布7/16π相平均

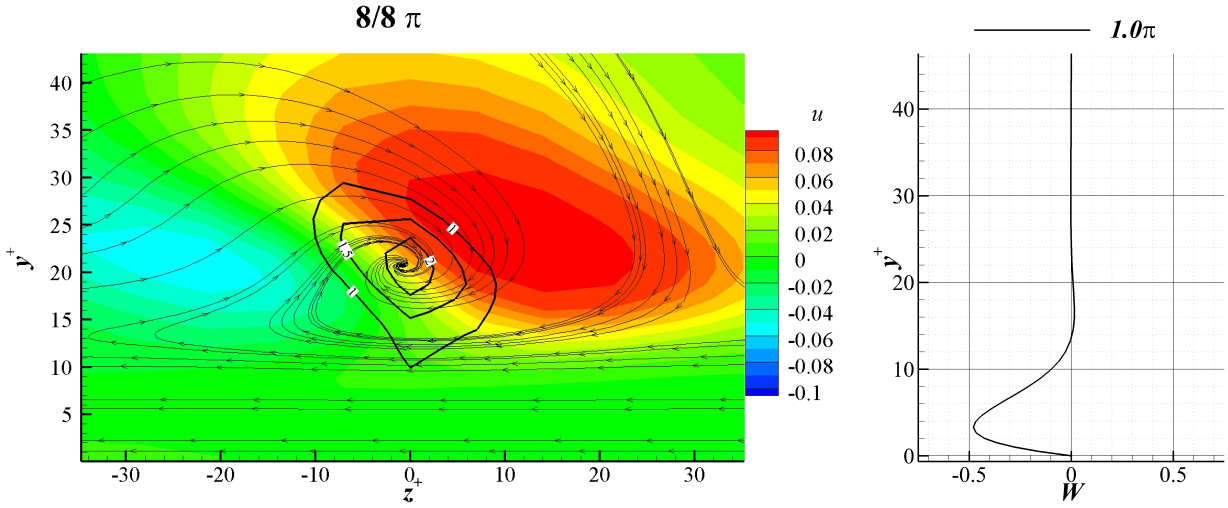

(a) 条件平均　　(b) 展向速度

图 5.30　POLIMI体积力分布8/16π相平均

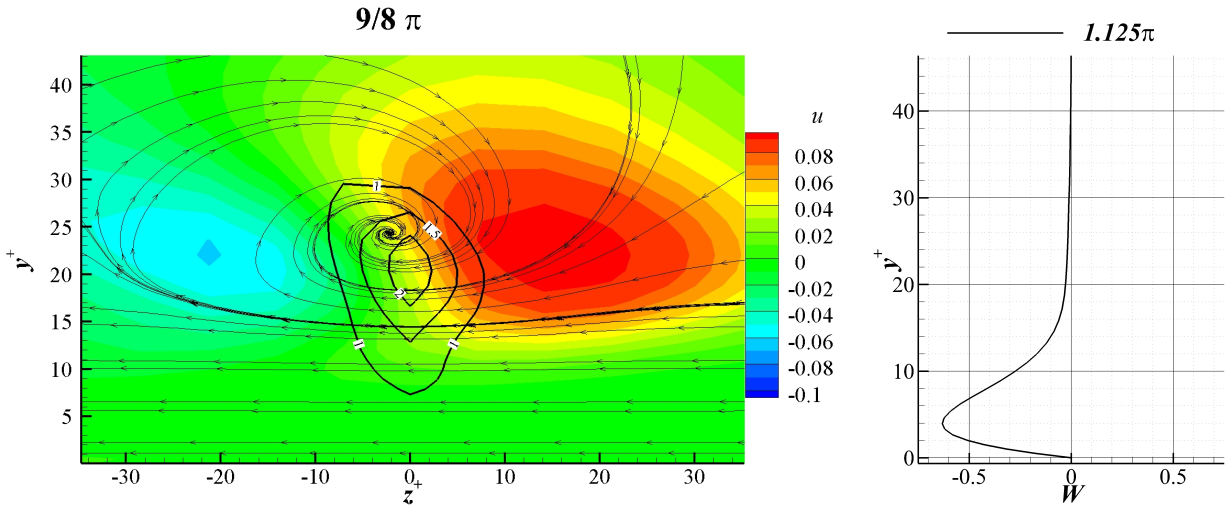

(a) 条件平均　　(b) 展向速度

图 5.31　POLIMI体积力分布9/16π相平均

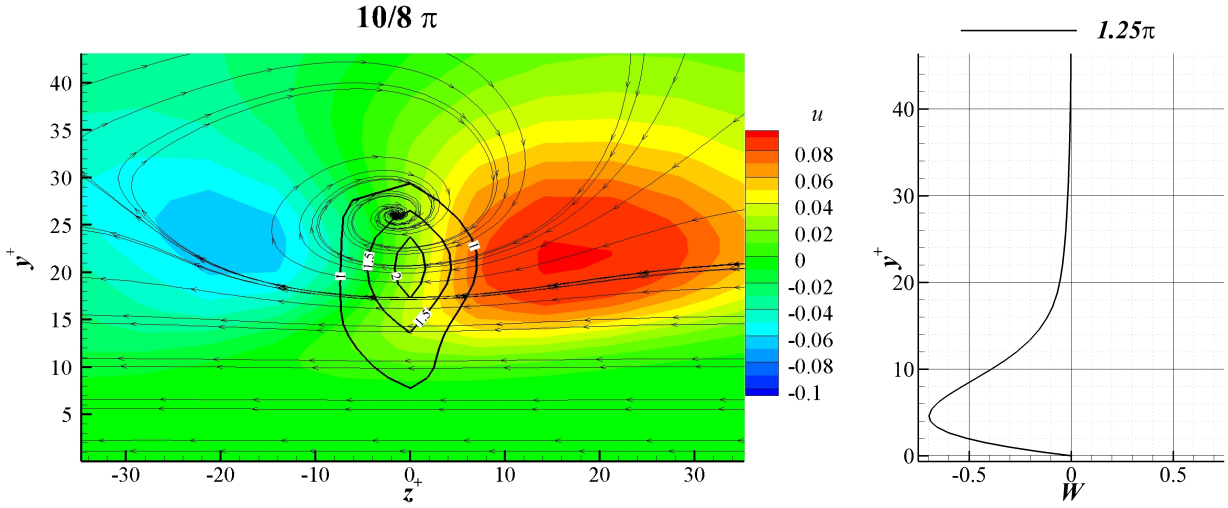

(a) 条件平均　　(b) 展向速度

图 5.32　POLIMI体积力分布10/16π相平均

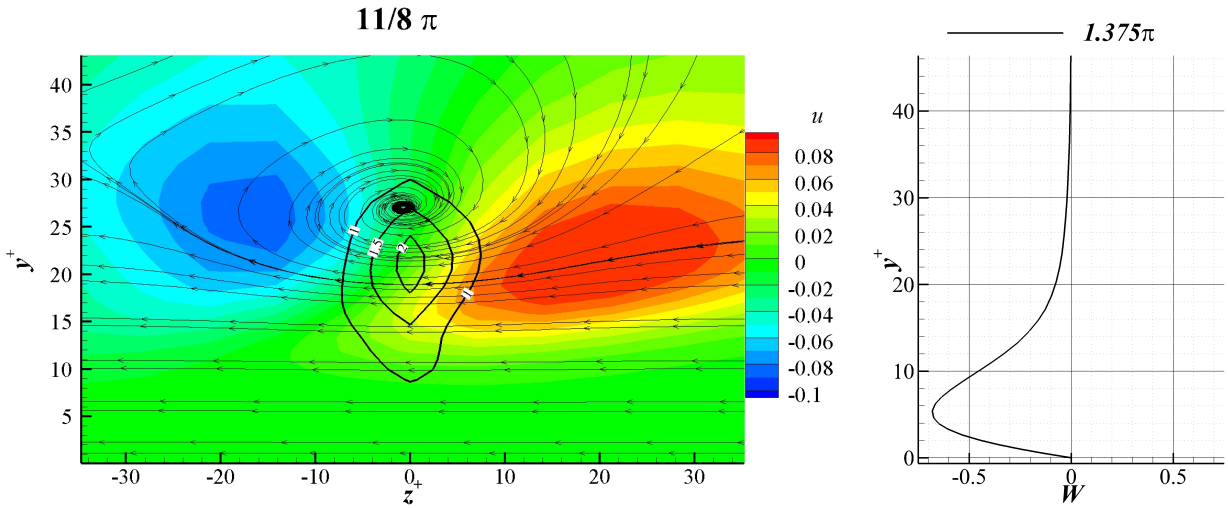

(a) 条件平均　　(b) 展向速度

图 5.33　POLIMI体积力分布11/16π相平均

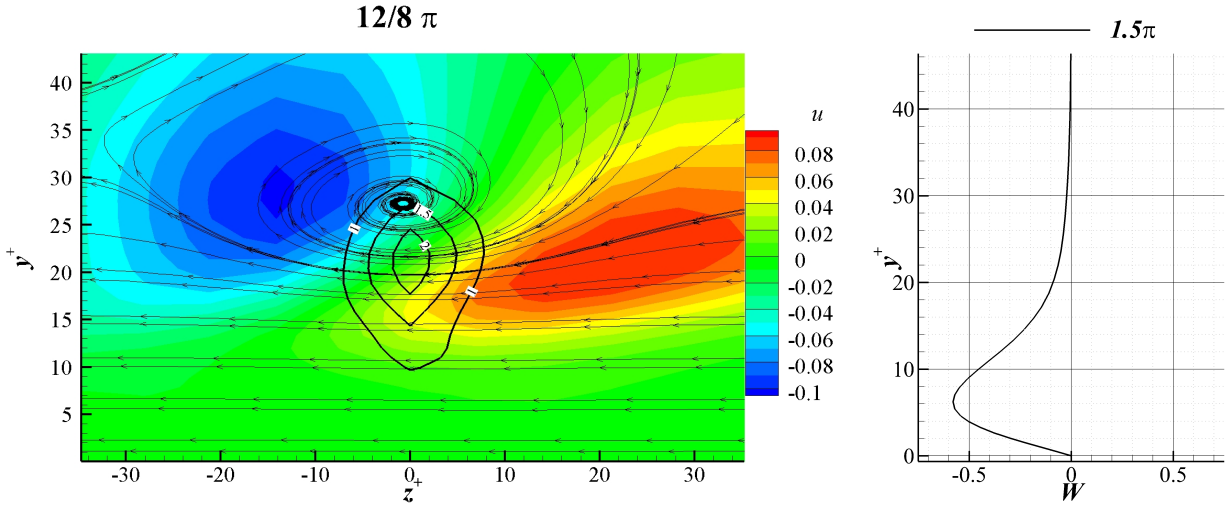

(a) 条件平均　　(b) 展向速度

图 5.34　POLIMI体积力分布12/16π相平均

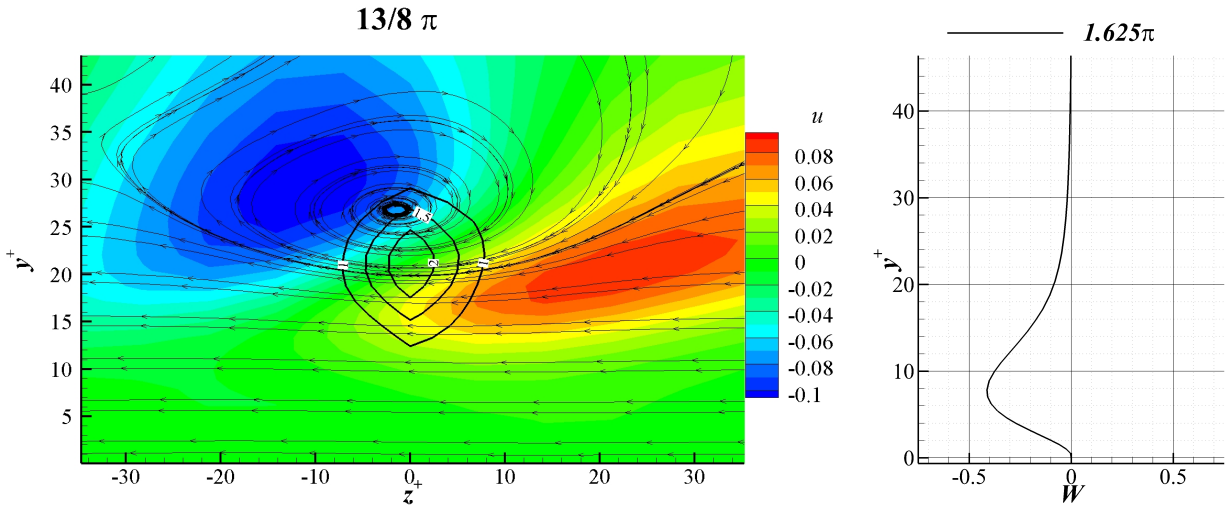

(a) 条件平均　　(b) 展向速度

图 5.35　POLIMI体积力分布13/16π相平均

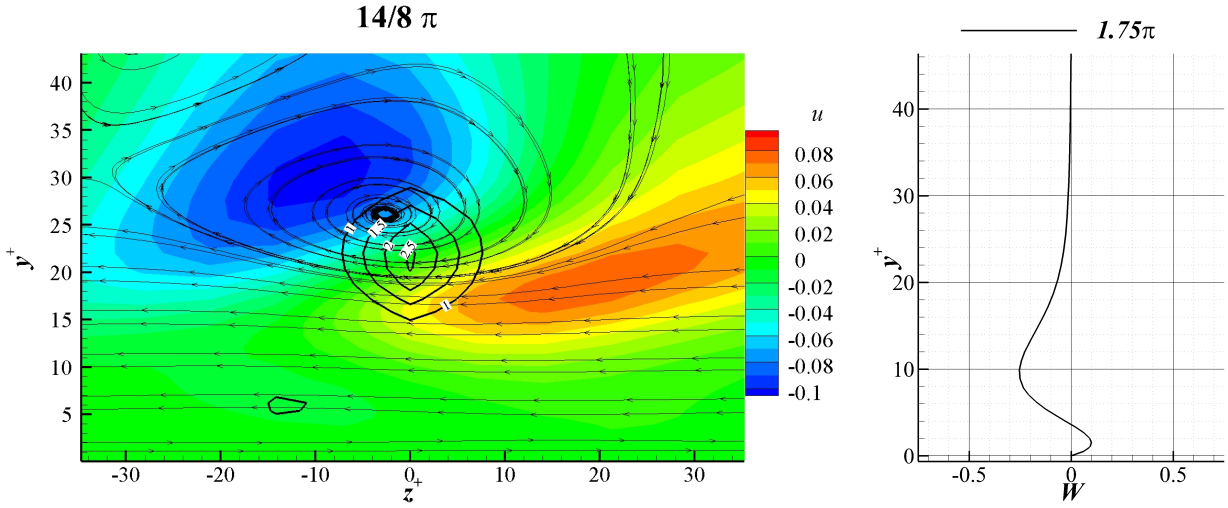

(a) 条件平均　　(b) 展向速度

图 5.36　POLIMI体积力分布14/16π相平均

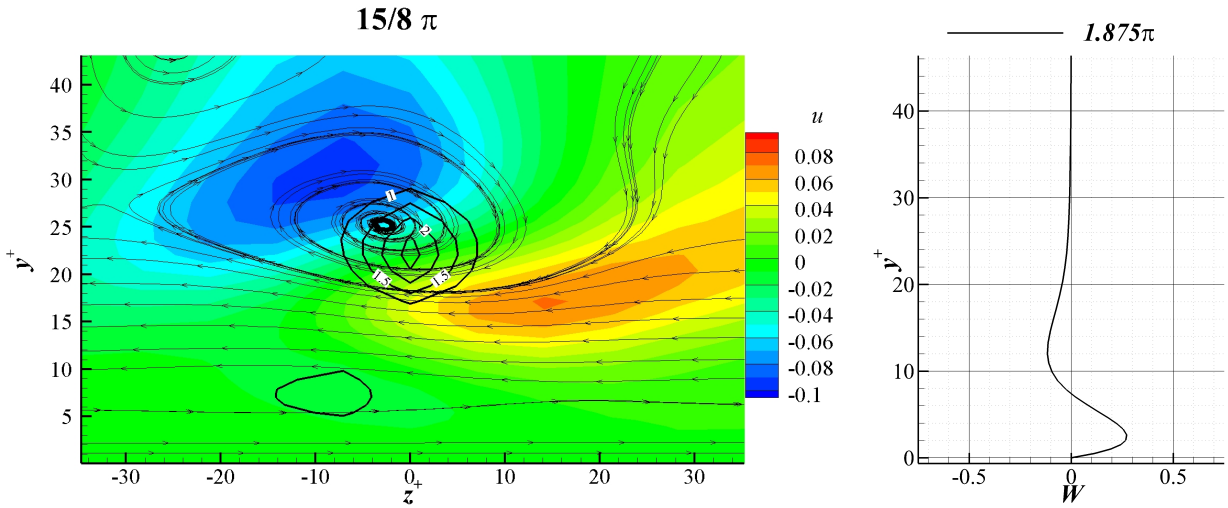

(a) 条件平均　　(b) 展向速度

图 5.37　POLIMI体积力分布15/16π相平均

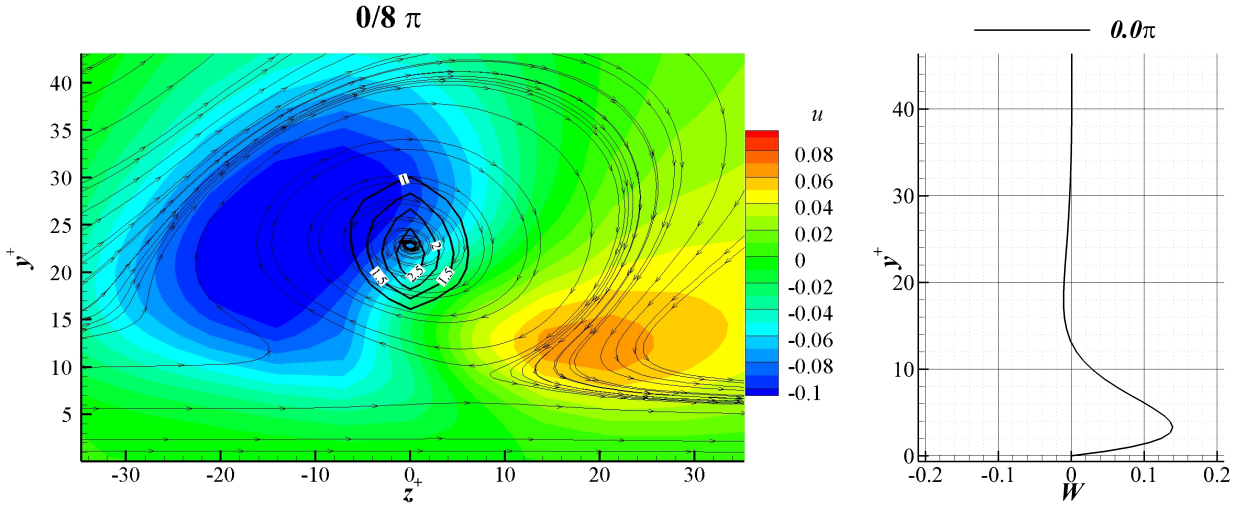

(a) 条件平均　　(b) 展向速度

图 5.38　16DBD体积力分布0/16π相平均

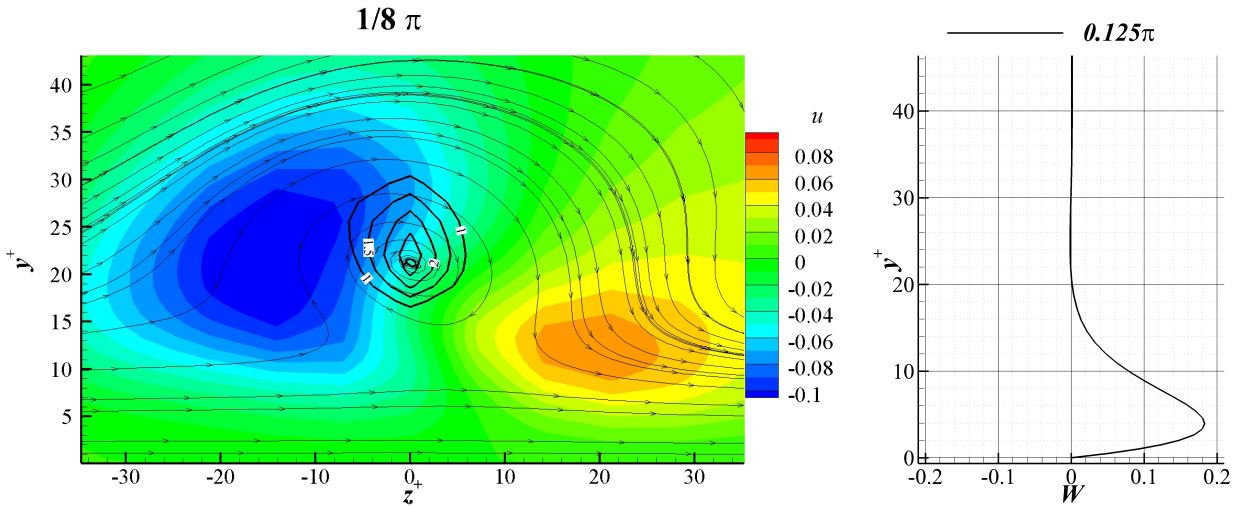

(a) 条件平均　　(b) 展向速度

图 5.39　16DBD体积力分布1/16π相平均

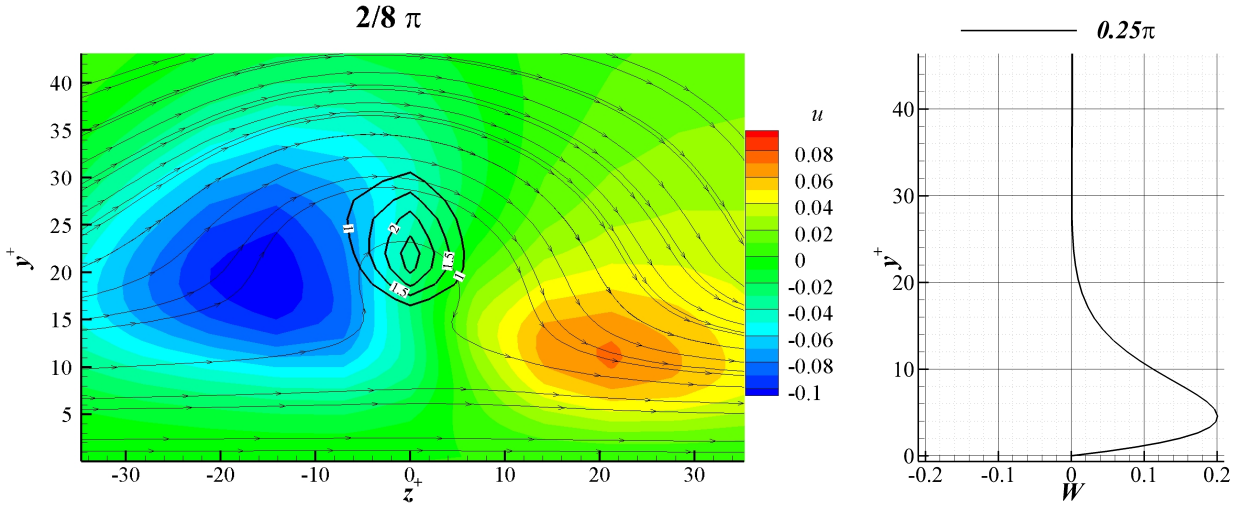

(a) 条件平均　　(b) 展向速度

图 5.40　16DBD体积力分布2/16π相平均

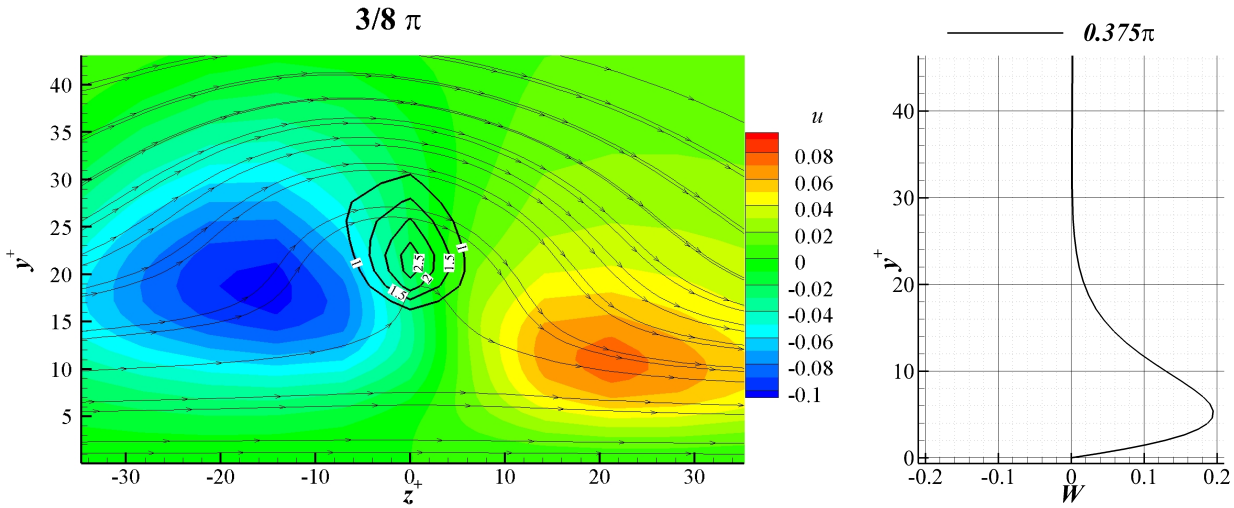

(a) 条件平均　　(b) 展向速度

图 5.41　16DBD体积力分布3/16π相平均

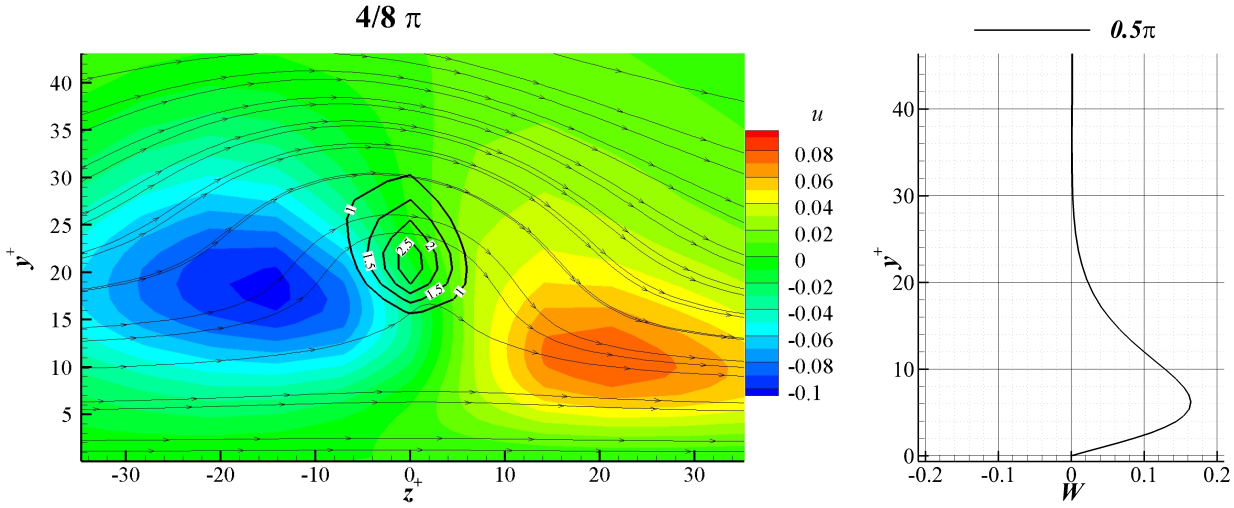

(a) 条件平均　　(b) 展向速度

图 5.42　16DBD体积力分布4/16π相平均

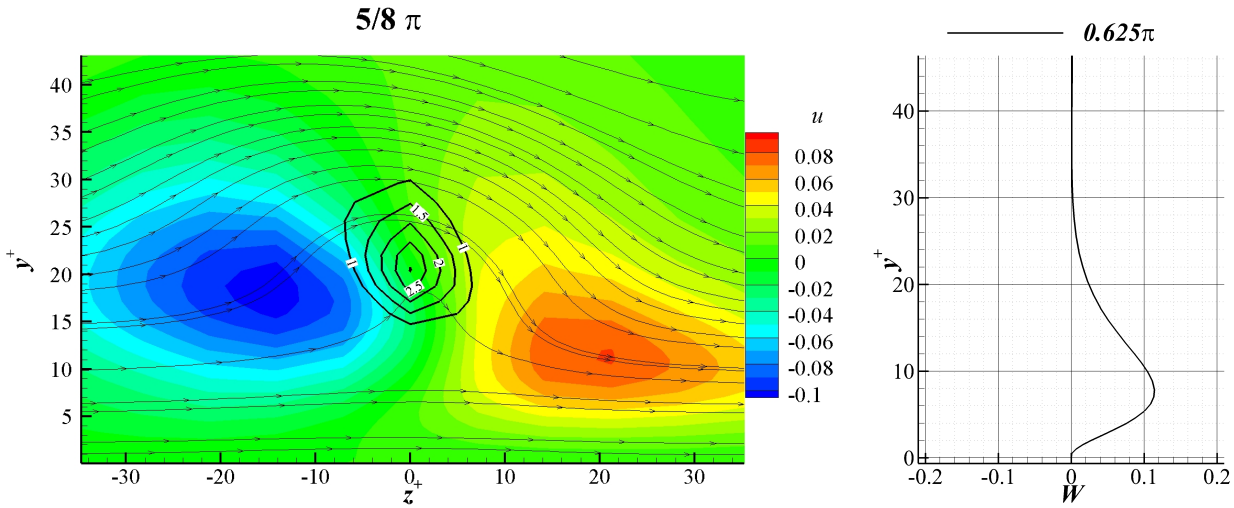

(a) 条件平均　　(b) 展向速度

图 5.43　16DBD体积力分布5/16π相平均

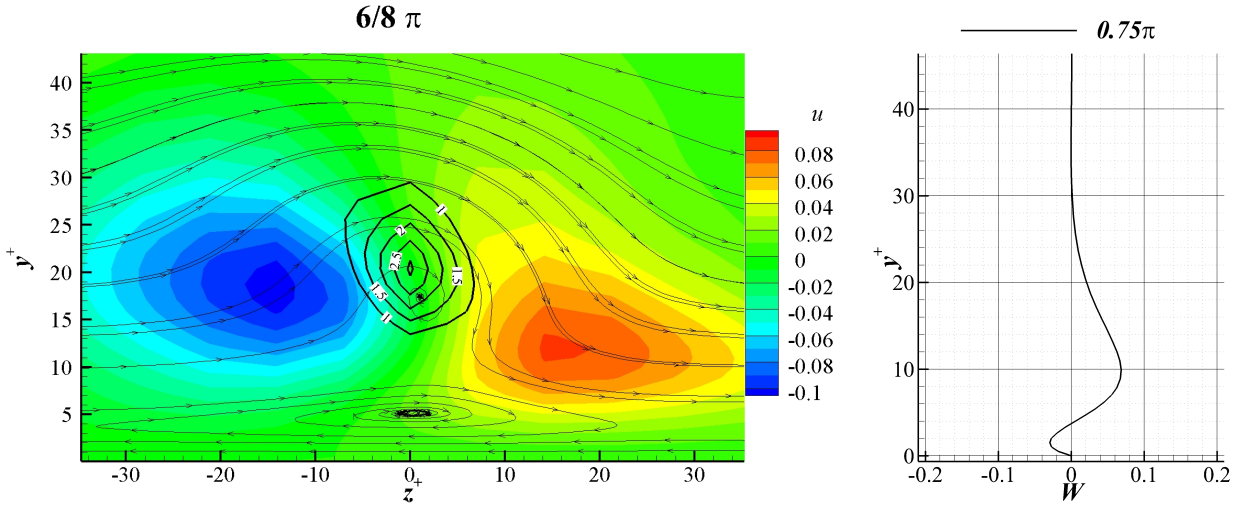

(a) 条件平均　　(b) 展向速度

图 5.44　16DBD体积力分布6/16π相平均

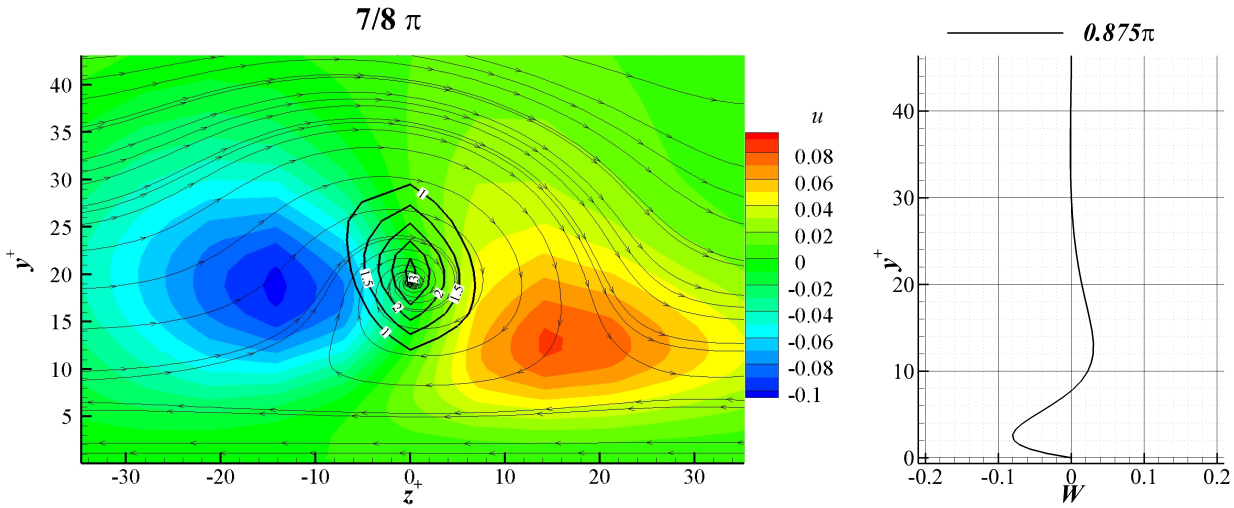

(a) 条件平均　　(b) 展向速度

图 5.45　16DBD体积力分布7/16π相平均

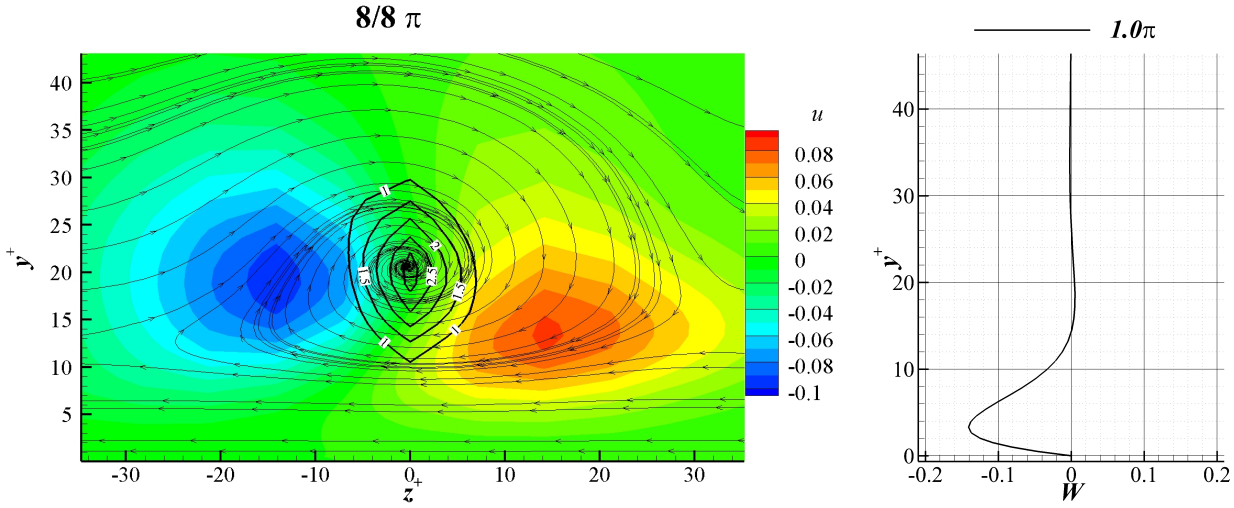

(a) 条件平均　　(b) 展向速度

图 5.46　16DBD体积力分布8/16π相平均

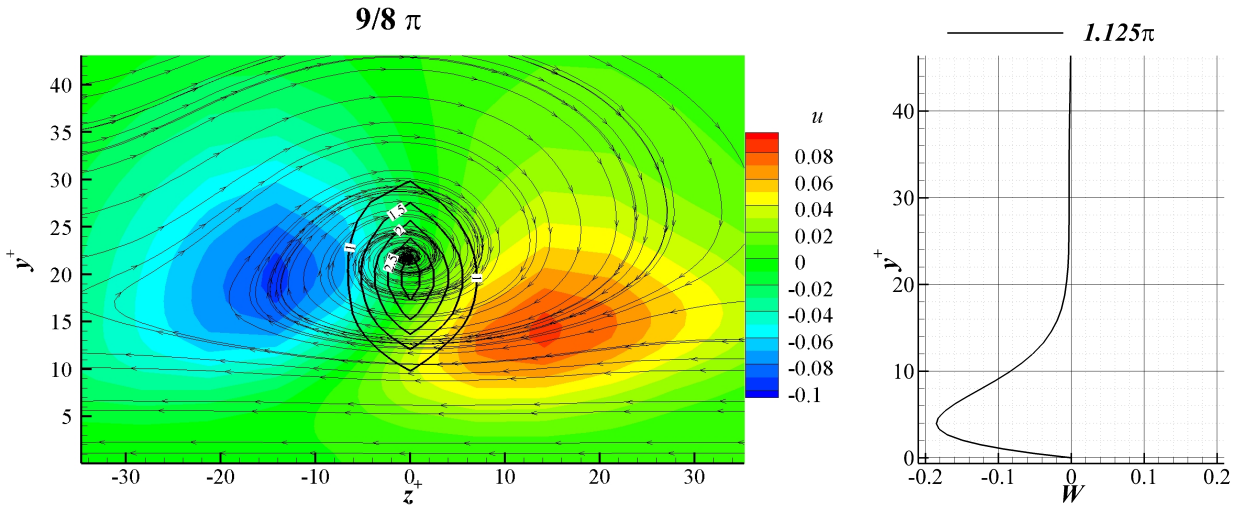

(a) 条件平均　　(b) 展向速度

图 5.47　16DBD体积力分布9/16π相平均

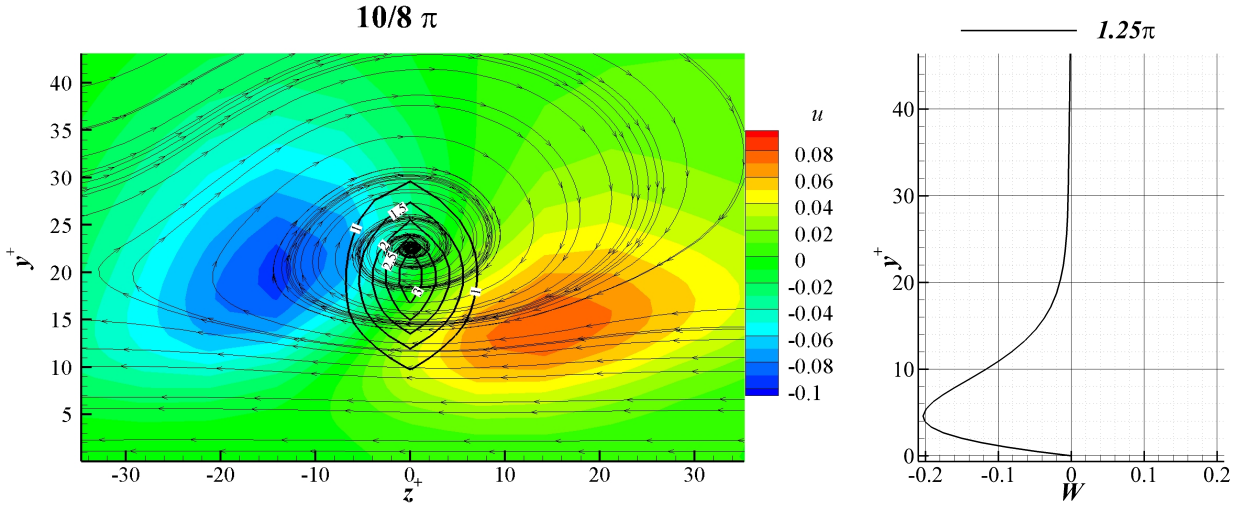

(a) 条件平均　　(b) 展向速度

图 5.48　16DBD体积力分布10/16π相平均

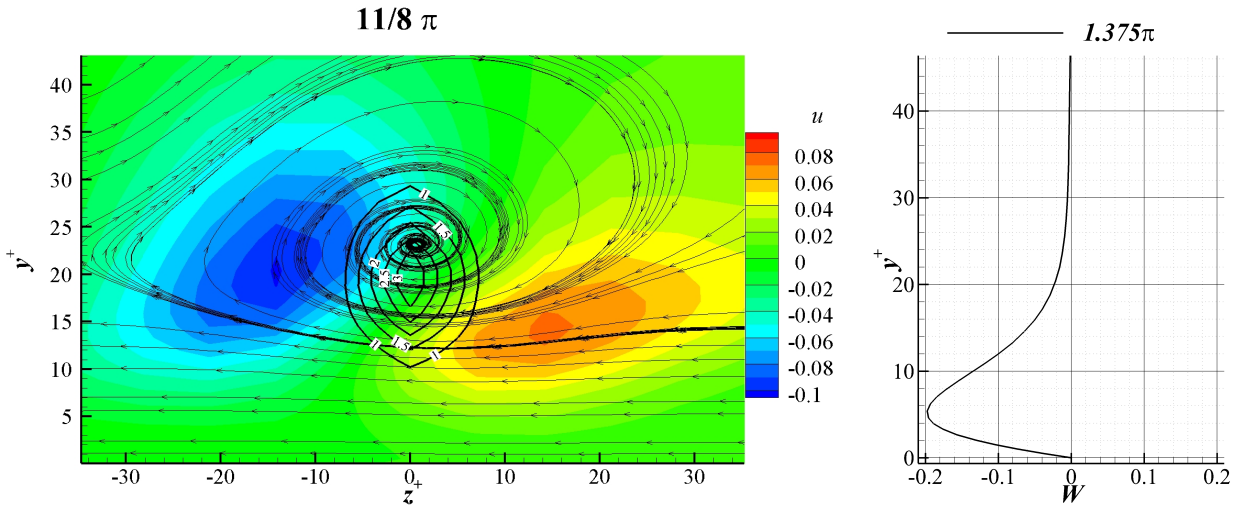

(a) 条件平均　　(b) 展向速度

图 5.49　16DBD体积力分布11/16π相平均

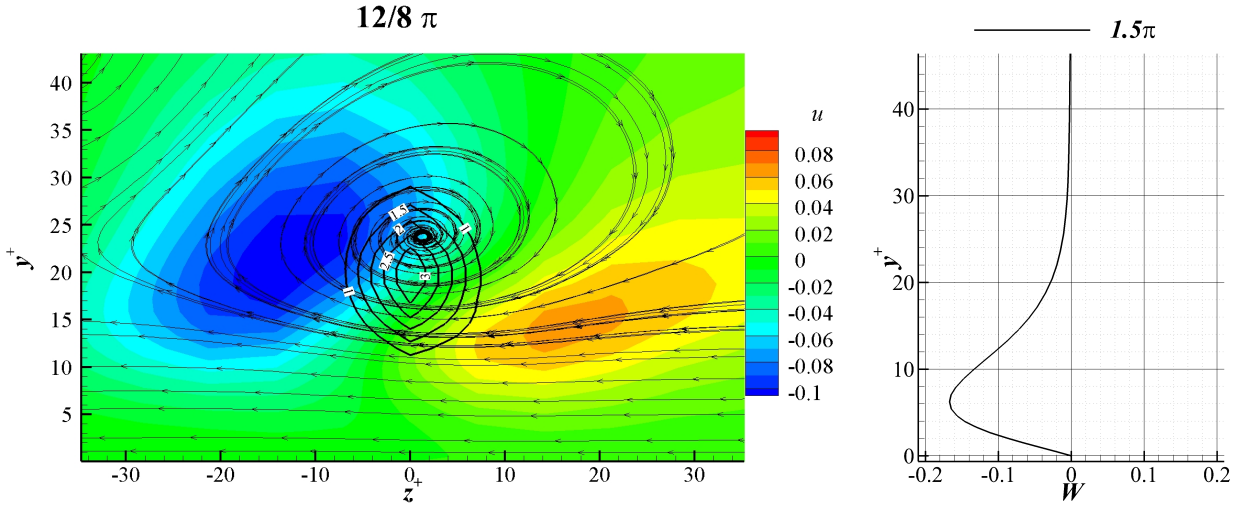

(a) 条件平均　　(b) 展向速度

图 5.50　16DBD体积力分布12/16π相平均

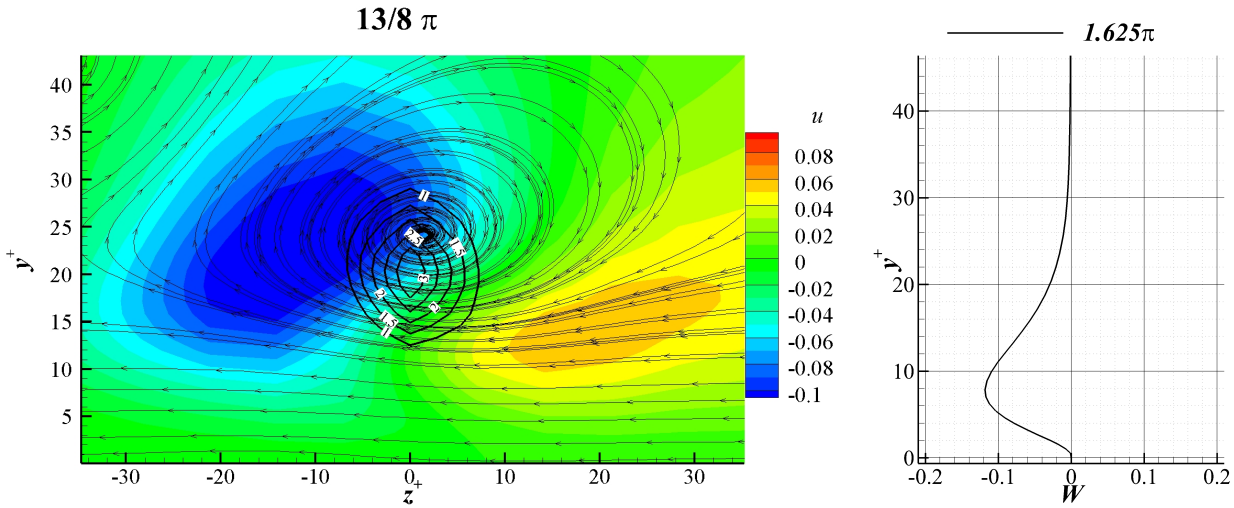

(a) 条件平均　　(b) 展向速度

图 5.51　16DBD体积力分布13/16π相平均

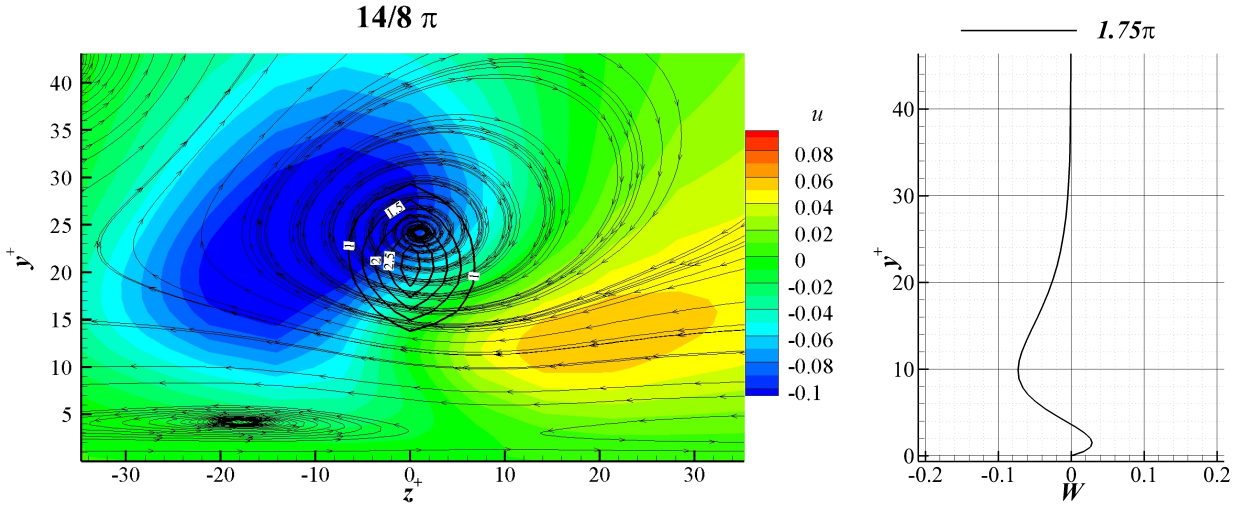

(a) 条件平均　　(b) 展向速度

图 5.52　16DBD体积力分布14/16π相平均

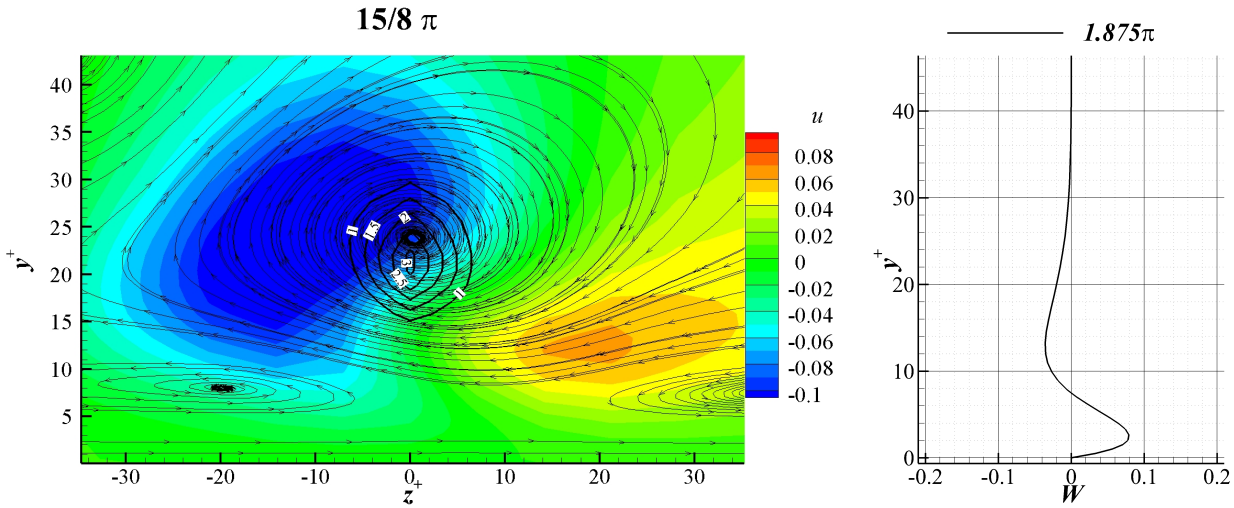

(a) 条件平均　　(b) 展向速度

图 5.53　16DBD体积力分布15/16π相平均

第6章　结论

参考文献

[1] 张谷令, 敖玲, 胡建芳, 等. 应用等离子体物理学[M]. [出版地不详]: 北京: 首都师范大学出版社, 2008.

[2] 聂万胜, 程钰锋, 车学科. 介质阻挡放电等离子体流动控制研究进展[J]. 力学进展, 2012, 42 (6): 722–734.

[3] 吴云, 李应红. 等离子体流动控制研究进展与展望[J]. 航空学报, 2015, 36(2): 381–405.

[4] Masuda S, Washizu M. Ionic charging of a very high resistivity spherical particle[J/OL]. Journal of Electrostatics, 1979, 6(1): 57–67. http://www.sciencedirect.com/science/article/pii/030438867990024X.

[5] Roth J, Sherman D, Wilkinson S. Aerospace sciences meetings: Boundary layer flow control with a one atmosphere uniform glow discharge surface plasma[M/OL]. American Institute of Aeronautics and Astronautics, 1998. https://doi.org/10.2514/6.1998-328

[6] Whalley R D, Choi K S. The starting vortex in quiescent air induced by dielectric-barrier-discharge plasma[J]. Journal of Fluid Mechanics, 2012, 703: 192–203.

[7] Malik M R, Li F, Choudhari M M, et al. Secondary instability of crossflow vortices and swept-wing boundary-layer transition[J]. Journal of Fluid Mechanics, 1999, 399: 85–115.

[8] Malik M, Li F, Chang C L. Crossflow disturbances in three-dimensional boundary layers: nonlinear development, wave interaction and secondary instability[J]. Journal of Fluid Mechanics, 1994, 268: 1–36.

[9] Li F, Malik M R. On the nature of PSE approximation[J]. Theoretical and Computational Fluid Dynamics, 1996, 8(4): 253–273.

[10] Bottaro A, Corbett P, Luchini P. The effect of base flow variation on flow stability[J]. Journal of Fluid Mechanics, 2003, 476.

[11] Marquet O, Sipp D, Jacquin L. Sensitivity analysis and passive control of cylinder flow[J]. Journal of Fluid Mechanics, 2008, 615: 221.

[12] Alizard F, Robinet J C, Rist U. Sensitivity analysis of a streamwise corner flow[J]. Physics of Fluids, 2010, 22(1): 014103.

[13] Brandt L, Sipp D, Pralits J O, et al. Effect of base-flow variation in noise amplifiers: the flat-plate boundary layer[J]. Journal of Fluid Mechanics, 2011, 687: 503–528.

[14] Meliga P, Pujals G, Serre E. Sensitivity of 2-d turbulent flow past a d-shaped cylinder using global stability[J]. Physics of Fluids, 2012, 24(6): 061701.

[15] Browne O M F, Rubio G, Ferrer E, et al. Sensitivity analysis to unsteady perturbations of complex flows: a discrete approach[J]. International Journal for Numerical Methods in Fluids, 2014, 76 (12): 1088–1110.

[16] Alizard F, Robinet J C, Filliard G. Sensitivity analysis of optimal transient growth for turbulent boundary layers[J]. European Journal of Mechanics - B/Fluids, 2015, 49: 373–386.

[17] Pralits J O, Airiau C, Hanifi A, et al. Sensitivity analysis using adjoint parabolized stability equations for compressible flows[J]. Flow, Turbulence and Combustion, 2000, 65(3-4): 321–346.

[18] Lin R S, Malik M R. On the stability of attachment-line boundary layers. part 1. the incompressible swept hiemenz flow[J]. Journal of Fluid Mechanics, 1996, 311.

[19] GuÈGan A, Schmid P J, Huerre P. Optimal energy growth and optimal control in swept hiemenz flow[J]. Journal of Fluid Mechanics, 2006, 566: 11.

[20] Li F, Choudhari M, Carpenter M, et al. Control of crossflow transition at high reynolds numbers using discrete roughness elements[J]. AIAA Journal, 2015: 1–14.

[21] Xu G, Xiao Z, Fu S. Analysis of the secondary instability of the incompressible flows over a swept wing[J]. Science China Physics, Mechanics and Astronomy, 2011, 54(4): 724–736.

[22] Xu G, Xiao Z, Fu S. Secondary instability control of compressible flow by suction for a swept wing[J]. Science China Physics, Mechanics and Astronomy, 2011, 54(11): 2040–2052.

[23] Ren J, Fu S. Competition of the multiple görtler modes in hypersonic boundary layer flows[J]. Science China Physics, Mechanics and Astronomy, 2014, 57(6): 1178–1193.

[24] Ren J, Fu S. Floquet analysis of fundamental, subharmonic and detuned secondary instabilities of görtler vortices[J]. Science China Physics, Mechanics and Astronomy, 2014, 57(3): 555–561.

[25] Ren J, Fu S. Study of the discrete spectrum in a mach 4.5 görtler flow[J]. Flow, Turbulence and Combustion, 2014, 94(2): 339–357.

[26] Ren J, Fu S. Secondary instabilities of görtler vortices in high-speed boundary layer flows[J]. Journal of Fluid Mechanics, 2015, 781: 388–421.

[27] Ren J, Fu S, Hanifi A. Stabilization of the hypersonic boundary layer by finite-amplitude streaks [J]. Physics of Fluids, 2016, 28(2): 024110.

[28] Kriegseis J, Schwarz C, Tropea C, et al. Velocity-information-based force-term estimation of dielectric-barrier discharge plasma actuators[J]. Journal of Physics D: Applied Physics, 2013, 46 (5): 055202.

[29] Dörr P C, Kloker M J. Transition control in a three-dimensional boundary layer by direct attenuation of nonlinear crossflow vortices using plasma actuators[J]. International Journal of Heat and Fluid Flow, 2016, 61: 449–465.

[30] Dörr P, Kloker M. Stabilisation of a three-dimensional boundary layer by base-flow manipulation using plasma actuators[J]. Journal of Physics D: Applied Physics, 2015, 48(28): 285205.

[31] Wang Z J, Gao H. A unifying lifting collocation penalty formulation including the discontinuous galerkin, spectral volume/difference methods for conservation laws on mixed grids[J]. Journal of Computational Physics, 2009, 228(21): 8161–8186.

[32] Reibert M S. Nonlinear stability, saturation, and transition in crossflow-dominated boundary layers[D]. [S.l.]: Arizona State University, 1996.

[33] Saric W S, Carpenter A L, Reed H L. Passive control of transition in three-dimensional boundary layers, with emphasis on discrete roughness elements[J/OL]. Philosophical Transactions of the Royal Society, Section A, 2011, 369(1940): 1352–64. http://www.ncbi.nlm.nih.gov/pubmed/21382818.

[34] Saric W, Carrillo R, Jr, Reibert M. Leading-edge roughness as a transition control mechanism [C]//36th AIAA Aerospace Sciences Meeting and Exhibit. [S.l.: s.n.], 1998: 781.

[35] 薛瑞尼. ThuThesis: 清华大学学位论文模板[EB/OL]. 2017. https://github.com/xueruini/thuthesis.

致　谢

衷心感谢导师符松教授和课题组内王亮助理研究员对本人的精心指导。他们的言传身教将使我终生受益。

同时衷心感谢徐国亮师兄，任杰师兄在流动稳定性方面的悉心指导，帮助我解决了不少问题。

感谢 LaTeX 和 ThuThesis[35]，帮我节省了不少时间。

声　明

本人郑重声明：所呈交的学位论文，是本人在导师指导下，独立进行研究工作所取得的成果。尽我所知，除文中已经注明引用的内容外，本学位论文的研究成果不包含任何他人享有著作权的内容。对本论文所涉及的研究工作做出贡献的其他个人和集体，均已在文中以明确方式标明。

签　名：_____ 日　期：_____

附录 A　边界层方程数值求解方法

在对边界层方程进行谱方法离散的时候，需要先将$\eta \in [0,+\infty]$映射到$\zeta \in [-1,1]$。本文采用的映射函数为：

$$\eta = \frac{a(1+\zeta)}{b-\zeta}, a = \frac{\eta_{\max}\eta_j}{\eta_{\max}-2\eta_j}, b = 1+\frac{2a}{\eta_{\max}} \tag{A-1}$$

这里j为法向网格点指标，计算中法向网格点分布采用：

$$\zeta_j = \cos(\frac{j\pi}{N}) \tag{A-2}$$

法向一共布置了N+1个网格点，其中$j=0$为壁面上的网格点。针对这一网格分布，法方向的微分离散可以采用Chebyshev微分矩阵：

$$D_{j,k} = \begin{cases} \frac{c_j(-1)^{j+k}}{c_k(\zeta_j-\zeta_k)}\left(\frac{\partial\zeta}{\partial\eta}\right)_j & j \neq k \\ \frac{-\zeta_k}{2(1-\zeta_k^2)}\left(\frac{\partial\zeta}{\partial\eta}\right)_j & 1 \leq j=k \leq N-1 \\ \frac{2N^2+1}{6}\left(\frac{\partial\zeta}{\partial\eta}\right)_j & j=k=0 \\ -\frac{2N^2+1}{6}\left(\frac{\partial\zeta}{\partial\eta}\right)_j & j=k=N \end{cases} \tag{A-3}$$

相应的，可以得到积分矩阵$I_{j,k}$，这里不再赘述，留给读者自行推导。借助边界层方程的抛物性，求解的时候可以从入口向下游推进。求解的时候流向指标小于当前求解位置流向指标，i,的物理量都是已经求得的。这里为了简洁，将要求的变量的流向指标略去，即$\Phi_{i,j} = \Phi_j$。其他位置的流向指标保留。采用如上所述的微分、积分矩阵，可以得到最终的离散形式为：

$$\Lambda_j - \Lambda_{j-1} + \sum I_{jk}\left[2\xi t_0 u_k + u_k\right] = \sum I_{jk}\left[2\xi\sum_{m=1}^{M} t_m u_{i-m,k} + u_k\right] \tag{A-4a}$$

$$2\xi u_j\sum_{m=1}^{M} t_m u_{i-m,j} + 2\xi t_0 u_j^2 + \Lambda_j\sum D_{jk}u_k - \sum\left(D_{jk}\hat{\mu}_k\sum D_{kl}u_l\right) + 2\tilde{\beta}T_j = 0 \tag{A-4b}$$

$$2\xi u_j \sum_{m=1}^{M} t_m w_{i-m,j} + 2\xi t_0 u_j w_j + \Lambda_j \sum D_{jk} w_k - \sum \left(D_{jk} \hat{\mu}_k \sum D_{kl} w_l \right) = 0 \quad \text{(A-4c)}$$

$$2\xi C_p u_j \sum_{m=1}^{M} t_m T_{i-m,j} + 2\xi C_p t_0 u_j T_j + \Lambda_j C_p \sum D_{jk} T_k - 2(\gamma-1) M^2 \tilde{\beta} T_j u_j -$$
$$(\gamma-1) M^2 \hat{\mu}_j \left[\left(\sum D_{jk} u_k \right)^2 + \left(\sum D_{jk} w_k \right)^2 \right] - \frac{1}{\mathrm{Pr}} \sum \left(D_{jk} \hat{k}_k \sum D_{kl} T_l \right) = 0 \quad \text{(A-4d)}$$

其中t_m为后差离散用到的系数。粘性系数与导热系数由Surtherland公式给出：

$$\hat{\mu} = \frac{T^{3/2}(C+1)}{(C+T)T} \Rightarrow \frac{d\hat{\mu}}{dT} = \frac{T^{-1/2}(C+1)[C-T]}{2(C+T)^2} \quad \text{(A-5a)}$$

$$\hat{k} = kT = \frac{T^{5/2}(C+1)}{(C+T)} \Rightarrow \frac{d\hat{k}}{dT} = \frac{T^{3/2}(C+1)[5C+3T]}{2(C+T)^2} \quad \text{(A-5b)}$$

其中C为公式中系数。$\mathbf{J}_b$矩阵中，各项的表达式为：

$$\mathbf{J}_b(4j-3, e) = \frac{\partial L_{dis}(\Phi)_{4j-3}}{\partial \Lambda_e} = \delta_{j,e} - \delta_{j-1,e}$$
$$\mathbf{J}_b(4j-2, e) = \frac{\partial L_{dis}(\Phi)_{4j-2}}{\partial \Lambda_e} = \delta_{j,e} \sum D_{jk} u_k$$
$$\mathbf{J}_b(4j-1, e) = \frac{\partial L_{dis}(\Phi)_{4j-1}}{\partial \Lambda_e} = \delta_{j,e} \sum D_{jk} w_k$$
$$\mathbf{J}_b(4j, e) = \frac{\partial L_{dis}(\Phi)_{4j}}{\partial \Lambda_e} = \delta_{j,e} c_p \sum D_{jk} T_k$$
$$\mathbf{J}_b(4j-3, e+N+1) = \frac{\partial L_{dis}(\Phi)_{4j-3}}{\partial u_e} = I_{je}[2\xi t_0 + 1]$$
$$\mathbf{J}_b(4j-2, e+N+1) = \frac{\partial L_{dis}(\Phi)_{4j-2}}{\partial u_e} = 2\xi \delta_{j,e} \sum_{m=1}^{M} t_m u_{i-m,j} + 4\xi t_0 u_j \delta_{j,e} + \Lambda_j D_{je} - \sum \left(D_{jk} \hat{\mu}_k D_{ke} \right)$$
$$\mathbf{J}_b(4j-1, e+N+1) = \frac{\partial L_{dis}(\Phi)_{4j-1}}{\partial u_e} = 2\xi \delta_{j,e} \sum_{m=0}^{M} t_m w_{i-m,j}$$
$$\mathbf{J}_b(4j, e+N+1) = \frac{\partial L_{dis}(\Phi)_{4j}}{\partial u_e}$$
$$= 2\xi c_p \delta_{j,e} \sum_{m=0}^{M} t_m T_{i-m,j} - 2(\gamma-1) M^2 \tilde{\beta} T_j \delta_{j,e} - 2(\gamma-1) M^2 \hat{\mu}_j \left(\sum D_{jk} u_k \right) D_{je}$$

$$\mathbf{J}_b(4j-3,e+2N+2)=\frac{\partial L_{dis}(\Phi)_{4j-3}}{\partial w_e}=0$$
$$\mathbf{J}_b(4j-2,e+2N+2)=\frac{\partial L_{dis}(\Phi)_{4j-2}}{\partial w_e}=0$$
$$\mathbf{J}_b(4j-2,e+2N+2)=\frac{\partial L_{dis}(\Phi)_{4j-2}}{\partial w_e}=0$$
$$\mathbf{J}_b(4j-1,e+2N+2)=\frac{\partial L_{dis}(\Phi)_{4j-1}}{\partial w_e}=2\xi t_0 u_j\delta_{j,e}+\Lambda_j D_{je}-\sum\left(D_{jk}\hat{\mu}_k D_{ke}\right)$$
$$\mathbf{J}_b(4j,e+2N+2)=\frac{\partial L_{dis}(\Phi)_{4j}}{\partial w_e}=-2(\gamma-1)M^2\hat{\mu}_j\left(\sum D_{jk}w_k\right)D_{je}$$
$$\mathbf{J}_b(4j-3,e+3N+3)=\frac{\partial L_{dis}(\Phi)_{4j-3}}{\partial T_e}=0$$
$$\mathbf{J}_b(4j-2,e+3N+3)=\frac{\partial L_{dis}(\Phi)_{4j-2}}{\partial T_e}=-\left(D_{je}\frac{d\hat{\mu}_e}{dT_e}\sum D_{el}u_l\right)+2\tilde{\beta}\delta_{j,e}$$
$$\mathbf{J}_b(4j-1,e+3N+3)=\frac{\partial L_{dis}(\Phi)_{4j-1}}{\partial T_e}=-\left(D_{je}\frac{d\hat{\mu}_e}{dT_e}\sum D_{el}w_l\right)$$
$$\begin{aligned}\mathbf{J}_b(4j,e+3N+3)&=\frac{\partial L_{dis}(\Phi)_{4j}}{\partial T_e}\\&=2\xi c_p t_0 u_j\delta_{j,e}+\Lambda_j c_p D_{je}-2(\gamma-1)M^2\tilde{\beta}\delta_{j,e}u_j\\&\quad-(\gamma-1)M^2\frac{d\hat{\mu}_e}{dT_e}\delta_{j,e}\left[\left(\sum D_{jk}u_k\right)^2+\left(\sum D_{jk}w_k\right)^2\right]\\&\quad-\frac{1}{\mathrm{Pr}}\left(D_{je}\frac{d\hat{k}_e}{dT_e}\sum D_{el}T_l\right)-\frac{1}{\mathrm{Pr}}\sum\left(D_{jk}\hat{k}_k D_{ke}\right)\end{aligned}$$

壁面边界条件：

$$L_{dis}(\Phi)_1=\Lambda_1;L_{dis}(\Phi)_2=u_1;L_{dis}(\Phi)_3=w_1;L_{dis}(\Phi)_4=\sum D_{1k}T_k;$$
$$\mathbf{J}_b(1,e)=\delta_{1,e};\mathbf{J}_b(2,e)=\delta_{N+2,e};\mathbf{J}_b(3,e)=\delta_{2N+3,e};$$
$$\mathbf{J}_b(4,e)=D_{1e},e\in[3N+4,4N+4]$$

远场边界条件：

$$L_{dis}(\Phi)_{4N+1}=\Lambda_{N+1}-\Lambda_N+\sum I_{N+1,k}\left[2\xi t_0u_k+u_k\right]-\sum I_{4N+1,k}\left[2\xi\sum_{m=1}^{M}t_m u_{i-m,k}+u_k\right]$$
$$L_{dis}(\Phi)_{4N+2}=u_{N+1}-u_e;L_{dis}(\Phi)_{4N+3}=w_{N+1}-w_e;L_{dis}(\Phi)_{4N+4}=T_{N+1}-T_e$$

$\mathbf{J}_b(4N+1,e)=\delta_{N+1,e}-\delta_{N,e}$; $\mathbf{J}_b(4N+1,e+N+1)=I_{N+1,e}\left[2\xi t_0+1\right]$

$\mathbf{J}_b(4N+2,e+N+1)=\delta_{N+1,e}$;

$\mathbf{J}_b(4N+3,e+2N+2)=\delta_{N+1,e}$; $\mathbf{J}_b(4N+4,e+3N+3)=\delta_{N+1,e}$;

附录 B　扰动方程具体形式

方程2-19中各项系数的具体形式将在这里给出：

$$\mathbf{\Gamma}=\begin{bmatrix} 1 & 0 & 0 & 0 & 0 \\ 0 & \rho & 0 & 0 & 0 \\ 0 & 0 & \rho & 0 & 0 \\ 0 & 0 & 0 & \rho & 0 \\ -\frac{\gamma-1}{\gamma}T & 0 & 0 & 0 & \rho-\frac{\gamma-1}{\gamma}\rho \end{bmatrix}$$

A矩阵的各个分矢量和各个分量的表达形式如下（其他矩阵的分向量和分量的表达形式类似，这里不再赘述。）：

$$\mathbf{A}=\begin{bmatrix} \mathbf{A}_1 \\ \mathbf{A}_2 \\ \mathbf{A}_3 \\ \mathbf{A}_4 \\ \mathbf{A}_5 \end{bmatrix}=\begin{bmatrix} \mathbf{A}_{11} & \mathbf{A}_{12} & \mathbf{A}_{13} & \mathbf{A}_{14} & \mathbf{A}_{15} \\ \mathbf{A}_{21} & \mathbf{A}_{22} & \mathbf{A}_{23} & \mathbf{A}_{24} & \mathbf{A}_{25} \\ \mathbf{A}_{31} & \mathbf{A}_{32} & \mathbf{A}_{33} & \mathbf{A}_{34} & \mathbf{A}_{35} \\ \mathbf{A}_{41} & \mathbf{A}_{42} & \mathbf{A}_{43} & \mathbf{A}_{44} & \mathbf{A}_{45} \\ \mathbf{A}_{51} & \mathbf{A}_{52} & \mathbf{A}_{53} & \mathbf{A}_{54} & \mathbf{A}_{55} \end{bmatrix}$$

$$\mathbf{A}_1=\begin{bmatrix} \frac{u}{h_1} & \frac{\rho}{h_1} & 0 & 0 & 0 \end{bmatrix}$$

$$\mathbf{A}_2=\begin{bmatrix} \frac{1}{\gamma \mathrm{Ma}^2}\frac{1}{h_1}T \\ \rho\frac{u}{h_1}-\frac{1}{h_1}\frac{4}{3}\frac{d\mu}{dT}\frac{\partial T}{\partial x}\frac{1}{\mathrm{Re}}\frac{1}{h_1} \\ -\frac{1}{h_1}\frac{\mu}{\mathrm{Re}}\frac{4}{3}\frac{1}{h_1}\frac{\partial h_1}{\partial y}-\frac{1}{h_1}\frac{d\mu}{dT}\frac{\partial T}{\partial y}\frac{1}{\mathrm{Re}}-\frac{\mu}{\mathrm{Re}}\frac{1}{h_1}\frac{\partial h_1}{\partial y}\frac{1}{h_1} \\ 0 \\ -\frac{1}{h_1}\frac{d\mu}{dT}\frac{1}{\mathrm{Re}}\left(\frac{4}{3}\frac{1}{h_1}\frac{\partial u}{\partial x}+\frac{4}{3}\frac{v}{h_1}\frac{\partial h_1}{\partial y}-\frac{2}{3}\frac{\partial v}{\partial y}\right)+\frac{1}{\gamma \mathrm{Ma}^2}\frac{1}{h_1}\rho \end{bmatrix}^T$$

$$\mathbf{A}_3 = \begin{bmatrix} 0 \\ \frac{1}{h_1}\frac{1}{\mathrm{Re}}\mu\frac{1}{h_1}\frac{\partial h_1}{\partial y} + \frac{2}{h_1}\frac{\partial h_1}{\partial y}\frac{1}{\mathrm{Re}}\mu\frac{1}{h_1} + \frac{2}{3}\frac{1}{\mathrm{Re}}\frac{d\mu}{dT}\frac{\partial T}{\partial y}\frac{1}{h_1} - \frac{2}{3}\frac{\mu}{\mathrm{Re}}\frac{1}{h_1}\frac{1}{h_1}\frac{\partial h_1}{\partial y} \\ \rho\frac{u}{h_1} - \frac{1}{h_1}\frac{1}{\mathrm{Re}}\frac{d\mu}{dT}\frac{\partial T}{\partial x}\frac{1}{h_1} \\ 0 \\ -\frac{1}{h_1}\frac{1}{\mathrm{Re}}\frac{d\mu}{dT}\left(\frac{\partial u}{\partial y} + \frac{1}{h_1}\frac{\partial v}{\partial x} - \frac{u}{h_1}\frac{\partial h_1}{\partial y}\right) \end{bmatrix}^T$$

$$\mathbf{A}_4 = \begin{bmatrix} 0 & 0 & 0 & \rho\frac{u}{h_1} - \frac{1}{h_1}\frac{d\mu}{dT}\frac{\partial T}{\partial x}\frac{1}{\mathrm{Re}}\frac{1}{h_1} & -\frac{1}{h_1}\frac{d\mu}{dT}\frac{1}{\mathrm{Re}}\frac{1}{h_1}\frac{\partial w}{\partial x} \end{bmatrix}$$

$$\begin{aligned}
\mathbf{A}_{51} =& -\frac{\gamma-1}{\gamma}T\frac{u}{h_1} \\
\mathbf{A}_{52} =& 2\times\frac{2}{3}\frac{(\gamma-1)\,\mathrm{Ma}^2}{\mathrm{Re}}\mu\left(\frac{1}{h_1}\frac{\partial v}{\partial y} - \frac{2}{h_1}\frac{1}{h_1}\frac{\partial u}{\partial x} - 2\frac{1}{h_1}\frac{v}{h_1}\frac{\partial h_1}{\partial y}\right) \\
\mathbf{A}_{53} =& -2\frac{(\gamma-1)\,\mathrm{Ma}^2}{\mathrm{Re}}\mu\left(\frac{1}{h_1}\frac{1}{h_1}\frac{\partial v}{\partial x} + \frac{1}{h_1}\frac{\partial u}{\partial y} - \frac{1}{h_1}\frac{1}{h_1}u\frac{\partial h_1}{\partial y}\right) \\
\mathbf{A}_{54} =& -2\frac{(\gamma-1)\,\mathrm{Ma}^2}{\mathrm{Re}}\mu\frac{1}{h_1}\frac{1}{h_1}\frac{\partial w}{\partial x} \\
\mathbf{A}_{55} =& \rho\frac{u}{h_1} - \frac{\gamma-1}{\gamma}\rho\frac{u}{h_1} - \frac{2}{\mathrm{Re}\,\mathrm{Pr}}\frac{1}{h_1}\frac{1}{h_1}\frac{d\kappa}{dT}\frac{\partial T}{\partial x}
\end{aligned}$$

$$\mathbf{B}_1 = \begin{bmatrix} v & 0 & \rho & 0 & 0 \end{bmatrix}$$

$$\mathbf{B}_2 = \begin{bmatrix} 0 \\ \rho v - \frac{d\mu}{dT}\frac{\partial T}{\partial y}\frac{1}{\mathrm{Re}} - \frac{\mu}{\mathrm{Re}}\frac{1}{h_1}\frac{\partial h_1}{\partial y} \\ \frac{2}{3}\frac{d\mu}{dT}\frac{\partial T}{\partial x}\frac{1}{\mathrm{Re}}\frac{1}{h_1} \\ 0 \\ -\frac{1}{h_1}\frac{d\mu}{dT}\frac{1}{\mathrm{Re}}\left(h_1\frac{\partial u}{\partial y} + \frac{\partial v}{\partial x} - u\frac{\partial h_1}{\partial y}\right) \end{bmatrix}^T$$

$$\mathbf{B}_3 = \begin{bmatrix} \frac{T}{\gamma \mathrm{Ma}^2} \\ -\frac{1}{h_1}\frac{1}{\mathrm{Re}}\frac{d\mu}{dT}\frac{\partial T}{\partial x} \\ \rho v - \frac{2}{h_1}\frac{\partial h_1}{\partial y}\frac{1}{\mathrm{Re}}\mu - \frac{4}{3}\frac{1}{\mathrm{Re}}\frac{d\mu}{dT}\frac{\partial T}{\partial y} + \frac{2}{3}\frac{\mu}{\mathrm{Re}}\frac{1}{h_1}\frac{\partial h_1}{\partial y} \\ 0 \\ \frac{\rho}{\gamma \mathrm{Ma}^2} + \frac{1}{\mathrm{Re}}\frac{d\mu}{dT}\left(\frac{2}{3}\frac{1}{h_1}\frac{\partial u}{\partial x} + \frac{2}{3}\frac{v}{h_1}\frac{\partial h_1}{\partial y} - \frac{4}{3}\frac{\partial v}{\partial y}\right) \end{bmatrix}^T$$

$$\mathbf{B}_4 = \begin{bmatrix} 0 & 0 & 0 & \rho v - \frac{1}{h_1}\frac{\partial h_1}{\partial y}\frac{1}{\mathrm{Re}}\mu - \frac{1}{\mathrm{Re}}\frac{d\mu}{dT}\frac{\partial T}{\partial y} & -\frac{1}{\mathrm{Re}}\frac{d\mu}{dT}\frac{\partial w}{\partial y} \end{bmatrix}$$

$$\begin{aligned}
\mathbf{B}_{51} &= -\frac{\gamma - 1}{\gamma} T v \\
\mathbf{B}_{52} &= -2\frac{(\gamma - 1)\,\mathrm{Ma}^2}{\mathrm{Re}}\mu\left(\frac{\partial u}{\partial y} + \frac{1}{h_1}\frac{\partial v}{\partial x} - \frac{1}{h_1}u\frac{\partial h_1}{\partial y}\right) \\
\mathbf{B}_{53} &= \frac{4}{3}\frac{(\gamma - 1)\,\mathrm{Ma}^2}{\mathrm{Re}}\mu\left(-2\frac{\partial v}{\partial y} + \frac{1}{h_1}\frac{\partial u}{\partial x} + \frac{v}{h_1}\frac{\partial h_1}{\partial y}\right) \\
\mathbf{B}_{54} &= -2\frac{(\gamma - 1)\,\mathrm{Ma}^2}{\mathrm{Re}}\mu\frac{\partial w}{\partial y} \\
\mathbf{B}_{55} &= \frac{1}{\gamma}\rho v - \frac{2}{\mathrm{Re}\,\mathrm{Pr}}\frac{d\kappa}{dT}\frac{\partial T}{\partial y} - \frac{1}{\mathrm{Re}\,\mathrm{Pr}}\frac{1}{h_1}\frac{\partial h_1}{\partial y}\kappa
\end{aligned}$$

$$\mathbf{C}_1 = \begin{bmatrix} w & 0 & 0 & \rho & 0 \end{bmatrix}$$

$$\mathbf{C}_2 = \begin{bmatrix} 0 \\ \rho w \\ 0 \\ \frac{2}{3}\frac{1}{h_1}\frac{d\mu}{dT}\frac{\partial T}{\partial x}\frac{1}{\mathrm{Re}} \\ -\frac{1}{h_1}\frac{d\mu}{dT}\frac{1}{\mathrm{Re}}\frac{\partial w}{\partial x} \end{bmatrix}^T$$

$$\mathbf{C}_3 = \begin{bmatrix} 0 & 0 & \rho w & \frac{2}{3}\frac{1}{\mathrm{Re}}\frac{d\mu}{dT}\frac{\partial T}{\partial y} & -\frac{d\mu}{dT}\frac{1}{\mathrm{Re}}\frac{\partial w}{\partial y} \end{bmatrix}$$

$$\mathbf{C}_4 = \begin{bmatrix} \frac{1}{\gamma \mathrm{Ma}^2} T \\ -\frac{1}{h_1}\frac{d\mu}{dT}\frac{\partial T}{\partial x}\frac{1}{\mathrm{Re}} \\ \frac{2}{3}\mu\frac{1}{\mathrm{Re}}\frac{1}{h_1}\frac{\partial h_1}{\partial y} - \frac{1}{\mathrm{Re}}\frac{d\mu}{dT}\frac{\partial T}{\partial y} - \frac{1}{h_1}\frac{\partial h_1}{\partial y}\frac{1}{\mathrm{Re}}\mu \\ \rho w \\ \frac{1}{\gamma \mathrm{Ma}^2}\rho - \frac{\partial \mu}{\partial T}\left(-\frac{2}{3}\frac{1}{\mathrm{Re}}\frac{1}{h_1}\frac{\partial u}{\partial x} - \frac{2}{3}\frac{1}{\mathrm{Re}}\frac{v}{h_1}\frac{\partial h_1}{\partial y} - \frac{2}{3}\frac{1}{\mathrm{Re}}\frac{\partial v}{\partial y}\right) \end{bmatrix}^T$$

$$\begin{aligned}
\mathbf{C}_{51} =& -\frac{\gamma-1}{\gamma} T w \\
\mathbf{C}_{52} =& -2\frac{(\gamma-1)\,\mathrm{Ma}^2}{\mathrm{Re}}\mu\frac{1}{h_1}\frac{\partial w}{\partial x} \\
\mathbf{C}_{53} =& -2\frac{(\gamma-1)\,\mathrm{Ma}^2}{\mathrm{Re}}\mu\frac{\partial w}{\partial y} \\
\mathbf{C}_{54} =& \frac{4}{3}\frac{(\gamma-1)\,\mathrm{Ma}^2}{\mathrm{Re}}\mu\left(\frac{1}{h_1}\frac{\partial u}{\partial x} + \frac{v}{h_1}\frac{\partial h_1}{\partial y} + \frac{\partial v}{\partial y}\right) \\
\mathbf{C}_{55} =& \frac{\rho w}{\gamma}
\end{aligned}$$

$$\mathbf{D}_1 = \begin{bmatrix} \frac{1}{h_1}\frac{\partial u}{\partial x} + \frac{\partial v}{\partial y} + \frac{\partial h_1}{\partial y}\frac{v}{h_1} & \frac{1}{h_1}\frac{\partial \rho}{\partial x} & \frac{\partial \rho}{\partial y} + \frac{\partial h_1}{\partial y}\frac{\rho}{h_1} & 0 & 0 \end{bmatrix}$$

$$\mathbf{D}_2 = \begin{bmatrix} \frac{u}{h_1}\frac{\partial u}{\partial x} + v\frac{\partial u}{\partial y} + \frac{uv}{h_1}\frac{\partial h_1}{\partial y} + \frac{1}{\gamma \mathrm{Ma}^2}\frac{1}{h_1}\frac{\partial T}{\partial x} \\ \frac{\rho}{h_1}\frac{\partial u}{\partial x} + \frac{\rho v}{h_1}\frac{\partial h_1}{\partial y} + \frac{1}{h_1}\frac{d\mu}{dT}\frac{\partial T}{\partial y}\frac{1}{\mathrm{Re}}\frac{\partial h_1}{\partial y} + \frac{\mu}{\mathrm{Re}}\frac{1}{h_1}\frac{\partial h_1}{\partial y}\left(\frac{1}{h_1}\frac{\partial h_1}{\partial y}\right) \\ \rho\frac{\partial u}{\partial y} + \rho\frac{u}{h_1}\frac{\partial h_1}{\partial y} - \frac{1}{h_1}\frac{d\mu}{dT}\frac{\partial T}{\partial x}\frac{1}{\mathrm{Re}}\left(\frac{4}{3}\frac{1}{h_1}\frac{\partial h_1}{\partial y}\right) \\ 0 \\ -\frac{1}{h_1}\frac{d^2\mu}{dT^2}\frac{\partial T}{\partial x}\frac{1}{\mathrm{Re}}\left(\frac{4}{3}\frac{1}{h_1}\frac{\partial u}{\partial x} + \frac{4}{3}\frac{v}{h_1}\frac{\partial h_1}{\partial y} - \frac{2}{3}\frac{\partial v}{\partial y}\right) \\ \left\langle -\frac{1}{h_1}\frac{d^2\mu}{dT^2}\frac{\partial T}{\partial y}\frac{1}{\mathrm{Re}}\left(h_1\frac{\partial u}{\partial y} + \frac{\partial v}{\partial x} - u\frac{\partial h_1}{\partial y}\right) \right. \\ \left. -\frac{d\mu}{dT}\frac{1}{\mathrm{Re}}\frac{1}{h_1}\frac{\partial h_1}{\partial y}\left(\frac{\partial u}{\partial y} + \frac{1}{h_1}\frac{\partial v}{\partial x} - \frac{u}{h_1}\frac{\partial h_1}{\partial y}\right) \right\rangle \\ -\frac{1}{h_1}\frac{d\mu}{dT}\frac{1}{\mathrm{Re}}\left(h_1\frac{\partial^2 u}{\partial y^2} + \frac{\partial^2 v}{\partial x \partial y}\right) + \frac{1}{\gamma \mathrm{Ma}^2}\frac{1}{h_1}\frac{\partial \rho}{\partial x} \\ -\frac{1}{h_1}\frac{d\mu}{dT}\frac{1}{\mathrm{Re}}\left(\frac{4}{3}\frac{1}{h_1}\frac{\partial^2 u}{\partial x^2} + \frac{4}{3}\frac{\partial v}{\partial x}\frac{1}{h_1}\frac{\partial h_1}{\partial y} - \frac{2}{3}\frac{\partial^2 v}{\partial x \partial y}\right) \end{bmatrix}$$

$$\mathbf{D}_{31} = \frac{\partial v}{\partial t} + \frac{u}{h_1}\frac{\partial v}{\partial x} + v\frac{\partial v}{\partial y} - \frac{uu}{h_1}\frac{\partial h_1}{\partial y} + \frac{1}{\gamma \mathrm{Ma}^2}\frac{\partial T}{\partial y}$$

$$\mathbf{D}_{32} = \frac{\rho}{h_1}\frac{\partial v}{\partial x} - 2\rho\frac{u}{h_1}\frac{\partial h_1}{\partial y} + \frac{1}{h_1}\frac{1}{\mathrm{Re}}\frac{d\mu}{dT}\frac{\partial T}{\partial x}\frac{1}{h_1}\frac{\partial h_1}{\partial y}$$

$$\mathbf{D}_{33} = \rho\frac{\partial v}{\partial y} + \frac{2}{h_1}\frac{\partial h_1}{\partial y}\frac{1}{\mathrm{Re}}\mu\frac{1}{h_1}\frac{\partial h_1}{\partial y} + \frac{2}{3}\frac{1}{\mathrm{Re}}\frac{\partial \mu}{\partial y}\frac{1}{h_1}\frac{\partial h_1}{\partial y} - \frac{2}{3}\frac{1}{\mathrm{Re}}\mu\frac{1}{h_1}\frac{1}{h_1}\frac{\partial h_1}{\partial y}\frac{\partial h_1}{\partial y}$$

$$\mathbf{D}_{34} = 0$$

$$\begin{aligned}\mathbf{D}_{35} = {} & \frac{1}{\gamma \mathrm{Ma}^2}\frac{\partial \rho}{\partial y} - \frac{1}{h_1}\frac{1}{\mathrm{Re}}\frac{d^2\mu}{dT^2}\frac{\partial T}{\partial x}\left(\frac{\partial u}{\partial y} + \frac{1}{h_1}\frac{\partial v}{\partial x} - \frac{u}{h_1}\frac{\partial h_1}{\partial y}\right) - \frac{1}{h_1}\frac{1}{\mathrm{Re}}\frac{d\mu}{dT}\left(\frac{\partial^2 u}{\partial x \partial y} + \frac{1}{h_1}\frac{\partial^2 v}{\partial x^2} - \frac{\partial u}{\partial x}\frac{1}{h_1}\frac{\partial h_1}{\partial y}\right) \\ & - \frac{2}{h_1}\frac{\partial h_1}{\partial y}\frac{1}{\mathrm{Re}}\frac{d\mu}{dT}\left(\frac{\partial v}{\partial y} - \frac{1}{h_1}\frac{\partial u}{\partial x} - \frac{v}{h_1}\frac{\partial h_1}{\partial y}\right) + \frac{1}{\mathrm{Re}}\frac{d^2\mu}{dT^2}\frac{\partial T}{\partial y}\left(\frac{2}{3}\frac{1}{h_1}\frac{\partial u}{\partial x} + \frac{2}{3}\frac{v}{h_1}\frac{\partial h_1}{\partial y} - \frac{4}{3}\frac{\partial v}{\partial y}\right) \\ & - \frac{1}{\mathrm{Re}}\frac{d\mu}{dT}\left(-\frac{2}{3}\frac{1}{h_1}\frac{\partial^2 u}{\partial x \partial y} - \frac{2}{3}\frac{1}{h_1}\frac{\partial v}{\partial y}\frac{\partial h_1}{\partial y} + \frac{4}{3}\frac{\partial^2 v}{\partial y^2} + \frac{2}{3}\frac{1}{h_1}\frac{1}{h_1}\frac{\partial h_1}{\partial y}\frac{\partial u}{\partial x} + \frac{2}{3}\frac{1}{h_1}\frac{v}{h_1}\frac{\partial h_1}{\partial y}\frac{\partial h_1}{\partial y}\right)\end{aligned}$$

$$\mathbf{D}_4 = \begin{bmatrix} \frac{u}{h_1}\frac{\partial w}{\partial x} + v\frac{\partial w}{\partial y} \\ \rho\frac{1}{h_1}\frac{\partial w}{\partial x} \\ \rho\frac{\partial w}{\partial y} \\ 0 \\ -\frac{1}{h_1}\frac{d^2\mu}{dT^2}\frac{\partial T}{\partial x}\frac{1}{\mathrm{Re}}\frac{1}{h_1}\frac{\partial w}{\partial x} - \frac{1}{h_1}\frac{d\mu}{dT}\frac{1}{\mathrm{Re}}\frac{1}{h_1}\frac{\partial^2 w}{\partial x^2} - \frac{1}{h_1}\frac{\partial h_1}{\partial y}\frac{1}{\mathrm{Re}}\frac{\partial \mu}{\partial T}\frac{\partial w}{\partial y} - \frac{1}{\mathrm{Re}}\frac{d^2\mu}{dT^2}\frac{\partial T}{\partial y}\frac{\partial w}{\partial y} - \frac{1}{\mathrm{Re}}\frac{d\mu}{dT}\frac{\partial^2 w}{\partial y^2} \end{bmatrix}$$

$$\mathbf{D}_{51} = \frac{u}{h_1}\frac{\partial T}{\partial x} + v\frac{\partial T}{\partial y} - \frac{\gamma-1}{\gamma}\frac{u}{h_1}\frac{\partial T}{\partial x} - \frac{\gamma-1}{\gamma}v\frac{\partial T}{\partial y}$$

$$\begin{aligned}\mathbf{D}_{52} = {} & \frac{\rho}{h_1}\frac{\partial T}{\partial x} - \frac{\gamma-1}{\gamma}\left(\frac{1}{h_1}\rho\frac{\partial T}{\partial x} + \frac{1}{h_1}T\frac{\partial \rho}{\partial x}\right) \\ & + 2\frac{(\gamma-1)\,\mathrm{Ma}^2}{\mathrm{Re}}\mu\left(-\frac{1}{h_1}\frac{\partial h_1}{\partial y}\frac{1}{h_1}u\frac{\partial h_1}{\partial y} + \frac{1}{h_1}\frac{\partial v}{\partial x}\frac{1}{h_1}\frac{\partial h_1}{\partial y} + \frac{\partial u}{\partial y}\frac{1}{h_1}\frac{\partial h_1}{\partial y}\right)\end{aligned}$$

$$\mathbf{D}_{53} = \rho\frac{\partial T}{\partial y} - \frac{\gamma-1}{\gamma}\left(\rho\frac{\partial T}{\partial y} + T\frac{\partial \rho}{\partial y}\right) - 2\frac{(\gamma-1)\,\mathrm{Ma}^2}{\mathrm{Re}}\mu\left(\begin{array}{l} +\frac{4}{3}\frac{1}{h_1}\frac{\partial u}{\partial x}\frac{1}{h_1}\frac{\partial h_1}{\partial y} + \frac{4}{3}\frac{1}{h_1}\frac{v}{h_1}\frac{\partial h_1}{\partial y}\frac{\partial h_1}{\partial y} \\ -\frac{2}{3}\frac{1}{h_1}\frac{\partial h_1}{\partial y}\frac{\partial v}{\partial y} - \frac{2}{3}\frac{1}{h_1}\frac{\partial h_1}{\partial y}\frac{\partial w}{\partial z} \end{array}\right)$$

$$\mathbf{D}_{54} = 0$$

$$\begin{aligned}\mathbf{D}_{55} = {} & -\frac{\gamma-1}{\gamma}\frac{u}{h_1}\frac{\partial \rho}{\partial x} - \frac{\gamma-1}{\gamma}v\frac{\partial \rho}{\partial y} \\ & - \frac{1}{\mathrm{Re}\,\mathrm{Pr}}\frac{1}{h_1}\frac{1}{h_1}\frac{d^2\kappa}{dT^2}\frac{\partial T}{\partial x}\frac{\partial T}{\partial x} - \frac{1}{\mathrm{Re}\,\mathrm{Pr}}\frac{1}{h_1}\frac{1}{h_1}\frac{d\kappa}{dT}\frac{\partial^2 T}{\partial x^2} - \frac{1}{\mathrm{Re}\,\mathrm{Pr}}\frac{d^2\kappa}{dT^2}\frac{\partial T}{\partial y}\frac{\partial T}{\partial y} \\ & - \frac{1}{\mathrm{Re}\,\mathrm{Pr}}\frac{1}{h_1}\frac{\partial h_1}{\partial y}\frac{d\kappa}{dT}\frac{\partial T}{\partial y} - \frac{1}{\mathrm{Re}\,\mathrm{Pr}}\frac{d\kappa}{dT}\frac{\partial^2 T}{\partial y^2}\end{aligned}$$

$$
-\frac{(\gamma-1)\,\mathrm{Ma}^2}{\mathrm{Re}}\frac{d\mu}{dT}\begin{bmatrix}
\frac{4}{3}\left(\frac{1}{h_1}\frac{\partial u}{\partial x}+\frac{v}{h_1}\frac{\partial h_1}{\partial y}\right)\left(\frac{1}{h_1}\frac{\partial u}{\partial x}+\frac{v}{h_1}\frac{\partial h_1}{\partial y}\right)+\frac{\partial w}{\partial y}\frac{\partial w}{\partial y}+\frac{4}{3}\frac{\partial v}{\partial y}\frac{\partial v}{\partial y}\\
+\frac{1}{h_1}\frac{\partial w}{\partial x}\frac{1}{h_1}\frac{\partial w}{\partial x}-\frac{4}{3}\left(\frac{1}{h_1}\frac{\partial u}{\partial x}+\frac{v}{h_1}\frac{\partial h_1}{\partial y}\right)\left(\frac{\partial v}{\partial y}\right)\\
+\left(\frac{1}{h_1}\frac{\partial v}{\partial x}+\frac{\partial u}{\partial y}-\frac{1}{h_1}u\frac{\partial h_1}{\partial y}\right)\left(\frac{1}{h_1}\frac{\partial v}{\partial x}+\frac{\partial u}{\partial y}-\frac{1}{h_1}u\frac{\partial h_1}{\partial y}\right)
\end{bmatrix}
$$

$$
\mathbf{H_{xx}}=\begin{bmatrix}
0 & 0 & 0 & 0 & 0\\
0 & \frac{4}{3}\frac{1}{h_1}\frac{1}{h_1}\frac{\mu}{\mathrm{Re}} & 0 & 0 & 0\\
0 & 0 & \frac{1}{h_1}\frac{1}{h_1}\frac{\mu}{\mathrm{Re}} & 0 & 0\\
0 & 0 & 0 & \frac{1}{h_1}\frac{1}{h_1}\frac{\mu}{\mathrm{Re}} & 0\\
0 & 0 & 0 & 0 & \frac{1}{\mathrm{Re}\,\mathrm{Pr}}\frac{1}{h_1}\frac{1}{h_1}\kappa
\end{bmatrix}
$$

$$
\mathbf{H_{xy}}=\begin{bmatrix}
0 & 0 & 0 & 0 & 0\\
0 & 0 & \frac{1}{3}\frac{1}{h_1}\frac{\mu}{\mathrm{Re}} & 0 & 0\\
0 & \frac{1}{3}\frac{\mu}{\mathrm{Re}}\frac{1}{h_1} & 0 & 0 & 0\\
0 & 0 & 0 & 0 & 0\\
0 & 0 & 0 & 0 & 0
\end{bmatrix}
$$

$$
\mathbf{H_{xz}}=\begin{bmatrix}
0 & 0 & 0 & 0 & 0\\
0 & 0 & 0 & \frac{1}{3}\frac{1}{h_1}\frac{\mu}{\mathrm{Re}} & 0\\
0 & 0 & 0 & 0 & 0\\
0 & \frac{1}{3}\mu\frac{1}{\mathrm{Re}}\frac{1}{h_1} & 0 & 0 & 0\\
0 & 0 & 0 & 0 & 0
\end{bmatrix}
$$

$$
\mathbf{H_{yy}}=\begin{bmatrix}
0 & 0 & 0 & 0 & 0\\
0 & \frac{\mu}{\mathrm{Re}} & 0 & 0 & 0\\
0 & 0 & \frac{4}{3}\frac{\mu}{\mathrm{Re}} & 0 & 0\\
0 & 0 & 0 & \frac{\mu}{\mathrm{Re}} & 0\\
0 & 0 & 0 & 0 & \frac{\kappa}{\mathrm{Re}\,\mathrm{Pr}}
\end{bmatrix}
$$

$$\mathbf{H_{yz}} = \begin{bmatrix} 0 & 0 & 0 & 0 & 0 \\ 0 & 0 & 0 & 0 & 0 \\ 0 & 0 & 0 & \frac{1}{3}\frac{\mu}{\mathrm{Re}} & 0 \\ 0 & 0 & \frac{1}{3}\frac{\mu}{\mathrm{Re}} & 0 & 0 \\ 0 & 0 & 0 & 0 & 0 \end{bmatrix}$$

$$\mathbf{H_{zz}} = \begin{bmatrix} 0 & 0 & 0 & 0 & 0 \\ 0 & \frac{\mu}{\mathrm{Re}} & 0 & 0 & 0 \\ 0 & 0 & \frac{\mu}{\mathrm{Re}} & 0 & 0 \\ 0 & 0 & 0 & \frac{4}{3}\frac{\mu}{\mathrm{Re}} & 0 \\ 0 & 0 & 0 & 0 & \frac{\kappa}{\mathrm{Re\,Pr}} \end{bmatrix}$$

$$\mathbf{N}_1 = -\left\langle \frac{1}{h_1}\tilde{\rho}\frac{\partial \tilde{u}}{\partial x} + \frac{1}{h_1}\tilde{u}\frac{\partial \tilde{\rho}}{\partial x} + \tilde{\rho}\frac{\partial \tilde{v}}{\partial y} + \tilde{v}\frac{\partial \tilde{\rho}}{\partial y} + \tilde{\rho}\frac{\partial \tilde{w}}{\partial z} + \tilde{w}\frac{\partial \tilde{\rho}}{\partial z} + \frac{\tilde{\rho}\tilde{v}}{h_1}\frac{\partial h_1}{\partial y} \right\rangle$$

$$\begin{aligned}
\mathbf{N}_2 = {} & -\rho\left(\tfrac{\tilde{u}}{h_1}\tfrac{\partial \tilde{u}}{\partial x} + \tilde{v}\tfrac{\partial \tilde{u}}{\partial y} + \tilde{w}\tfrac{\partial \tilde{u}}{\partial z} + \tfrac{\tilde{u}\tilde{v}}{h_1}\tfrac{\partial h_1}{\partial y}\right) - \tilde{\rho}\left(\begin{array}{l} \tfrac{\partial \tilde{u}}{\partial t} + \tfrac{\tilde{u}}{h_1}\tfrac{\partial u}{\partial x} + \tfrac{u}{h_1}\tfrac{\partial \tilde{u}}{\partial x} + \tfrac{\tilde{u}}{h_1}\tfrac{\partial \tilde{u}}{\partial x} + \tilde{v}\tfrac{\partial u}{\partial y} + v\tfrac{\partial \tilde{u}}{\partial y} + \tilde{v}\tfrac{\partial \tilde{u}}{\partial y} \\ +w\tfrac{\partial \tilde{u}}{\partial z} + \tilde{w}\tfrac{\partial \tilde{u}}{\partial z} + \tfrac{\tilde{u}v}{h_1}\tfrac{\partial h_1}{\partial y} + \tfrac{u\tilde{v}}{h_1}\tfrac{\partial h_1}{\partial y} + \tfrac{\tilde{u}\tilde{v}}{h_1}\tfrac{\partial h_1}{\partial y} \end{array} \right) \\
& -\tfrac{1}{\gamma \mathrm{Ma}^2}\tfrac{1}{h_1}\left(\tilde{\rho}\tfrac{\partial \tilde{T}}{\partial x} + \tilde{T}\tfrac{\partial \tilde{\rho}}{\partial x}\right) \\
& +\tfrac{1}{h_1}\left(\begin{array}{l} \tfrac{d^2\mu}{dT^2}\tfrac{\partial T}{\partial x}\tfrac{\tilde{T}}{\mathrm{Re}}\left(\tfrac{4}{3}\tfrac{1}{h_1}\tfrac{\partial \tilde{u}}{\partial x} + \tfrac{4}{3}\tfrac{\tilde{v}}{h_1}\tfrac{\partial h_1}{\partial y} - \tfrac{2}{3}\tfrac{\partial \tilde{v}}{\partial y} - \tfrac{2}{3}\tfrac{\partial \tilde{w}}{\partial z}\right) \\ +\tfrac{d\mu}{dT}\tfrac{\partial \tilde{T}}{\partial x}\tfrac{1}{\mathrm{Re}}\left(\tfrac{4}{3}\tfrac{1}{h_1}\tfrac{\partial \tilde{u}}{\partial x} + \tfrac{4}{3}\tfrac{\tilde{v}}{h_1}\tfrac{\partial h_1}{\partial y} - \tfrac{2}{3}\tfrac{\partial \tilde{v}}{\partial y} - \tfrac{2}{3}\tfrac{\partial \tilde{w}}{\partial z}\right) \\ +\tfrac{d\mu}{dT}\tfrac{\tilde{T}}{\mathrm{Re}}\left(\tfrac{4}{3}\tfrac{1}{h_1}\tfrac{\partial^2 \tilde{u}}{\partial x^2} + \tfrac{4}{3}\tfrac{\partial \tilde{v}}{\partial x}\tfrac{1}{h_1}\tfrac{\partial h_1}{\partial y} - \tfrac{2}{3}\tfrac{\partial^2 \tilde{v}}{\partial x \partial y} - \tfrac{2}{3}\tfrac{\partial^2 \tilde{w}}{\partial x \partial z}\right) \end{array} \right) \\
& +\tfrac{1}{h_1}\left[\begin{array}{l} \tfrac{d^2\mu}{dT^2}\tfrac{\partial T}{\partial y}\tfrac{\tilde{T}}{\mathrm{Re}}\left(h_1\tfrac{\partial \tilde{u}}{\partial y} + \tfrac{\partial \tilde{v}}{\partial x} - \tilde{u}\tfrac{\partial h_1}{\partial y}\right) + \tfrac{d\mu}{dT}\tfrac{\partial \tilde{T}}{\partial y}\tfrac{1}{\mathrm{Re}}\left(h_1\tfrac{\partial \tilde{u}}{\partial y} + \tfrac{\partial \tilde{v}}{\partial x} - \tilde{u}\tfrac{\partial h_1}{\partial y}\right) \\ +\tfrac{d\mu}{dT}\tfrac{\tilde{T}}{\mathrm{Re}}\left(h_1\tfrac{\partial^2 \tilde{u}}{\partial y^2} + \tfrac{\partial^2 \tilde{v}}{\partial x \partial y}\right) \end{array} \right] \\
& +\tfrac{1}{h_1}\left[\tfrac{d\mu}{dT}\tfrac{\partial \tilde{T}}{\partial z}\tfrac{1}{\mathrm{Re}}\left(\tfrac{\partial \tilde{w}}{\partial x} + h_1\tfrac{\partial \tilde{u}}{\partial z}\right) + \tfrac{d\mu}{dT}\tfrac{\tilde{T}}{\mathrm{Re}}\left(\tfrac{\partial^2 \tilde{w}}{\partial x \partial z} + h_1\tfrac{\partial^2 \tilde{u}}{\partial z^2}\right)\right] \\
& +\tfrac{d\mu}{dT}\tfrac{\tilde{T}}{\mathrm{Re}}\tfrac{1}{h_1}\tfrac{\partial h_1}{\partial y}\left(\tfrac{\partial \tilde{u}}{\partial y} + \tfrac{1}{h_1}\tfrac{\partial \tilde{v}}{\partial x} - \tfrac{\tilde{u}}{h_1}\tfrac{\partial h_1}{\partial y}\right) - \tfrac{1}{\gamma \mathrm{Ma}^2}\tfrac{1}{h_1}\left\langle \tilde{\rho}\tfrac{\partial \tilde{T}}{\partial x} + \tilde{T}\tfrac{\partial \tilde{\rho}}{\partial x}\right\rangle
\end{aligned}$$

$$
\begin{aligned}
\mathbf{N}_3 = & -\rho\left(\frac{\tilde{u}}{h_1}\frac{\partial\tilde{v}}{\partial x}+\tilde{v}\frac{\partial\tilde{v}}{\partial y}+\tilde{w}\frac{\partial\tilde{v}}{\partial z}-\frac{\tilde{u}\tilde{u}}{h_1}\frac{\partial h_1}{\partial y}\right)-\tilde{\rho}\left(\begin{array}{l}\frac{\partial\tilde{v}}{\partial t}+\frac{\tilde{u}}{h_1}\frac{\partial v}{\partial x}+\frac{u}{h_1}\frac{\partial\tilde{v}}{\partial x}+\frac{\tilde{u}}{h_1}\frac{\partial\tilde{v}}{\partial x}+\tilde{v}\frac{\partial v}{\partial y}+v\frac{\partial\tilde{v}}{\partial y}+\tilde{v}\frac{\partial\tilde{v}}{\partial y}\\ +w\frac{\partial\tilde{v}}{\partial z}+\tilde{w}\frac{\partial\tilde{v}}{\partial z}-2\frac{\tilde{u}u}{h_1}\frac{\partial h_1}{\partial y}-\frac{\tilde{u}\tilde{u}}{h_1}\frac{\partial h_1}{\partial y}\end{array}\right)\\
& -\frac{1}{\gamma\mathrm{Ma}^2}\left(\tilde{\rho}\frac{\partial\tilde{T}}{\partial y}+\tilde{T}\frac{\partial\tilde{\rho}}{\partial y}\right)\\
& +\frac{1}{h_1}\frac{1}{\mathrm{Re}}\left[\begin{array}{l}\frac{d^2\mu}{dT^2}\frac{\partial T}{\partial x}\tilde{T}\left(\frac{\partial\tilde{u}}{\partial y}+\frac{1}{h_1}\frac{\partial\tilde{v}}{\partial x}-\frac{\tilde{u}}{h_1}\frac{\partial h_1}{\partial y}\right)+\frac{d\mu}{dT}\frac{\partial\tilde{T}}{\partial x}\left(\frac{\partial\tilde{u}}{\partial y}+\frac{1}{h_1}\frac{\partial\tilde{v}}{\partial x}-\frac{\tilde{u}}{h_1}\frac{\partial h_1}{\partial y}\right)\\ +\frac{d\mu}{dT}\tilde{T}\left(\frac{\partial^2\tilde{u}}{\partial x\partial y}+\frac{1}{h_1}\frac{\partial^2\tilde{v}}{\partial x^2}-\frac{\partial\tilde{u}}{\partial x}\frac{1}{h_1}\frac{\partial h_1}{\partial y}\right)\end{array}\right]\\
& +\frac{2}{h_1}\frac{\partial h_1}{\partial y}\frac{1}{\mathrm{Re}}\left[\frac{d\mu}{dT}\tilde{T}\left(\frac{\partial\tilde{v}}{\partial y}-\frac{1}{h_1}\frac{\partial\tilde{u}}{\partial x}-\frac{\tilde{v}}{h_1}\frac{\partial h_1}{\partial y}\right)\right]\\
& -\frac{1}{\mathrm{Re}}\frac{d^2\mu}{dT^2}\frac{\partial T}{\partial y}\tilde{T}\left(\frac{2}{3}\frac{1}{h_1}\frac{\partial\tilde{u}}{\partial x}+\frac{2}{3}\frac{\tilde{v}}{h_1}\frac{\partial h_1}{\partial y}-\frac{4}{3}\frac{\partial\tilde{v}}{\partial y}+\frac{2}{3}\frac{\partial\tilde{w}}{\partial z}\right)\\
& -\frac{1}{\mathrm{Re}}\frac{d\mu}{dT}\frac{\partial\tilde{T}}{\partial y}\left(\frac{2}{3}\frac{1}{h_1}\frac{\partial\tilde{u}}{\partial x}+\frac{2}{3}\frac{\tilde{v}}{h_1}\frac{\partial h_1}{\partial y}-\frac{4}{3}\frac{\partial\tilde{v}}{\partial y}+\frac{2}{3}\frac{\partial\tilde{w}}{\partial z}\right)\\
& -\frac{1}{\mathrm{Re}}\frac{d\mu}{dT}\tilde{T}\left(\begin{array}{l}\frac{2}{3}\frac{1}{h_1}\frac{\partial^2\tilde{u}}{\partial x\partial y}+\frac{2}{3}\frac{1}{h_1}\frac{\partial\tilde{v}}{\partial y}\frac{\partial h_1}{\partial y}-\frac{4}{3}\frac{\partial^2\tilde{v}}{\partial y^2}+\frac{2}{3}\frac{\partial^2\tilde{w}}{\partial y\partial z}\\ -\frac{2}{3}\frac{1}{h_1}\frac{1}{h_1}\frac{\partial h_1}{\partial y}\frac{\partial\tilde{u}}{\partial x}-\frac{2}{3}\frac{1}{h_1}\frac{\tilde{v}}{h_1}\frac{\partial h_1}{\partial y}\frac{\partial h_1}{\partial y}\end{array}\right)\\
& +\frac{d\mu}{dT}\frac{\partial\tilde{T}}{\partial z}\frac{1}{\mathrm{Re}}\left(\frac{\partial\tilde{v}}{\partial z}+\frac{\partial\tilde{w}}{\partial y}\right)+\frac{d\mu}{dT}\frac{\tilde{T}}{\mathrm{Re}}\left(\frac{\partial^2\tilde{v}}{\partial z^2}+\frac{\partial^2\tilde{w}}{\partial y\partial z}\right)
\end{aligned}
$$

$$
\begin{aligned}
\mathbf{N}_4 = & -\rho\left(\frac{\tilde{u}}{h_1}\frac{\partial\tilde{w}}{\partial x}+\tilde{v}\frac{\partial\tilde{w}}{\partial y}+\tilde{w}\frac{\partial\tilde{w}}{\partial z}\right)-\tilde{\rho}\left(\begin{array}{l}\frac{\partial\tilde{w}}{\partial t}+\frac{\tilde{u}}{h_1}\frac{\partial w}{\partial x}+\frac{u}{h_1}\frac{\partial\tilde{w}}{\partial x}+\frac{\tilde{u}}{h_1}\frac{\partial\tilde{w}}{\partial x}\\ +\tilde{v}\frac{\partial w}{\partial y}+v\frac{\partial\tilde{w}}{\partial y}+\tilde{v}\frac{\partial\tilde{w}}{\partial y}+w\frac{\partial\tilde{w}}{\partial z}+\tilde{w}\frac{\partial\tilde{w}}{\partial z}\end{array}\right)\\
& -\frac{1}{\gamma\mathrm{Ma}^2}\left(\tilde{\rho}\frac{\partial\tilde{T}}{\partial z}+\tilde{T}\frac{\partial\tilde{\rho}}{\partial z}\right)\\
& +\frac{1}{h_1}\frac{d^2\mu}{dT^2}\frac{\partial T}{\partial x}\frac{\tilde{T}}{\mathrm{Re}}\left(\frac{1}{h_1}\frac{\partial\tilde{w}}{\partial x}+\frac{\partial\tilde{u}}{\partial z}\right)+\frac{1}{h_1}\frac{d\mu}{dT}\frac{\partial\tilde{T}}{\partial x}\frac{1}{\mathrm{Re}}\left(\frac{1}{h_1}\frac{\partial\tilde{w}}{\partial x}+\frac{\partial\tilde{u}}{\partial z}\right)\\
& +\frac{1}{h_1}\frac{d\mu}{dT}\frac{\tilde{T}}{\mathrm{Re}}\left(\frac{1}{h_1}\frac{\partial^2\tilde{w}}{\partial x^2}+\frac{\partial^2\tilde{u}}{\partial x\partial z}\right)+\frac{1}{h_1}\frac{\partial h_1}{\partial y}\frac{1}{\mathrm{Re}}\frac{\partial\mu}{\partial T}\tilde{T}\left(\frac{\partial\tilde{v}}{\partial z}+\frac{\partial\tilde{w}}{\partial y}\right)\\
& +\frac{1}{\mathrm{Re}}\frac{d^2\mu}{dT^2}\frac{\partial T}{\partial y}\tilde{T}\left(\frac{\partial\tilde{v}}{\partial z}+\frac{\partial\tilde{w}}{\partial y}\right)+\frac{1}{\mathrm{Re}}\frac{d\mu}{dT}\frac{\partial\tilde{T}}{\partial y}\left(\frac{\partial\tilde{v}}{\partial z}+\frac{\partial\tilde{w}}{\partial y}\right)+\frac{1}{\mathrm{Re}}\frac{\partial\mu}{\partial T}\tilde{T}\left(\frac{\partial^2\tilde{v}}{\partial y\partial z}+\frac{\partial^2\tilde{w}}{\partial y^2}\right)\\
& +\frac{\partial\mu}{\partial T}\frac{\partial\tilde{T}}{\partial z}\frac{1}{\mathrm{Re}}\left(-\frac{2}{3}\frac{1}{h_1}\frac{\partial\tilde{u}}{\partial x}-\frac{2}{3}\frac{\tilde{v}}{h_1}\frac{\partial h_1}{\partial y}-\frac{2}{3}\frac{\partial\tilde{v}}{\partial y}+\frac{4}{3}\frac{\partial\tilde{w}}{\partial z}\right)\\
& +\frac{\partial\mu}{\partial T}\tilde{T}\frac{1}{\mathrm{Re}}\left(-\frac{2}{3}\frac{1}{h_1}\frac{\partial^2\tilde{u}}{\partial x\partial z}-\frac{2}{3}\frac{1}{h_1}\frac{\partial\tilde{v}}{\partial z}\frac{\partial h_1}{\partial y}-\frac{2}{3}\frac{\partial^2\tilde{v}}{\partial y\partial z}+\frac{4}{3}\frac{\partial^2\tilde{w}}{\partial z^2}\right)
\end{aligned}
$$

$$
\begin{aligned}
\mathbf{N}_5 = &-\rho\left(\frac{\tilde{u}}{h_1}\frac{\partial\tilde{T}}{\partial x}+\tilde{v}\frac{\partial\tilde{T}}{\partial y}+\tilde{w}\frac{\partial\tilde{T}}{\partial z}\right)-\tilde{\rho}\left(\begin{array}{l}\frac{\partial\tilde{T}}{\partial t}+\frac{\tilde{u}}{h_1}\frac{\partial T}{\partial x}+\frac{u}{h_1}\frac{\partial\tilde{T}}{\partial x}+\frac{\tilde{u}}{h_1}\frac{\partial\tilde{T}}{\partial x}\\ +\tilde{v}\frac{\partial T}{\partial y}+v\frac{\partial\tilde{T}}{\partial y}+\tilde{v}\frac{\partial\tilde{T}}{\partial y}+w\frac{\partial\tilde{T}}{\partial z}+\tilde{w}\frac{\partial\tilde{T}}{\partial z}\end{array}\right)\\
&+\frac{\gamma-1}{\gamma}\left(\begin{array}{l}+\tilde{\rho}\frac{\partial\tilde{T}}{\partial t}+\tilde{T}\frac{\partial\tilde{\rho}}{\partial t}+\frac{u}{h_1}\left(\tilde{\rho}\frac{\partial\tilde{T}}{\partial x}+\tilde{T}\frac{\partial\tilde{\rho}}{\partial x}\right)+\frac{\tilde{u}}{h_1}\left(\tilde{\rho}\frac{\partial T}{\partial x}+T\frac{\partial\tilde{\rho}}{\partial x}+\rho\frac{\partial\tilde{T}}{\partial x}+\tilde{T}\frac{\partial\rho}{\partial x}+\tilde{\rho}\frac{\partial\tilde{T}}{\partial x}+\tilde{T}\frac{\partial\tilde{\rho}}{\partial x}\right)\\ +v\left(\tilde{\rho}\frac{\partial\tilde{T}}{\partial y}+\tilde{T}\frac{\partial\tilde{\rho}}{\partial y}\right)+\tilde{v}\left(\tilde{\rho}\frac{\partial T}{\partial y}+T\frac{\partial\tilde{\rho}}{\partial y}+\rho\frac{\partial\tilde{T}}{\partial y}+\tilde{T}\frac{\partial\rho}{\partial y}+\tilde{\rho}\frac{\partial\tilde{T}}{\partial y}+\tilde{T}\frac{\partial\tilde{\rho}}{\partial y}\right)+w\left(\tilde{T}\frac{\partial\tilde{\rho}}{\partial z}+\tilde{\rho}\frac{\partial\tilde{T}}{\partial z}\right)\\ +\tilde{w}\left(T\frac{\partial\tilde{\rho}}{\partial z}+\rho\frac{\partial\tilde{T}}{\partial z}+\tilde{T}\frac{\partial\tilde{\rho}}{\partial z}+\tilde{\rho}\frac{\partial\tilde{T}}{\partial z}\right)\end{array}\right)\\
&+\frac{1}{\mathrm{Re}\,\mathrm{Pr}}\left(\begin{array}{l}\frac{1}{h_1}\frac{1}{h_1}\frac{d^2\kappa}{dT^2}\frac{\partial T}{\partial x}\tilde{T}\frac{\partial\tilde{T}}{\partial x}+\frac{1}{h_1}\frac{1}{h_1}\frac{d\kappa}{dT}\frac{\partial\tilde{T}}{\partial x}\frac{\partial\tilde{T}}{\partial x}+\frac{1}{h_1}\frac{1}{h_1}\frac{d\kappa}{dT}\tilde{T}\frac{\partial^2\tilde{T}}{\partial x^2}\\ +\frac{d^2\kappa}{dT^2}\frac{\partial T}{\partial y}\tilde{T}\frac{\partial\tilde{T}}{\partial y}+\frac{d\kappa}{dT}\frac{\partial\tilde{T}}{\partial y}\frac{\partial\tilde{T}}{\partial y}+\frac{d\kappa}{dT}\tilde{T}\frac{\partial^2\tilde{T}}{\partial y^2}+\frac{1}{h_1}\frac{\partial h_1}{\partial y}\frac{\partial\kappa}{\partial T}\tilde{T}\frac{\partial\tilde{T}}{\partial y}+\frac{d\kappa}{dT}\frac{\partial\tilde{T}}{\partial z}\frac{\partial\tilde{T}}{\partial z}+\frac{d\kappa}{dT}\tilde{T}\frac{\partial^2\tilde{T}}{\partial z^2}\end{array}\right)\\
&+\frac{(\gamma-1)\mathrm{Ma}^2}{\mathrm{Re}}\mu\left(\begin{array}{l}+\frac{4}{3}\frac{1}{h_1}\frac{1}{h_1}\frac{\partial\tilde{u}}{\partial x}\frac{\partial\tilde{u}}{\partial x}+\frac{4}{3}\frac{\partial\tilde{v}}{\partial y}\frac{\partial\tilde{v}}{\partial y}+\frac{4}{3}\frac{\partial\tilde{w}}{\partial z}\frac{\partial\tilde{w}}{\partial z}+\frac{4}{3}\frac{\tilde{v}}{h_1}\frac{\tilde{v}}{h_1}\frac{\partial h_1}{\partial y}\frac{\partial h_1}{\partial y}+\frac{4}{3}2\frac{1}{h_1}\frac{\partial\tilde{u}}{\partial x}\frac{\tilde{v}}{h_1}\frac{\partial h_1}{\partial y}\\ -\frac{4}{3}\frac{\tilde{v}}{h_1}\frac{\partial h_1}{\partial y}\frac{\partial\tilde{v}}{\partial y}-\frac{4}{3}\frac{1}{h_1}\frac{\partial\tilde{u}}{\partial x}\frac{\partial\tilde{w}}{\partial z}-\frac{4}{3}\frac{\tilde{v}}{h_1}\frac{\partial h_1}{\partial y}\frac{\partial\tilde{w}}{\partial z}-\frac{4}{3}\frac{\partial\tilde{v}}{\partial y}\frac{\partial\tilde{w}}{\partial z}-\frac{4}{3}\frac{1}{h_1}\frac{\partial\tilde{u}}{\partial x}\frac{\partial\tilde{v}}{\partial y}\\ +\frac{\partial\tilde{u}}{\partial y}\frac{\partial\tilde{u}}{\partial y}+\frac{1}{h_1}\tilde{u}\frac{\partial h_1}{\partial y}\frac{1}{h_1}\tilde{u}\frac{\partial h_1}{\partial y}+\frac{1}{h_1}\frac{\partial\tilde{v}}{\partial x}\frac{1}{h_1}\frac{\partial\tilde{v}}{\partial x}+\frac{\partial\tilde{u}}{\partial z}\frac{\partial\tilde{u}}{\partial z}+\frac{1}{h_1}\frac{\partial\tilde{w}}{\partial x}\frac{1}{h_1}\frac{\partial\tilde{w}}{\partial x}+\frac{\partial\tilde{v}}{\partial z}\frac{\partial\tilde{v}}{\partial z}+\frac{\partial\tilde{w}}{\partial y}\frac{\partial\tilde{w}}{\partial y}\\ -2\frac{\partial\tilde{u}}{\partial y}\frac{1}{h_1}\tilde{u}\frac{\partial h_1}{\partial y}+2\frac{1}{h_1}\frac{\partial\tilde{v}}{\partial x}\frac{\partial\tilde{u}}{\partial y}-2\frac{1}{h_1}\frac{\partial\tilde{v}}{\partial x}\frac{1}{h_1}\tilde{u}\frac{\partial h_1}{\partial y}+2\frac{\partial\tilde{v}}{\partial z}\frac{\partial\tilde{w}}{\partial y}+2\frac{1}{h_1}\frac{\partial\tilde{w}}{\partial x}\frac{\partial\tilde{u}}{\partial z}\end{array}\right)\\
&+\frac{(\gamma-1)\mathrm{Ma}^2}{\mathrm{Re}}\frac{d\mu}{dT}\tilde{T}\left[\begin{array}{l}\frac{4}{3}\left(\begin{array}{l}\frac{2}{h_1}\frac{1}{h_1}\frac{\partial\tilde{u}}{\partial x}\frac{\partial u}{\partial x}+\frac{1}{h_1}\frac{1}{h_1}\frac{\partial\tilde{u}}{\partial x}\frac{\partial\tilde{u}}{\partial x}+2\frac{1}{h_1}\frac{\partial\tilde{u}}{\partial x}\frac{v}{h_1}\frac{\partial h_1}{\partial y}+2\frac{1}{h_1}\frac{\partial u}{\partial x}\frac{\tilde{v}}{h_1}\frac{\partial h_1}{\partial y}+2\frac{1}{h_1}\frac{\partial\tilde{u}}{\partial x}\frac{\tilde{v}}{h_1}\frac{\partial h_1}{\partial y}\\ +2\frac{\tilde{v}}{h_1}\frac{v}{h_1}\frac{\partial h_1}{\partial y}\frac{\partial h_1}{\partial y}+\frac{\tilde{v}}{h_1}\frac{\tilde{v}}{h_1}\frac{\partial h_1}{\partial y}\frac{\partial h_1}{\partial y}\end{array}\right)\\ +\left(2\frac{\partial\tilde{w}}{\partial y}\frac{\partial w}{\partial y}+\frac{\partial\tilde{w}}{\partial y}\frac{\partial\tilde{w}}{\partial y}+2\frac{\partial\tilde{v}}{\partial z}\frac{\partial w}{\partial y}+2\frac{\partial v}{\partial z}\frac{\partial\tilde{w}}{\partial y}+2\frac{\partial\tilde{v}}{\partial z}\frac{\partial\tilde{w}}{\partial y}+2\frac{\partial\tilde{v}}{\partial z}\frac{\partial v}{\partial z}+\frac{\partial\tilde{v}}{\partial z}\frac{\partial\tilde{v}}{\partial z}\right)\\ +\frac{8}{3}\frac{\partial\tilde{v}}{\partial y}\frac{\partial v}{\partial y}+\frac{4}{3}\frac{\partial\tilde{v}}{\partial y}\frac{\partial\tilde{v}}{\partial y}+\frac{8}{3}\frac{\partial\tilde{w}}{\partial z}\frac{\partial w}{\partial z}+\frac{4}{3}\frac{\partial\tilde{w}}{\partial z}\frac{\partial\tilde{w}}{\partial z}\\ +\left(\frac{2}{h_1}\frac{\partial\tilde{w}}{\partial x}\frac{1}{h_1}\frac{\partial w}{\partial x}+\frac{1}{h_1}\frac{\partial\tilde{w}}{\partial x}\frac{1}{h_1}\frac{\partial\tilde{w}}{\partial x}+2\frac{1}{h_1}\frac{\partial\tilde{w}}{\partial x}\frac{\partial u}{\partial z}+2\frac{1}{h_1}\frac{\partial w}{\partial x}\frac{\partial\tilde{u}}{\partial z}+2\frac{1}{h_1}\frac{\partial\tilde{w}}{\partial x}\frac{\partial\tilde{u}}{\partial z}+2\frac{\partial\tilde{u}}{\partial z}\frac{\partial u}{\partial z}+\frac{\partial\tilde{u}}{\partial z}\frac{\partial\tilde{u}}{\partial z}\right)\\ +\left(\begin{array}{l}\frac{2}{h_1}\frac{\partial\tilde{v}}{\partial x}\frac{1}{h_1}\frac{\partial v}{\partial x}+\frac{1}{h_1}\frac{\partial\tilde{v}}{\partial x}\frac{1}{h_1}\frac{\partial\tilde{v}}{\partial x}+2\frac{\partial\tilde{u}}{\partial y}\frac{\partial u}{\partial y}+\frac{\partial\tilde{u}}{\partial y}\frac{\partial\tilde{u}}{\partial y}+\frac{2}{h_1}\tilde{u}\frac{\partial h_1}{\partial y}\frac{1}{h_1}u\frac{\partial h_1}{\partial y}+\frac{1}{h_1}\tilde{u}\frac{\partial h_1}{\partial y}\frac{1}{h_1}\tilde{u}\frac{\partial h_1}{\partial y}\\ +2\frac{1}{h_1}\frac{\partial\tilde{v}}{\partial x}\frac{\partial u}{\partial y}+2\frac{1}{h_1}\frac{\partial v}{\partial x}\frac{\partial\tilde{u}}{\partial y}+2\frac{1}{h_1}\frac{\partial\tilde{v}}{\partial x}\frac{\partial\tilde{u}}{\partial y}-2\frac{1}{h_1}\frac{\partial\tilde{v}}{\partial x}\frac{1}{h_1}u\frac{\partial h_1}{\partial y}-2\frac{1}{h_1}\frac{\partial v}{\partial x}\frac{1}{h_1}\tilde{u}\frac{\partial h_1}{\partial y}-2\frac{1}{h_1}\frac{\partial\tilde{v}}{\partial x}\frac{1}{h_1}\tilde{u}\frac{\partial h_1}{\partial y}\\ -2\frac{\partial\tilde{u}}{\partial y}\frac{1}{h_1}u\frac{\partial h_1}{\partial y}-2\frac{\partial u}{\partial y}\frac{1}{h_1}\tilde{u}\frac{\partial h_1}{\partial y}-2\frac{\partial\tilde{u}}{\partial y}\frac{1}{h_1}\tilde{u}\frac{\partial h_1}{\partial y}\end{array}\right)\\ -\frac{4}{3}\left(\frac{1}{h_1}\frac{\partial\tilde{u}}{\partial x}\frac{\partial v}{\partial y}+\frac{1}{h_1}\frac{\partial u}{\partial x}\frac{\partial\tilde{v}}{\partial y}+\frac{1}{h_1}\frac{\partial\tilde{u}}{\partial x}\frac{\partial\tilde{v}}{\partial y}+\frac{\tilde{v}}{h_1}\frac{\partial h_1}{\partial y}\frac{\partial v}{\partial y}+\frac{v}{h_1}\frac{\partial h_1}{\partial y}\frac{\partial\tilde{v}}{\partial y}+\frac{\tilde{v}}{h_1}\frac{\partial h_1}{\partial y}\frac{\partial\tilde{v}}{\partial y}\right)\\ -\frac{4}{3}\left(\frac{1}{h_1}\frac{\partial\tilde{u}}{\partial x}\frac{\partial w}{\partial z}+\frac{1}{h_1}\frac{\partial u}{\partial x}\frac{\partial\tilde{w}}{\partial z}+\frac{1}{h_1}\frac{\partial\tilde{u}}{\partial x}\frac{\partial\tilde{w}}{\partial z}+\frac{\tilde{v}}{h_1}\frac{\partial h_1}{\partial y}\frac{\partial w}{\partial z}+\frac{v}{h_1}\frac{\partial h_1}{\partial y}\frac{\partial\tilde{w}}{\partial z}+\frac{\tilde{v}}{h_1}\frac{\partial h_1}{\partial y}\frac{\partial\tilde{w}}{\partial z}\right)\\ -\frac{4}{3}\frac{\partial\tilde{v}}{\partial y}\frac{\partial w}{\partial z}-\frac{4}{3}\frac{\partial v}{\partial y}\frac{\partial\tilde{w}}{\partial z}-\frac{4}{3}\frac{\partial\tilde{v}}{\partial y}\frac{\partial\tilde{w}}{\partial z}\end{array}\right]
\end{aligned}
$$

个人简历、在学期间发表的学术论文与研究成果

个人简历

1991 年 10 月 5 日出生于陕西省西安市长安县（现长安区）。

2009 年 9 月考入清华大学航天航空学院工程力学系钱学森力学班，2013 年 7 月本科毕业并获得工学学士学位。

2013 年 9 月免试进入清华大学大学航天航空学院攻读力学博士学位至今。

发表的学术论文

[1] Zhefu Wang, Liang Wang, and Song Fu. "Control of stationary crossflow modes in swept Hiemenz flows with dielectric barrier discharge plasma actuators", Physics of Fluids, 2017, 29(9): 094105. （SCI 收录，WOS:000412105100038）

[2] Zhefu Wang, Liang Wang, and Song Fu. "Sensitivity analysis of crossflow boundary layer and transition delay using plasma actuator", 8th AIAA Flow Control Conference, AIAA AVIATION Forum, (AIAA 2016-3933). （EI 收录，ISBN-13: 9781624104329）

[3] Zhefu Wang, Liang Wang, and Song Fu. "Control of crossflow instability using plasma actuators", 7th Asia-Pacific International Symposium on Aerospace Technology, 25-27 November 2015, Cairns, Australia. （会议论文）

[4] Zhefu Wang and Song Fu. "Control of crossflow instability using plasma actuators", XXIV ICTAM, 21-26 August 2016, Montreal, Canada.（会议论文）

[5] Zhefu Wang and Song Fu. "Transition delay using DBD plasma actuators", European Drag Reduction and Flow Control Meeting, 3-6 April 2017, Rome, Italy. （会议论文）

综合论文训练记录表

学生姓名		学号		班级	
论文题目					
主要内容以及进度安排	指导教师签字： 考核组组长签字： 年　　月　　日				
中期考核意见	考核组组长签字： 年　　月　　日				

指导教师评语	指导教师签字：_____ 年　　月　　日
评阅教师评语	评阅教师签字：_____ 年　　月　　日
答辩小组评语	答辩小组组长签字：_____ 年　　月　　日

总成绩：_____

教学负责人签字：_____

年　　月　　日